Multi Gigabit/s Visible Light Communications:

Modelling and Demonstrations

Hyunchae Chun

Somerville College

Michaelmas Term 2015

Supervisor: Professor Dominic O'Brien

Department of Engineering Science

A thesis submitted for the Degree of Doctor of Philosophy

ABSTRACT

Traffic in wireless communications is expected to increase exponentially due to demands such as multiple up/downloading, and streaming of ultra-high-definition or multi-dimensional content. This demand requires the development of multi-Giga bit/s communication systems. Insufficient radio spectrum is the main barrier to developing such high-speed wireless systems. Visible light communications (VLC) has the potential to overcome this barrier by providing THz of unlicensed spectrum.

This thesis reports a new generalized modelling method and demonstrations for multi Gigabit/s VLC. For the optimum design of such system, a comprehensive investigation is presented, including the review of existing investigations. Novel design methods, such as optimisation for band-limited optical orthogonal-frequency-division-multiplexing schemes, generalisation of multi-input-multi-output (MIMO) VLC channels, and consideration of device characteristics in the modelling, are introduced for the first time. Then, various VLC techniques are compared considering practical constraints from various VLC channels and devices.

Demonstrations of multi-Gb/s VLC systems are also presented: A 3-Gb/s wireless link with a single Gallium Nitride micro light-emitting-diode (μLED), a 1.68 Gb/s white-light communication link using a conjugated polymer and the μLED, and laser diode (LD) based remote phosphor approach leading to data-rates of up to 6.52 Gb/s for single channel and 10 Gb/s for 2-channel imaging system. These are the fastest demonstrations through a single LED source, and white-light generating LED and LD sources, respectively, at the time this thesis was written.

CONTENTS

Figure Index

Table Index

Acronyms and Abbreviations

ACO-OFDM	Asymmetrically clipped optical OFDM
ADO-OFDM	Asymmetrically clipped DC biased optical OFDM
AWGN	Additive white Gaussian noise
BPSK	Binary phase shift keying
BW	Bandwidth
CAP	Carrier-less amplitude phase modulation
DCO-OFDM	DC biased optical OFDM
DFE	Decision feedback equalisation
DR	Dynamic range
EL	Electro luminescence
EPSRC	Engineering and Physical Sciences Research Council
EQ	Equalisation
FEC	Forward error correction
FFT	Fast Fourier transform
IFFT	Inverse fast Fourier transform
IMDD	Intensity modulation direct detection
IR	Infrared
IrDA	Infrared Data Association
LED	Light emitting diode

LOS	Line of sight
L-PAM	L-level pulse amplitude modulation
L-PPM	L-level pulse amplitude modulation
MLD	Maximum likelihood decoding
NA	Numerical aperture
N-*L*-QAM	N subcarriers L level quadrature amplitude modulation
O-OFDM	Optical orthogonal frequency division multiplexing
OOK	On off keying
OWC	Optical wireless communications
PL	Photo luminescence
PSD	Power spectral density
QPSK	Quadrature phase shift keying
RRC	Root-raised cosine
SC-FDM	Single carrier frequency division multiplexing
Smod	Spatial modulation
Smux	Spatial multiplexing
SNR	Signal to noise ratio
SSL	Solid state lighting
STD	Standard deviation
UP-VLC	Ultra Parallel Visible Light Communications
UV	Ultraviolet
VLC	Visible light communications

VLCA	Visible Light Communications Association
WLED	While light emitting diode
ZFE	Zero forcing equaliser

Chapter 1
Motivation and Aims

1.1 DEMAND AND CHALLENGES FOR MULTI GIGABIT/S WIRELESS SYSTEMS

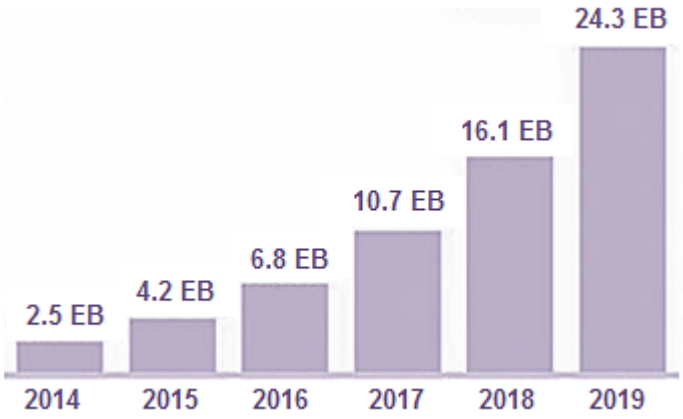

Figure 1. Cisco prediction of global mobile traffic per month (source: Cisco VNI Mobile, 2015)

It has been widely acknowledged that the traffic in wireless communications is increasing exponentially [1][2]. Figure 1 shows Cisco's prediction that overall mobile data traffic will grow almost ten times from 2014 to 2019. In addition, the demand for high-speed data exchange, supporting multiple up/downloading and streaming of ultra-high-definition (UHD) or multi-dimensional content, requires the development of multi-Giga bit/s communication systems [3][4].

The main challenge to develop such high-speed wireless systems is insufficient radio spectrum resources, known as 'Spectrum-Drought' [5]. The radio frequency spectrum is strictly regulated by relevant authorities such as the Federal Communications Commission (FCC) in the US, and is full from 3 kHz to 30 GHz [6]. In addition to its scarcity, the time and cost spent to secure such

communication spectrum is large [7]. For these reasons, other spectrum bands, such as millimetre wave [3][8][9] and optical wave lengths [10]- [11], have been investigated.

Millimetre wave communications systems use a high radio frequency carrier (20–90 GHz) to obtain a large spectrum. For instance, a bandwidth up to 4 GHz is available at a carrier frequency of 38 GHz bands, and a bandwidth of up to 10 GHz is available in a band between 70 and 80 GHz. More details of spectrum planning and current regulatory issues are shown in [8]. There have been a limited number of physical demonstrations. As an example, in 2014, a 1.06 Gb/s system using 27.9 GHz carrier was demonstrated by Samsung Electronics [9].

Optical wireless communications (OWC) uses optical wavelengths in the infrared (IR), visible, and ultraviolet (UV) regions of the spectrum. OWC has the potential to provide ~THz of unlicensed bandwidth, a high degree of spatial reuse, and high security [12]. Typical data rates are hundreds of Mbit/s, using LEDs to provide diffuse coverage, using an intensity modulation, direct detection transmission scheme. Early stage OWC investigations and demonstrations were undertaken in 1960-70, and are reported in [13][14]. Reference [12] investigated diffuse IR radiation and demonstrated 125 kb/s. In the 1990s, short-range links with data rates up to 4 Mb/s, using the Infrared-Data-Association (IrDA) standard were widely deployed [15]. More recently, multi-channel approaches including a 2x2 multiple-input-multiple-output system supporting 10 Mb/s was shown [16]. There have also been a number of high speed demonstrations. A Gigabit class home access network supporting up to 1.25 Gb/s was developed [17], and an IR wireless link with aggregate capacity over 100 Gb/s was demonstrated [11].

It can be seen that Gb/s implementation of both optical wavelength and RF systems have been demonstrated. IR optical wireless requires additional dedicated infrastructure that preserves line of

sight if high rates are to be achieved. In addition eye safety requirements limit the available power, making achieving high rates challenging [8][18].

1.2 VISIBLE LIGHT COMMUNICATIONS

Visible light communications (VLC) can overcome the power constraints that limit performance in IR systems. VLC is an OWC system operating in the visible region of spectrum (390-750 nm). VLC uses the existing lighting infrastructure, which is designed for illumination. It can, therefore, provide considerable cost saving compared with other communication methods requiring additional infrastructure. For the success of VLC, a prerequisite is the deployment of solid state lighting (SSL), usually based on light emitting diodes (LEDs). The successful deployment of SSL based lighting depends on the efficiency and quality of the light compared with the existing sources as well as the cost. White LEDs (WLEDs) are mostly based on blue LEDs combined with a yellow phosphor. These provide high efficiency (94-119 lm/W) comparable to that of fluorescent (108 lm/W) and high intensity discharge (HID) systems (115 lm/W) [19]. (The unit ‘lm/W’ is the ratio between the generated luminous flux and the applied electrical power.) Also, they provide high quality colour rendering and controllability [20]. WLEDs are predicted to become main lighting sources by 2020 [21].

In 2003, the visible light communications consortium (VLCC) was established. This group reported a number of VLC techniques and applications, and standards were also developed [22], and more recently the visible light communications association (VLCA) has superseded the VLCC. Over the following decade the field has grown substantially, with major efforts across the globe.

Recent research has focused on increasing available data rate. These include work on high level modulation, spatial-multiplexing, wavelength-multiplexing, and/or channel equalisation [23]. Reference [24] reviews the research before 2010, and Table 1 summarises recent demonstrations.

Table 1. Recent VLC demonstrations

Reference / Year	Applied source	Applied schemes	Result
[25] / 2015	R/G/B Lasers	Orthogonal-frequency-division-multiplexing & Wavelength-division-multiplexing	14 Gb/s
[26] / 2014	Red Laser	Orthogonal-frequency-division-multiplexing & Spatial multiplexing	10 Gb/s
[27] / 2014	Comercial R/Y/G/B LEDs	Orthogonal-frequency-division-multiplexing & Wavelength-division-multiplexing	5.6 Gb/s
[28] / 2013	Comercial R/G/B LEDs	Careless-amplitude-phase-modulation & Wavelength-division-multiplexing	3.4 Gb/s
[29] / 2013	Comercial WLEDs	Orthogonal-frequency-division-multiplexing & Spatial-multiplexing	1 Gb/s
[30] / 2013	Comercial WLED	Orthogonal-frequency-division-multiplexing (Real-time)	500 Mb/s
[31] / 2010	Comercial WLED	On-off-keying & Analogue-post-equaliser	100 Mb/s

In the past several years, several projects are beginning investigating custom devices for VLC. In the ultra-parallel visible light communications (UP-VLC) project, funded by the Engineering and Physical Sciences Research Council (EPSRC), the use of customised GaN μLEDs and CMOS based integrated system is being investigated [32]. The UPVLC collaborators hold the current

‘world-record’ for a single LED data link [33], and also the record for a white LED using the fast colour converters [34], with a multi-input-multi-output systems demonstrations.

All of these demonstrations have shown that it is possible to construct high-speed VLC links. Most of these investigations chose a specific VLC scheme without in depth comparative research. This is because there has not been a straightforward method to find an optimum scheme for a given VLC channel. A method shown in [35] has been used in several publications comparing performances of different modulation schemes. The method estimates the power and bandwidth requirements for different IM-DD modulation schemes, and enables the comparison. However, this modelling does not include i) the device technology used for transmitter and receiver, and ii) key techniques such as equalisation and multi-input multi-output transmission. For the optimum design of a multi Gigabit VLC system, however, a comprehensive modelling approach is required.

1.3 INVESTIGATION METHODOLOGY

This thesis aims to create a general approach for designing multi Gb/s VLC systems. For this, a comprehensive understanding of VLC schemes and devices are required. A new design method optimising both schemes and devices will be introduced. Work in each chapter is listed below.

- **Chapter 2** shows modelling of illumination and the VLC communication channel.
- **Chapter 3** shows the modelling frame work. Required bandwidth and signal-to-noise ratio for a number of VLC schemes are discussed. The concept of ‘technology-curve’ is introduced to include the impact of VLC transmitter and receiver devices on the available communication power and frequency resources.

- **Chapter 4** shows the comparison of MIMO VLC schemes.
- **Chapter 5** presents examples of maximising the data-rate or margin of VLC systems using the approach developed in Chapter 3 and 4.
- **Chapter 6** shows demonstrations of multi-Gigabit VLC systems using novel custom devices developed in the UPVLC project.
- **Chapter 7** summarises the key results and suggest future work and further developments.

Chapter 2

Modelling of the illumination and communication channel

2.1 INTRODUCTION

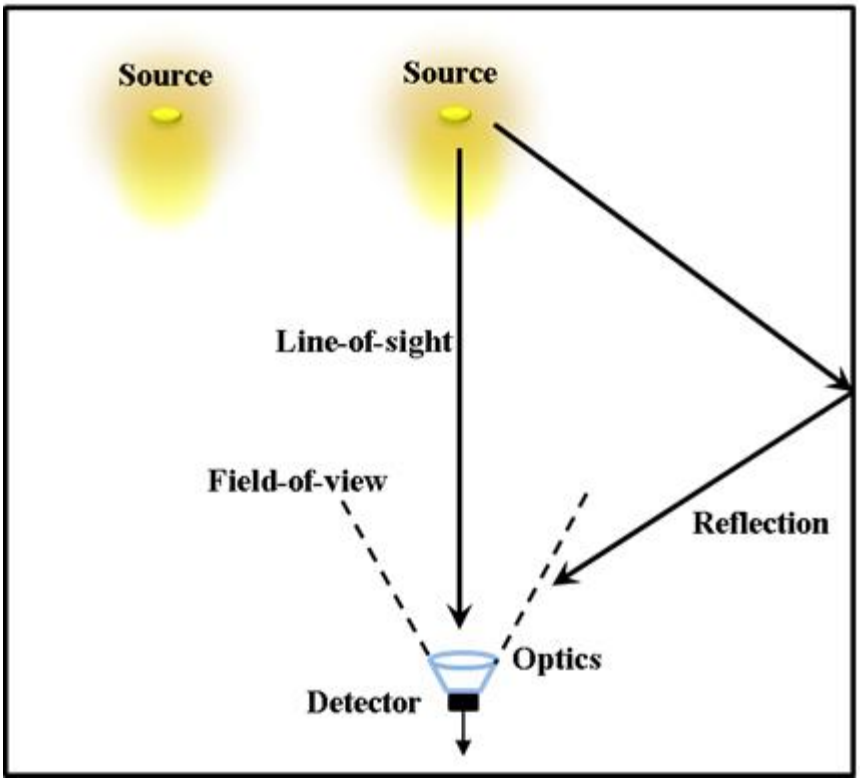

Figure 2. An example of VLC Channel

In this chapter, the impact of lighting designs on the performances of the illumination and communication channel is presented. Figure 2 shows an example of VLC channel. LED sources provide illumination and data transmission. The data signal is carried on the modulated intensity of the visible light, and is collected by receiver optics. Depending on the optical path, optics collects

the light and a photo detector subsequently converts the received optical power into the electrical current for signal processing in electrical domain. It can be seen that the source layout can have a strong influence on VLC channel. This chapter investigates the relationships between illumination and communication channel using two distinct lighting designs as an example.

2.2 ILLUMINATION DESIGN

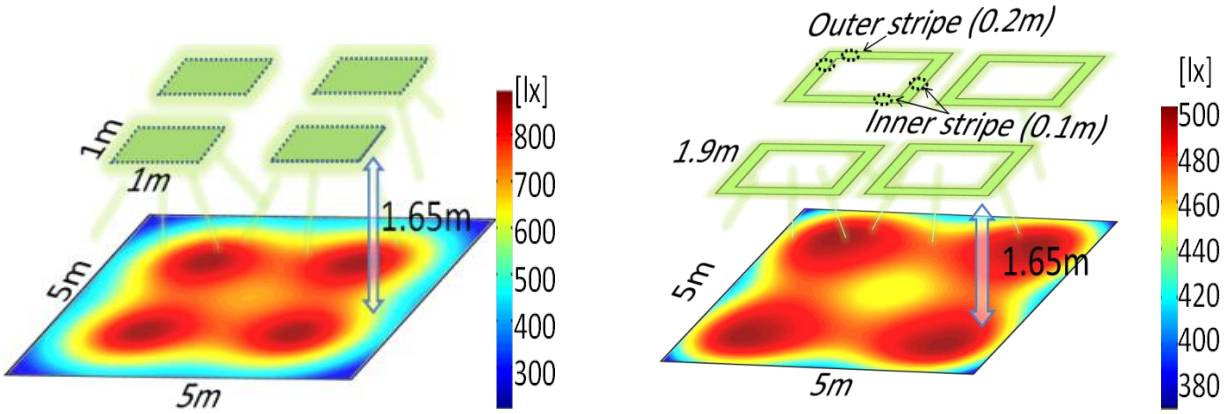

(a) Square design (b) Hollow design

Figure 3. Two lighting designs: (a) square design, and (b) hollow design

In an indoor environment, a certain level of illuminance (~400 lx) on the desk level is required [36]. For a given light source, the layout is an essential factor in meeting this criterion. Two lighting configurations are investigated, as shown in Figure 3. (a) shows a typical square design, and (b) shows the hollow design. (The latter was devised to provide even illumination, and chosen after a number of simulations.)

Table 2. Summary of geometric parameters

Geometric Parameters	**(a) Square design**	**(b) Hollow design**
Room size	5m (length) x 5m (width) x 3m (height)	
Light to desk	1.65m (lighting systems 2.5m – desk 0.85m)	
Distributed area	4 x 1m^2	4 x 0.11m^2
Centre position	(1.2m,1.2m) (1.2m,3.8m) (3.8m,1.2m) (3.8m,3.8m)	(1m,1m) (1m,3m) (3m,1m) (3m,3m)
Features	Square shape	Outer edges : 20cm Inner edges :10cm

Calculation of the illumination level starts from the Lambertian luminous intensity given by [35]:

$$R_o(\phi) = \Phi \cdot \left[\frac{(m+1)}{2\pi}\right] \cdot \cos^m \phi \ \ [lm/sr] \tag{1}$$

where Φ [lm] and ø denote luminous flux of light source and radiation angle, respectively. The Lambertian order *m* determines the radiation pattern and OLEDs can have almost perfect Lambertian emission ($m \approx 1$). The illuminance (*E*) then can be obtained by [35]:

$$E = R_o(\phi) \cdot \cos\theta / r^2 \ \ [lx] \tag{2}$$

where θ denotes the angle between the illumination plane normal direction and the direction of propagation, and *r* is the distance between light source and illumination plane. In the simulation, it is assumed that the distance between two adjacent LEDs is 1 cm, and the illuminance (*E* [lx]) at a

specific point on the illumination plane is obtained by summing each LED's contributions, as calculated by (2).

Table 2 shows the geometric parameters of the two designs, and Table 3 shows the illumination statistics. In the simulation, the same amount of total luminous flux (~ 27 klm) as that in [37] is used for both designs. On average, the square design provides brighter illumination than the hollow design. However, there is a steep gradient in the illumination level, resulting in 7 % of the room area being illuminated below 400 lx. The hollow design shows even illumination with a standard deviation (STD) of 26 lx, and 99 % of desk level area above 400 lx. Having a low STD is important because it reduces the total energy required, considering this 400 lx minimum. Also, a high standard deviation can increase the dynamic range requirements of any VLC receivers, increasing design complexity.

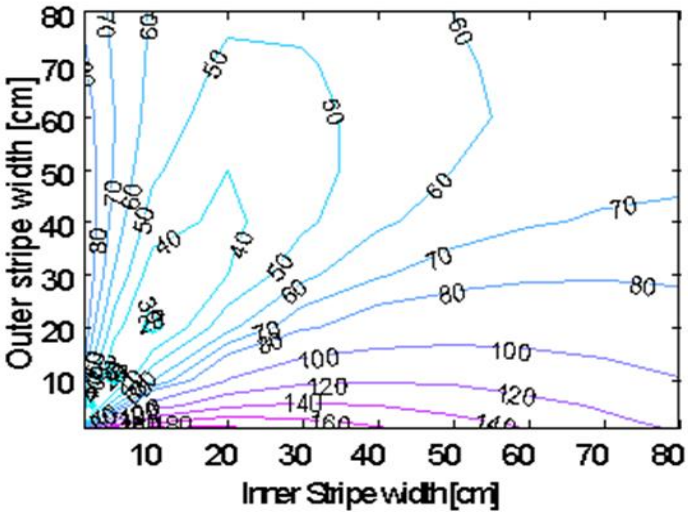

Figure 4. Impact of stripe width in the hollow design on standard deviation of illumination level (lx) on desk plane. Other parameters are shown in Table 2

Figure 4 shows the standard deviation of the illumination level on the desk plane for different inner and outer stripe widths in the hollow design. It can be seen that low standard deviations are achieved when the inner stripes are half the width of the outer stripes. This is thought to be because the effect of two adjacent inner stripes is approximately the same as a single outer stripe.

Table 3. Summary of illumination levels obtained

Brightness Statistics	**(a) Square design**	**(b) Hollow design**
Min / Max / Average [lx]	218 / 892 / 646	362 / 528 / 490
STD [lx]	157	26
Level > 400 lx [%]	93	99

2.3 COMMUNICATION CHANNEL

Next, the communication channels constructed by these two designs are investigated. The VLC channel is composed of line of sight (LOS) and diffuse-paths. LOS paths are modelled as propagation of light from a Lambertian source directly to the receiver. Diffuse paths are modelled as propagation from the LED to an intermediate surface then Lambertian re-emission. Depending on the ray direction, the light may be re-emitted to another intermediate surface and be re-emitted again, or propagate to the receiver. In the modeling, a receiver with a FOV (θ_c) = 60°, a collector refractive index n_c = 1.5, and area of photodiode A_{pd} = 1 cm^2 are used. These are typical values that might be available with a compact receiver. The channel gain H^0 from an ideal Lambertian source to a receiver is [36]:

$$H^0 = \frac{1}{\pi}\cos\phi \cdot \cos\theta \cdot g(\theta) \cdot A_{pd} / r^2 \quad (3)$$

where $\emptyset$ and θ are the radiation angle and receiving angle from receiver's normal direction. r is distance between the source and receiver, and the $g(\theta)$ is the concentrator gain. Assuming light sources and room walls are composed of small segments ($1cm^2$) with Lambertian emission characteristics, the total optical power from all of the segments in the room (including sources and surfaces) to a receiver at a time t can be expressed as

$$P_{rx}(t) = \sum_{i}^{sources} H^0_{source,i} \cdot dP_{source}(t - \tau_{source,i}) + \sum_{k=1}^{K} \sum_{j}^{walls} H^0_{wall,j} \cdot P^k_{wall,j}(t - \tau^k_{wall,j}) \quad (4)$$

The first term represents LOS components. Here, dP_{source} denotes the optical power of one LED segment. $H^0_{source,i}$ and $\tau_{source,i}$ denote channel gain and delay from the i^{th} LED segment to the receiver. The second term represents diffuse components up to the K^{th} reflection. $H^0_{wall,j}$ is the channel gain from j^{th} wall segment to a receiver. $P^k_{wall,j}$ and $\tau^k_{wall,j}$ are the power and accumulated delay to a receiver on the j^{th} wall segment at the k^{th} reflection. P_{rx} at 'desk level' is recursively calculated by the deterministic simulation introduced in [38]. Monte-Carlo simulations with 10 million rays and 0.2 ns resolutions are used for each receiver delay profile. It is assumed that the room has plaster walls and ceiling (reflectivity = 0.8), and the floor has a reflectivity = 0.3 [39].

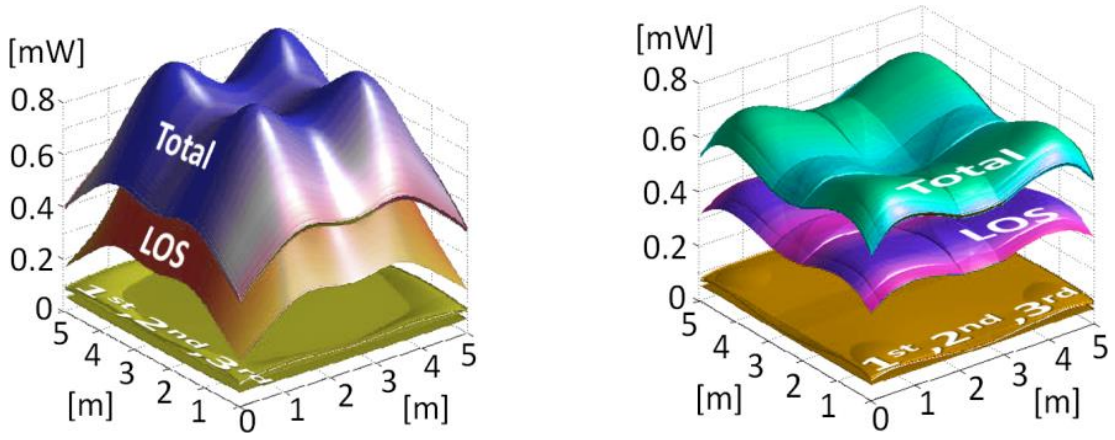

(a) Square design (b) Hollow design

Figure 5. Power (P_{rx}) distribution on desk plane (5m x 5m) of the two designs

Table 4. Summary of received optical power

Received Power Statistics	**(a) Square design**	**(b) Hollow design**
Maximum (LOS/Total) [mW]	0.81 / 0.98	0.43 / 0.71
Minimum (LOS/Total) [mW]	0.17 / 0.38	0.32 / 0.52
Average (LOS/Total) [mW]	0.57 / 0.76	0.40 / 0.63
STD. (LOS/Total) [mW]	0.15 / 0.13	0.02 / 0.04

Figure 5 shows received power distributions at desk level separated into LOS, 1st to 3rd reflections, and their total sum. The received power statistics are arranged in Table 4. In the square design, the strongest LOS components are under the four lighting sources and abruptly fall as a receiver moves to the four corners, causing an STD of 0.15 mW (0.13 mW in 'Total'). In the hollow design, however, the STD of the LOS distribution is only 0.02 mW (0.04 mW in 'Total'). On average, the hollow design transmits less optical power to desk level since the lighting system is placed closer to the walls, losing more power due to the walls' absorbance.

Now, it is of interest to investigate the frequency components within the received optical power. It is observed that where LOS components are dominant, mutual interference due to LOSs having different delays determines the overall spectral shape. However, the worst frequency response observed is at the four corners owing to the relatively higher diffuse power from the walls. Figure 6 shows the normalized impulse and frequency magnitude response at a distance 30 cm in both x and y from one of the corners.

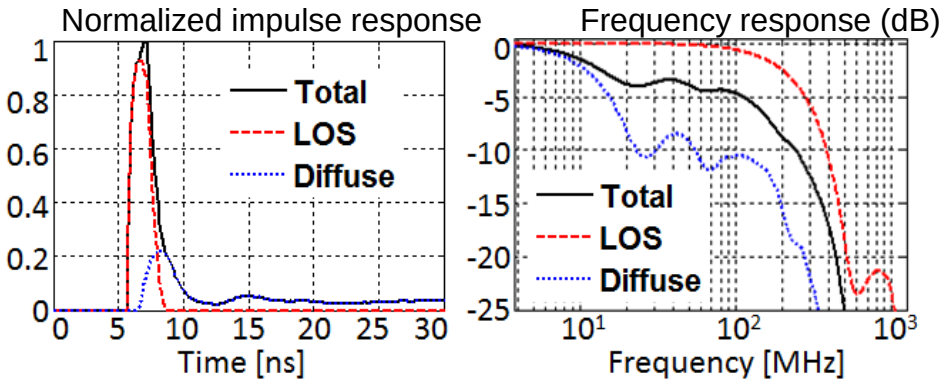

(a) Square design

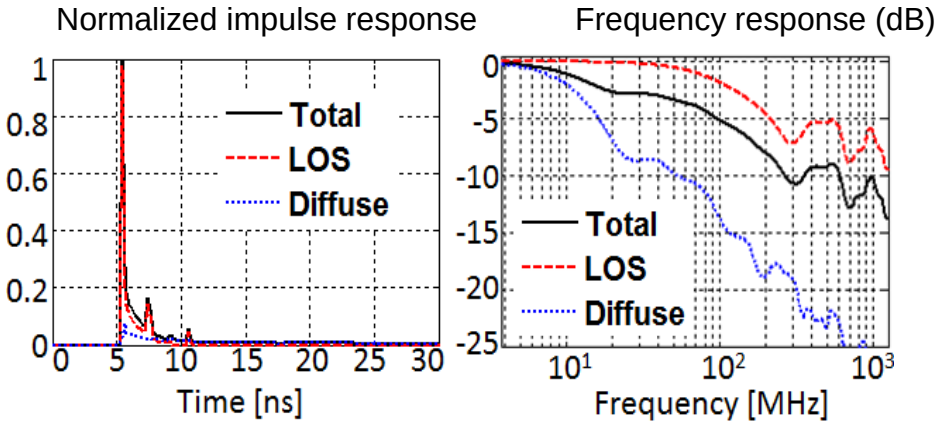

(b) Hollow design

Figure 6. Normalized impulse response and frequency magnitude response of the two designs at Rx position (30 cm x 30 cm)

The 3-dB cutoff of the square design is 17 MHz, and that of hollow design is 40 MHz. This is mainly due to the relatively stronger LOS component, as represented in the normalized impulse response. Nevertheless, it is worth noting that in both designs only ~5 dB of attenuation at frequencies up to 100 MHz is observed. Using this channel, high-speed data transmission (>100 Mbps) can still be achieved by complex modulation and/or equalisation schemes. Therefore, it can be concluded that as long as LOS component exists the effect of the diffuse component in overall frequency response is not significant. (A similar result is shown in [40].)

2.4 CONCLUSIONS

In this chapter, the illumination and communication channel characteristics of two lighting designs were investigated. A simple square design showed a steep gradient in illumination level (and hence the received optical power) compared with a hollow design. The hollow design has even illumination with 99% of room illuminated above the proper level (400 lx) with STD of 26 lx. The hollow design also showed a very small STD of 0.04 mW. Having this low STD can relieve the dynamic range requirements of VLC receivers, reducing the complexity. In terms of bandwidth, both designs showed only ~5 dB attenuation to 100 MHz. It indicates that overall channel frequency response follows that of LOS, and data transmission at frequencies >100 Mbps is still feasible through these channels.

Chapter 3

Modelling of requirements for various VLC techniques

3.1 INTRODUCTION

In order to construct a reliable high-speed VLC link, it is necessary to use optimum communication techniques for a given power and frequency resources. For this, a comprehensive understanding of a number of modulation schemes, channel impairment compensation techniques, and multiple input and output based transmission schemes is required.

There has been some work investigating communication techniques in various VLC environments [38]-[43]. However, many of them show different results and conclusions, due to the different conditions and assumptions. In this chapter, various VLC schemes are compared under the same practical constraints. An in-depth comparison is made by comparing the SNR and bandwidth (BW) requirements of each. This extends the work in [38] by including the characteristics of transmitter and receiver components and MIMO systems. There has been little work analysing the use of equalised channels despite being widely used. In this chapter, such schemes are analysed.

3.2 COMPARISON OF MODULATION SCHEMES IN VLC

A modulation scheme is chosen upon according to available resources (SNR and BW) and required data-rate. An important constraint is that the modulation scheme must not change the

average illumination level, which implies that the comparison should be made under the same average optical power, $P_{optical}$. Figure 7 shows different modulation schemes with the same average optical power

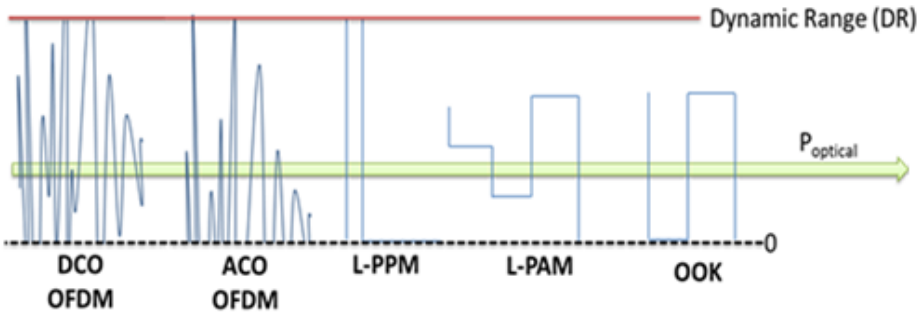

Figure 7. Modulation schemes with the same optical power (the same illumination level)

For the same average optical power ($P_{optical}$), each modulation scheme experiences different levels of penalty from system non-linearity and/or finite dynamic range. Thus, the dynamic range (DR) provided by transmitter and receiver is another key factor to consider. Here, the DR is defined as the maximum level that the instantaneous optical power can reach to. In this chapter, a dynamic range constraint of $\frac{DR}{P_{optical}} = 2$ is used in most cases, as this condition enables a full use of the dynamic range.

In the following comparison, the optical power and receiver noise are the same for all modulation schemes. However, some schemes may induce additional noise, and others may have to reduce signal variance for optimal operation. Therefore, each modulation scheme has a different *SNR* although the same optical power and receiver noise are present.

SNR_{total} =

(5)

$$\frac{\eta_{mod}\,(RP_{optical})^2}{i^2_{mod} + i^2_{comm}} = \frac{\eta_{mod}}{\frac{i^2_{mod}}{(RP_{optical})^2} + \frac{i^2_{comm}}{(RP_{optical})^2}} = \frac{\eta_{mod}}{\gamma^{-1}_{mod} + \gamma^{-1}_{comm}}$$

R : responsivity

η_{mod} : signal variance over squared photocurrent ← modulation dependent

i^2_{mod} : modulation dependent noise

i^2_{comm} : common noise (receiver noise) ← modulation independent

γ_{mod} : SNR by modulation dependent noise only

γ_{comm} : SNR by common noise only

Equation (5) shows the total SNR is made up of a modulation independent term and a modulation dependent term. Equation (6) shows how the required overall SNR ($SNR_{total,req}$) is derived. By (5) and (6), the common required SNR for a target ($\gamma_{comm,req}$) is obtained. In this way, performance of modulation schemes can be compared purely by the optical power and receiver noise relationships.

$$BER = f_{BER\_mod}(SNR_{total}) \rightarrow SNR_{total,req} = f^{-1}{}_{BER\_mod}(target\_BER) \quad (6)$$

f_{BER_mod} : modulation dependant BER function

$SNR_{total,req}$: required SNR_{total} for target BER

$$\gamma_{comm,req} = \left(\frac{\eta_{mod}}{\mathrm{f}_{\mathrm{BER\_mod}}^{-1}(target\_BER)} - \gamma_{mod}^{-1}\right)^{-1} \quad (7)$$

$\gamma_{comm,req}$: required common *SNR* for target BER

For a particular error rate, the required 'common' SNR will be compared because it represents the SNR that the optical power and receiver noise of the system can provide. The overall SNR (SNR_{total}) can be lower than the 'common' SNR (γ_{comm}). Table 5 summarises previous work on the performance comparison of modulation schemes. Each one has meaningful outcomes, although conclusions are not consistent, due to the different assumptions made. The 'comment' column in the table notes some of the shortcomings when taking into account the above practical constraints and the comparison methodology.

Table 5. Previous work

PREVIOUS WORK	SCHEMES	COMPARISON METHOD	CONCLUSION	COMMENT
[38]	*L*-PAM /*L*-PPM BPSK/QPSK /*N*-*L*-QAM	Compared the required optical powers as well as BW for each modulation scheme	*L*-PPM or *L*-PAM is more appropriate for IMDD due to penalties in pass-band modulation schemes.	[CN] [DR]
[44][45]	OOK/*L*-PPM /DCO-OFDM /ACO-OFDM /ADO-OFDM	Compared the required optical $^{Eb}/_{N_0}$ and BW.	ACO-OFDM is desirable thanks to its high power efficiency. ADO-OFDM can be more power efficient than ACO-OFDM.	[CN],[DR] [NS],[NO]

[46]	*L*-PAM/ DCO-OFDM	Compared optimally bit-loaded DCO-OFDM and equalised *L*-PAM in terms of optical link margin. The cases of data-rate exceeding bandwidth were studied.	(*L*-PAM + EQ) results in higher link margin when data-rate exceeds less than ~10 times of the bandwidth. Beyond ~10 times, (bit-loaded DCO-OFDM) gives rise to higher link margin.	[CN],[NS] [NO],[NG]
[47]	*L*-PPM /*L*-PAM DCO-OFDM ACO-OFDM	Compared optimised O-OFDMs (without bit-loading) and L-PAM/L-PPM with equaliser in terms of the required SNR per bit and spectral efficiency. The cases of data-rate exceeding bandwidth were studied.	When signal-bandwidth exceeds channel-bandwidth, DCO-OFDM has the highest spectral efficiency, and its SNR requirement becomes similar (*L*-PAM + DFE). Thus, DCO-OFDM is desirable.	[CN],[NS] [NG]
[41]	*L*-PAM DCO-OFDM ACO-OFDM *L*-PAM-DMT	Compared equalised *L*-PAM and bit/power loaded O-OFDMs in terms of required SNR. Statistically obtained room impulse responses were included.	When modulated less than the given BW, equalised *L*-PAM performs the best, ACO has the same as *L*-PAM DMT, and DCO is the worst. When modulated beyond the BW, DCO performs the best, ACO has the same as *L*-PAM DMT, and equalised *L*-PAM is the worst.	[CN],[DR] [NS],[NO]

- Abbreviations: *L*-PAM (*L*-level pulse amplitude modulation), *L*-PPM (*L*-level pulse position modulation), BPSK (binary phase shift keying), QPSK (quadrature phase shift keying), *N*-*L*-QAM (*N* sub-carriers *L* level quadrature amplitude modulation), BW (bandwidth), IMDD (intensity modulation direct detection), O-OFDM (optical orthogonal frequency division multiplexing), OOK (on off keying), DCO-OFDM (DC biased optical OFDM), ACO-OFDM (asymmetrically clipped optical OFDM), ADO-OFDM (asymmetrically clipped DC biased optical OFDM), Eb/N0 (bit energy over noise density), EQ (equaliser), DFE (decision-feedback equaliser)
- [CN]: Constant Noise; Impact of the shot-noise caused by the received optical power was ignored.
- [DR]: Dynamic Range; Impact of the limited dynamic range was not considered.
- [NS]: Not Same optical power; optical power was not set to the same value.
- [NO]: Not Optimised; O-OFDM's signal variance was not optimised.
- [NG]: Not General; only specific cases were discussed.

3.2.1 Base-band modulation schemes

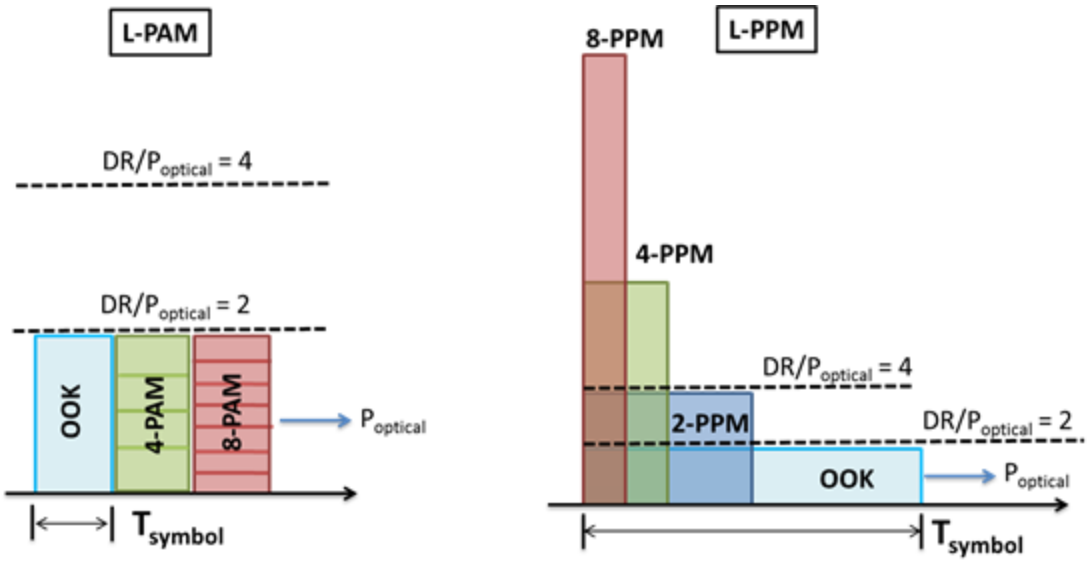

Figure 8. Impact of limited dynamic range on *L*-PAM and *L*-PPM

In this section the required common SNR (γ_comm,req) of base-band modulation scheme is derived, in order to perform a fair comparison with other modulation schemes. The most widely used schemes include On-off-keying (OOK), *L*-level pulse-amplitude-modulation (*L*-PAM), and *L*-level pulse-position-modulation (*L*-PPM). Methods to generate these signals are detailed in [38]. They have a fixed peak value, so it is not necessary to clip the signal for a given dynamic range.

There is no noise generated by the modulation itself. Therefore, γ^{-1}_{mod} is 0. However, η_{mod} can vary depending on the peak-to-peak-amplitude requirement of each scheme. This is because the peak-to-peak-amplitude is limited by the finite DR, for a given $P_{optical}$.

$$\gamma_{comm\text{-}req} = \left(\frac{\eta_{mod}}{f^{-1}_{BER\text{-}mod}(target\_BER)} - \overbrace{\gamma^{-1}_{mod}}^{0} \right)^{-1} \quad (8)$$

$$= \frac{f^{-1}_{BER\text{-}mod}(target\_BER)}{\eta_{mod}}$$

$$\gamma_{b\_comm\text{-}req} = \frac{f^{-1}_{BER\text{-}mod}(target\_BER)}{\eta_{b\_mod}}, \quad (9)$$

where $\eta_{b\_mod} = \eta_{mod}\ log_2 L$

Figure 8 shows how OOK, *L*-PAM, and *L*-PPM operate under different dynamic ranges. Unlike *L*-PAM, *L*-PPM is highly sensitive to the limited dynamic range, and it cannot generate the same optical power ($P_{optical}$) that OOK generates. For instance, using 8-PPM requires 8 times higher peak signal than OOK for the same optical power. If the dynamic-range is sufficient for OOK ($DR/P_{optical}$ =2), there is $(1/8)^2$ SNR penalty for PPM compared with OOK.

Table **6** lists the required SNR and bandwidth for OOK, *L*-PAM, and *L*-PPM scheme from [38], but with the consideration of limited DR. As seen in Figure 8, OOK can also have a penalty when a dynamic range of twice the optical power is not available. In *L*-PAM, signal variance reduces by factor of $(L\text{-}1)^2$. However, thanks to the use of $\log_2 L$ times less BW, SNR gain of $\log_2 L$ is obtained. In *L*-PPM, the impact of limited DR becomes more severe. For example, the penalty from DR induced loss ($loss_{DR}$) of 4-PPM becomes $(¼)^2$ or 12 dB when $\frac{DR}{P_{optical}} = 2$. And, it becomes $(½)^2$ or 6 dB when $\frac{DR}{P_{optical}} = 4$.

Table 6. Required resources for baseband modulation schemes

SCHEMES	loss/gain (η) due to DR and multi-level	Required SNR per bit ($\gamma_{\text{b\_comm-req}}$)	Required Bandwidth
OOK	$\eta_{OOK} = \begin{cases} 1 & , \frac{\text{DR}}{\text{P}_{\text{optical}}} \geq 2 \\ \left(\frac{DR}{P_{optical}} - 1\right)^2 & , \frac{\text{DR}}{\text{P}_{\text{optical}}} < 2 \end{cases}$	$\gamma_{comm\text{-}req,OOK} \simeq \frac{\{\text{Q}^{-1}(target\_BER)\}^2}{\eta_{OOK}}$	BW_{OOK}
L-PAM	$\eta_{b\_L\text{-}PAM} \simeq \eta_{OOK} \frac{log_2 L}{(L-1)^2}$	$\frac{\gamma_{comm\text{-}req,OOK}}{\eta_{b\_L\text{-}PAM}}$	$\frac{BW_{OOK}}{log_2 L}$
L-PPM	$\eta_{b\_L\text{-}PPM} \simeq 0.5L\, log_2 L \cdot loss_{\text{DR}}^2$ $loss_{DR} = \begin{cases} \frac{\text{DR}}{\text{P}_{\text{optical}}} \Big/ 2L & , loss_{\text{DR}} < 1 \\ 1 & , loss_{\text{DR}} \geq 1 \end{cases}$	$\frac{\gamma_{comm\text{-}req,OOK}}{\eta_{b\_L\text{-}PPM}}$	$\frac{L\, BW_{OOK}}{log_2 L}$

Carrier-less amplitude phase (CAP) modulation is a different kind of baseband modulation scheme. It utilises two orthogonal baseband basis functions that enable quadrature modulation, in the baseband. General quadrature amplitude modulation (QAM) requires a BW at least twice that of OOK. However, CAP allows the required BW to be altered by employing a variable root-raised-cosine (RRC) filter based basis function. Detailed implementation methods are shown in [48][49].

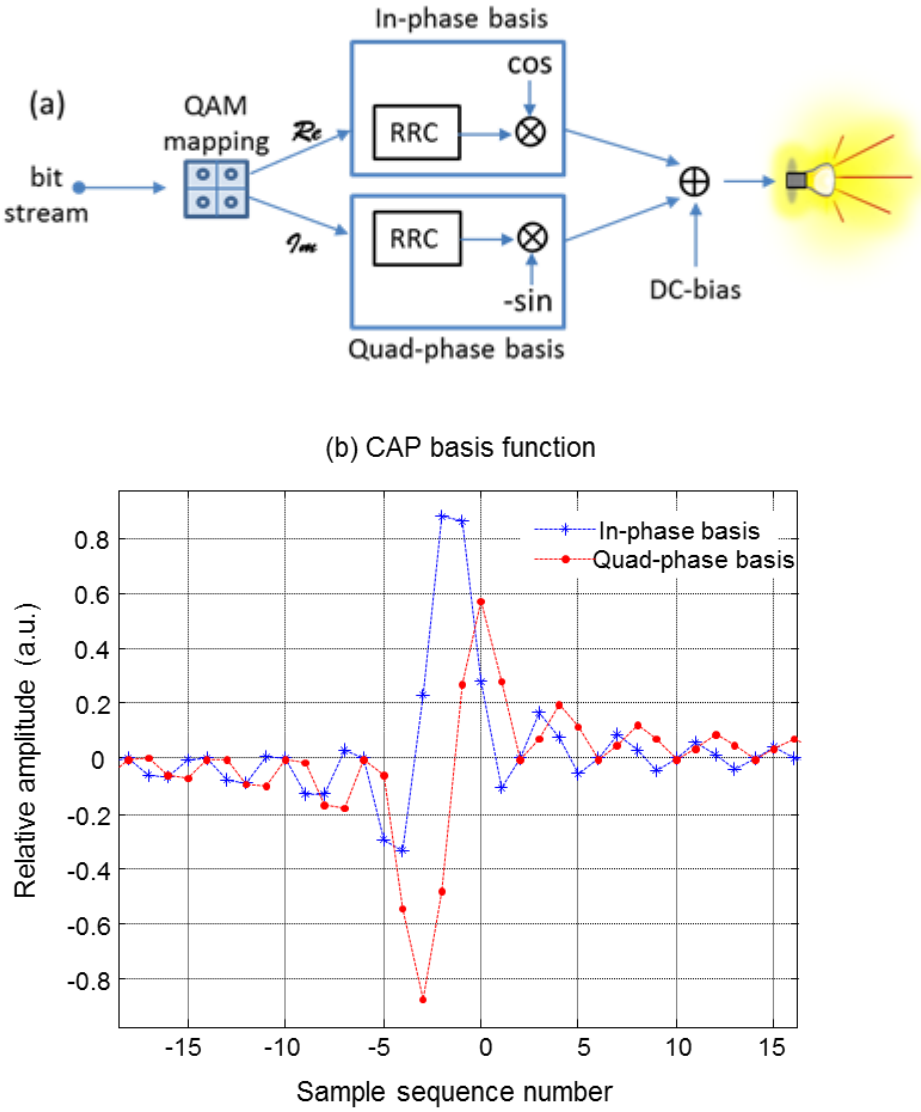

Figure 9. (a) CAP signal generation and (b) two orthogonal base assigning in-phase and quadrature-phase components for CAP modulation

Figure 9-(a) shows how a CAP signal is generated. The main difference from QAM is the direct convolution with two base-band basis with no need for up-conversion, after QAM mapping. Figure 9-(b) shows RRC (roll-off = 0.01) based orthogonal functions with 4 samples per symbol. Using this basis with 0.01 roll-off, the BW that *L* level CAP (*L*-CAP) occupies becomes almost half of *L*-QAM and the same as *L*-PAM.

However, *L*-CAP suffers from higher peak level ($A_{peak,LCAP}$) to standard deviation (STD) ratio, mainly due to the basis shape. Despite *L*-CAP's finite $A_{peak,LCAP,}$ the signal peak-to-peak amplitude has to be scaled to fall within the system DR, causing a corresponding penalty. For this, a peak level to standard deviation ratio ($\frac{A_{peak,LCAP}}{STD}$), or 'crest-factor', is useful. It becomes straightforward to examine the impact of the system dynamic-range using this ratio.

Table 7. L-CAP penalty due to peak to standard deviation ratio

	2-CAP	4-CAP	16-CAP	64-CAP	256-CAP	OOK
$\frac{A_{peak,LCAP}}{STD}$	2.11	2.38	2.68	2.83	2.97	1
Penalty	6.5 dB	7.5 dB	8.5 dB	9 dB	9.5 dB	0 dB

Table 7 shows the peak to standard deviation ratios of different *L*-CAP levels and their penalties. A RRC with a roll-off of 0.01 and $\frac{DR}{P_{optical}}$ of 2 is assumed. Compared to OOK which can have a crest-factor of 1, L-CAP shows a value at least twice as high, mainly due to the RRC based basis. This ratio increases for high level CAP schemes, because they require a higher peak amplitude mapping. Assuming that a system has to re-scale A_{peak} to unity due to constrained dynamic range

($\frac{DR}{Poptical}$=2), the corresponding penalty can be calculated. Finally, one can calculate the required SNR for *L*-CAP to provide a target BER by using a typical *L*-QAM BER equation [50], with the penalties calculated above incorporated.

$$\mathrm{BER}_{LCAP} \approx \frac{2\left(\sqrt{L}-1\right)}{\sqrt{L}\log_2\sqrt{L}}\,\mathrm{Q}\left(\sqrt{\left(\frac{\mathrm{STD}}{\mathrm{A}_{\mathrm{peak,LCAP}}}\right)^2\cdot\frac{3\,SNR}{L-1}}\right) \tag{10}$$

3.2.2 Multi-carrier modulation schemes

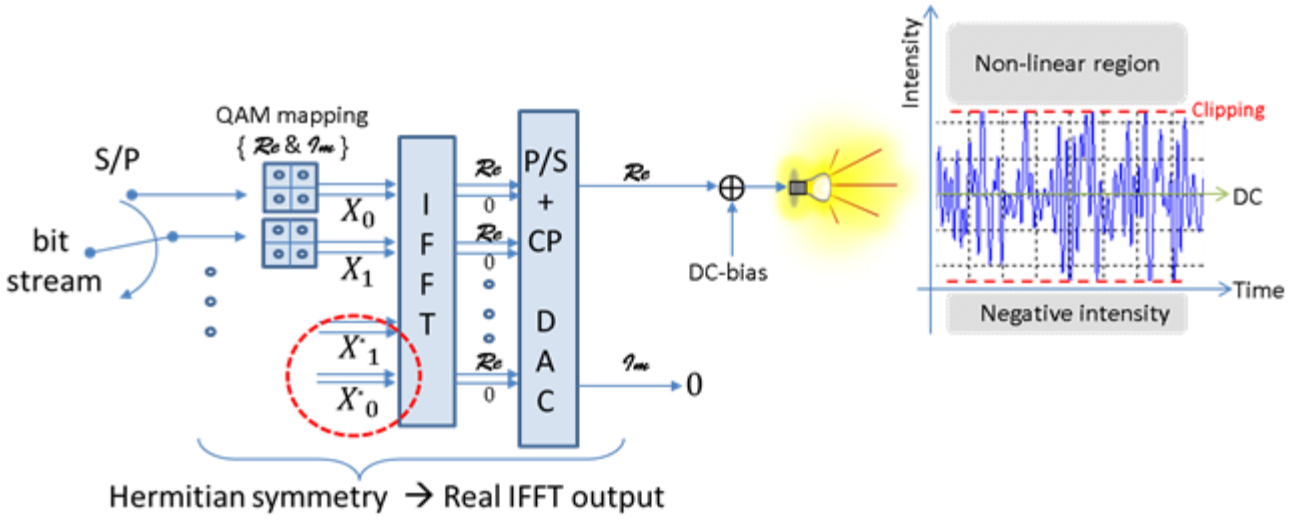

Figure 10. DCO-OFDM signal generation

DC-biased optical orthogonal frequency division multiplexing (DCO-OFDM) [41] [44]-[47] is modified from conventional complex-valued OFDM to allow intensity modulation, and is widely used in VLC. Figure 10 shows the generation of DCO-OFDM. First, QAM symbols are generated

in parallel using the data bits which are to be transmitted, and mapped to sub-carriers by inverse-fast-Fourier-transform (IFFT). The symbols on the IFFT inputs are duplicated and arranged to be Hermitian symmetric, so that the IFFT outputs are real. These outputs are serialised, and a cyclic-prefix (CP) is added. Then, DC addition and appropriate clipping are done to prevent negative intensity and non-linear impairment.

Asymmetrically clipped optical orthogonal frequency division multiplexing (ACO-OFDM) [41][44][45][47] [51] uses a similar method to generate the signal. If QAM symbols are assigned only to odd subcarriers, noise generated by asymmetrical clipping (normally clipping below zero signal level) only falls into even sub-carriers. These carriers are not used, but allow an increased signal variance. However, in a dynamic range limited system, the upper signal level clipping has to be accommodated. Then, the clipping noise generated by this falls not only on even subcarriers, but also on odd-subcarriers where information is loaded.

DCO-OFDM is considered a bandwidth efficient scheme, but generates high clipping noise, with a low power efficiency. ACO-OFDM is considered a power efficient scheme, but requires twice the bandwidth of DCO-OFDM. For both O-OFDMs, careful clipping optimisation is needed. Equation (11) shows how to obtain the required common *SNR* for O-OFDM schemes. Setting a large signal variance can increase $\eta_{\mathrm{O-OFDM}}$, thus reducing the required SNR. In return, however, clipping noise is increased with the increased signal variance. Therefore, there is an optimal signal variance (or clipping level) leading to a minimum SNR requirement for a target performance, under a specific DR. The minimum required $\gamma_{\text{comm-req,O-OFDM}}$ for a target BER can be calculated by using (11) detailed in (A1) in Appendix 1, and by employing the clipping noise modelling (A2) introduced in Appendix 2.

$$\gamma_{comm\text{-}req,O\text{-}OFDM} = \left(\frac{\eta_{O\text{-}OFDM}}{f^{-1}_{\text{BER-L-QAM}}(target\_BER)} - \gamma^{-1}_{O\text{-}OFDM} \right)^{-1} \quad (11)$$

η_{O_OFDM} : useful O_OFDM signal variance over a given optical power

γ_{O_OFDM} : SNR resulting from O"_" OFDM clipping noise

$\gamma_{comm\text{-}req,O\text{-}OFDM}$: the required common SNR for O_OFDM

Single carrier frequency division multiplexing (SC-FDM) [52][53] is based on OFDM, but is designed to reduce the high PAPR of OFDM.

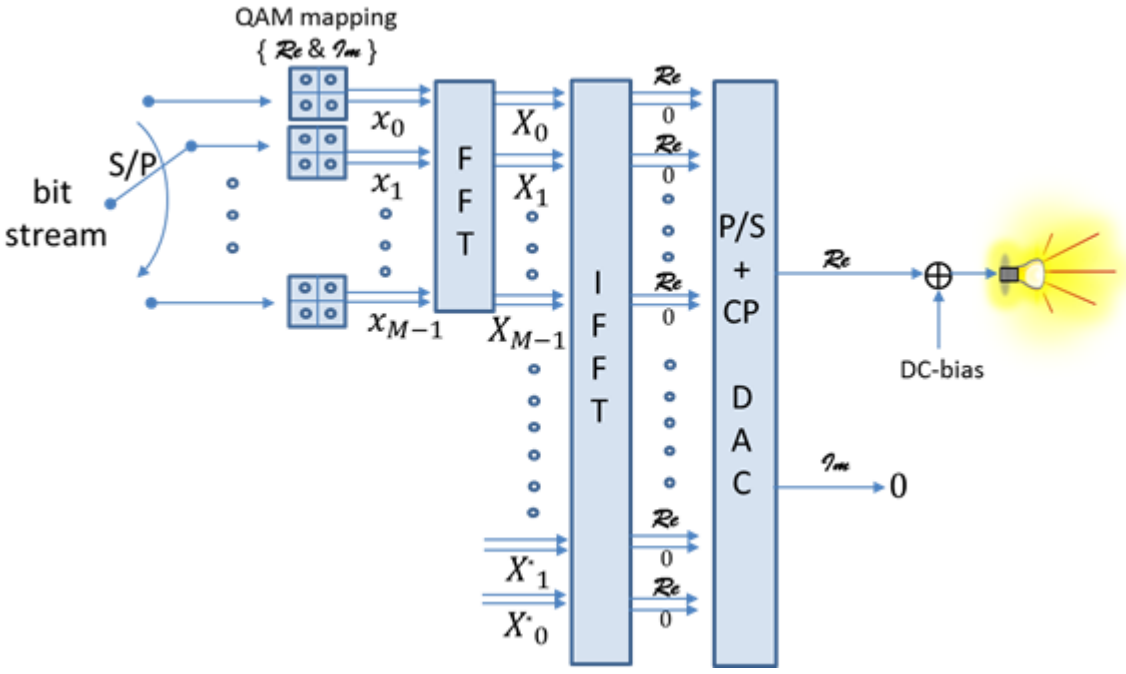

Figure 11. SC-FDM signal generation

Figure 11 shows the generation of an SC-FDM signal. This is similar to OFDM except that there is an FFT operation between the QAM mapping and IFFT operation. This FFT operation

spreads the QAM signal before sub-carrier mapping. This reduces the probability of strong constructive interference among subcarriers, and therefore reduces $\frac{A_{peak}}{STD}$.

Table 8. Comparison of peak to standard deviation ratio

	4-QAM	16-QAM	64-QAM	256-QAM
$\frac{A_{peak,ACO\_OFDM}}{STD}$	7.4	7.5	7.5	7.5
$\frac{A_{peak,DCO\_OFDM}}{STD}$	4.5	4.6	4.6	4.6
$\frac{A_{peak,SCFDM}}{STD}$	3	3.4	3.6	3.8

Table 8 compares the simulated 99.9-percentile $\frac{A_{peak}}{STD}$ of ACO-, DCO-OFDM, and SC-FDM. An IFFT size of 256 is used and 50000 OFDM (or SC-FDM) frames are generated and tested. The percentile indicates the probability that a frame has $\frac{A_{peak}}{STD}$ less than the shown values is 99.9%.

As seen, SC-FDM suppresses the ratio compared to OFDM schemes. It can be further suppressed by interleaving the symbols between the FFT and IFFT block [52]. However, it is hard to apply clipping optimisation. Moreover, it is difficult to apply channel adaptive bit and power loading algorithm that enables the maximum use of the available SNR/frequency resources.

The required SNR for SC-FDM to provide a target performance can be calculated by (12) by using a typical L-QAM BER equation [50], with the penalties calculated from Table 8.

$$BER_{SCFDM} \approx \frac{2\left(\sqrt{L}-1\right)}{\sqrt{L}\log_2\sqrt{L}}\,Q\left(\sqrt{\left(\frac{STD}{A_{peak,SCFDM}}\right)^2 \cdot \frac{3\,SNR}{L-1}}\right) \qquad (12)$$

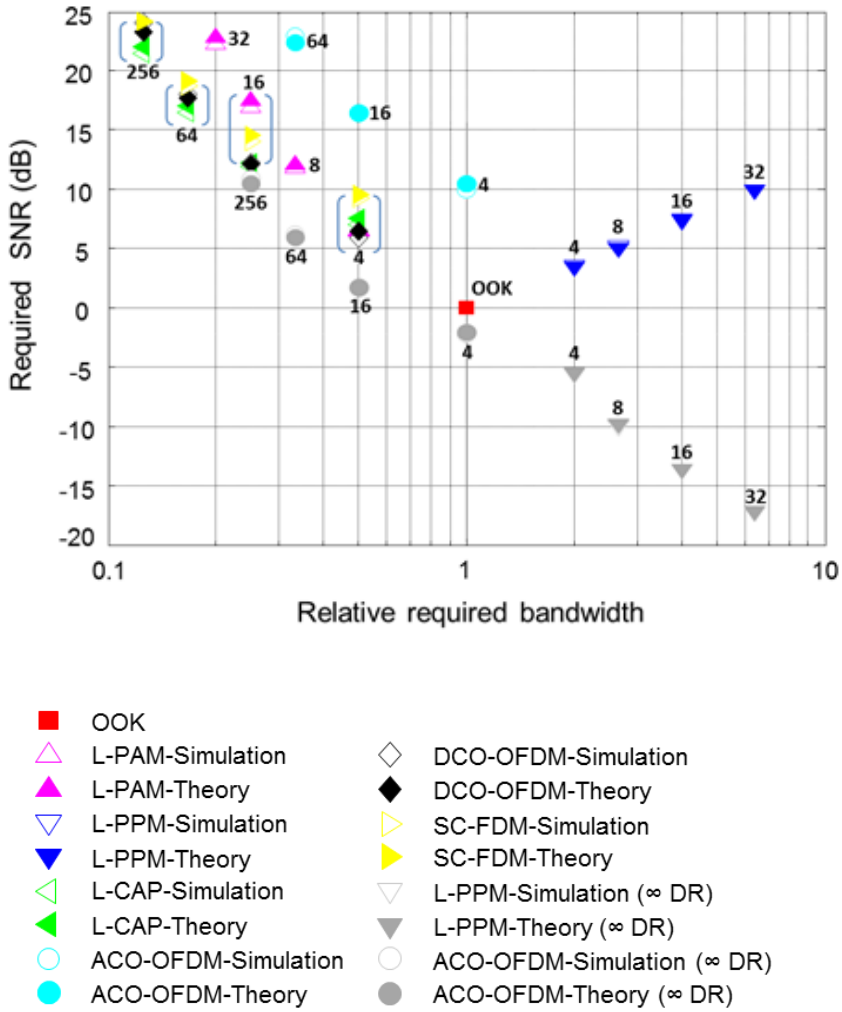

Figure 12. SNR and BW requirements for various modulation schemes to achieve a BER of 10^{-3} compared to the reference scheme (OOK), where the dynamic range constraint is $\frac{\mathbf{DR}}{\mathbf{P_{optical}}}$ of 2, unless indicated otherwise

Figure 12 shows SNR and BW requirements for all the modulation schemes compared to those of OOK. The required SNRs are derived from Table **6** and equations (10-12) above and by Monte-Carlo simulations. All schemes have a target BER of 10^{-3} and dynamic range, $\frac{\mathrm{DR}}{\mathrm{P_{optical}}}$, of 2.

Schemes such as L-PAM, L-CAP, DCO-OFDM, and SC-FDM have signals with symmetrical peaks below and above the average. For these schemes, a full modulation depth, $\frac{\mathrm{DR}}{\mathrm{P_{optical}}}$ more than 2 is not necessary. However, so called power-efficient schemes such as *L*-PPM and ACO-OFDM suffer from considerable peak power suppression by the limited DR. This leads to a significant penalty compared to the case with an infinite dynamic range shown as '∞ DR' in the figure.

L-CAP, DCO-OFDM, and SC-FDM show similar performance with maximum differences of ~4 dB, depending on modulation levels. For 4-QAM, optimally clipped DCO-OFDM shows the minimum required SNR. For larger constellations, the benefits of clipping reduce as the multi-level penalty increases. In this case, DCO-OFDM shows higher penalties than *L*-CAP, which has a smaller peak-to-standard-deviation ratio. SC-FDM shows the highest penalties compared with *L*-CAP and DCO-OFDM.

For *L*-PAM, a 4-level scheme requires a similar SNR and BW as DCO-OFDM. However, due to the limitation of one-dimensional modulation, the penalty relative to '∞ DR' rises roughly twice as fast as the quadrature modulation schemes.

In comparison with previous work, the L-PAM and L-PPM results of '∞ DR' case are in good agreement with [38], but here the practical constraints on DR are taken into account. The ACO-OFDM results of '∞ DR' are in good agreement with [44], but the practical constraints summarised in Table 5 are considered here.

For DCO-OFDM, the result shown in Figure 12 shows similar results as [47]. However, [47] assumes that DCO-OFDM consumes twice the BW of OOK. Other DCO-OFDM results shown in [41][44] did not optimise the clipping level and assumed the infinite DR only. There has not been

an investigation of *L*-CAP and SC-FDM using the same method shown here, to the best of our knowledge.

3.3 BW LIMITED CHANNEL COMPENSATION TECHNIQUES

In previous section, it is assumed that the BW is sufficient to provide a flat channel across the signal's frequency spectrum range. However, in many cases, the signal is modulated beyond the available bandwidth, demanding additional compensation techniques such as equalisation for baseband modulation and bit/power loading for O-OFDM schemes. Additional power (SNR) margin is required for these compensation techniques. Their performance depends on the shape of the frequency response of the system and the margin available. Such techniques are examined in the following sections.

3.3.1 Channel Equalisation

For baseband modulation schemes, there are a number of equalisation techniques from linear/non-linear to analogue/discrete-time [54]. Well-known among them are the discrete-time zero-forcing-equaliser (ZFE) and decision-feedback-equaliser (DFE) [55]. In this sub-section, ZFE and DFE approaches are examined.

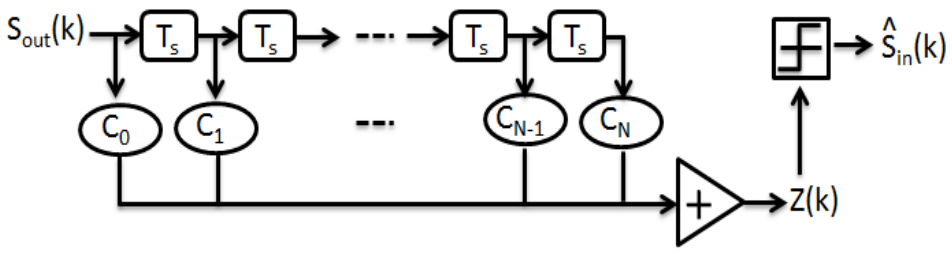

(a) Zero-forcing-equaliser

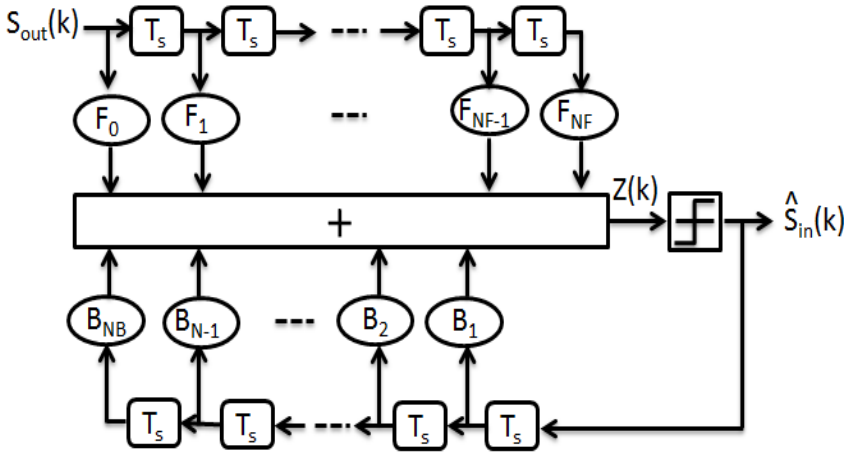

(b) Decision-feedback-equaliser

Figure 13. (a) Linear transversal filter structure of ZFE and (b) feed-back structure of DFE

Figure 13-(a) shows a linear transversal filter structure for ZFE. $S_{out}(k)$ is the received signal modelled as [38];

$$S_{out}(k) = h(k) * S_{in}(k) + n(k) = \underbrace{h(0)\cdot S_{in}(k)}_{Signal} + \underbrace{\sum_{i\neq 0} h(i)\cdot S_{in}(k-i)}_{ISI} + \underbrace{n(k)}_{Noise} \qquad (13)$$

where $S_{in}(k)$, $n(k)$, and $h(k)$ denotes transmitted, noise, and impulse response sequence, respectively.

$S_{out}(k)$ contains a noise term, but also an inter-*symbol-interference (ISI)* term in the bandwidth limited channel case. A ZFE is constructed with a transversal filter that contains delay taps (T_s) and weighting coefficients (C_n) on each tap. The coefficient set, $C_{ZFE} = [\, C_0\, C_1 \cdots C_N \,]$, that leads

to no ISI term in the summed output (Z_k) is derived by transmission and reception of known training sequences [55].

Figure 13-(b) shows a DFE structure employing a transversal feed-forward filter with coefficients $\underline{F} = [F_0\ F_1 \cdots F_{NF}]$ and feed-back filter with coefficients $\underline{B} = [B_1\ B_2 \cdots B_{NB}]$. The equalised signal $Z(k)$ is represented as [56];

$$Z(k) = \sum_{n=0}^{NF} F_n(k) \cdot S_{out}(k-n) + \sum_{j=1}^{NB} B_j(k) \cdot \hat{S}_{in}(k-j) \qquad (14)$$

To find the optimum filter coefficients $\underline{F}$ and $\underline{B}$, the least mean square (LMS) algorithm [55] [56] is usually applied. Using the LMS algorithm, $\underline{F}$ and $\underline{B}$ are iteratively updated until the minimum square error is achieved, as shown below.

$$\underline{C}(k+1) = \underline{C}(k) + \Delta \cdot e(k) \cdot \underline{Y}(k) \qquad (15)$$

where

$$\underline{C}(k) = [\ F_0(k)\quad F_1(k)\quad \cdots\quad F_{NF}(k)\quad B_1(k)\quad B_2(k) \cdots B_{NB}(k)]$$

$$\underline{Y}(k) = [S_{out}(k)\ \ S_{out}(k\text{-}1) \cdots S_{out}(k\text{-}NF)\quad Z(k)\ \ Z(k\text{-}1) \cdots Z(k\text{-}NB)]$$

, and Δ is the step-size parameter, and error is defined in two modes

(16)

$$e(k) = S_{training}(k) - Z(k) \quad \text{, Training mode}$$

$$= \hat{S}_{in}(k) - Z(k) \quad \text{, Decision directed mode}$$

In the training mode, a training sequence $S_{training}(k)$ is transmitted and the resultant DFE output $Z(k)$ is compared with a locally generated replica. In decision directed mode, the coefficient $\underline{C}$ is updated in real time using the error $e(k)$ between the DFE output $Z(k)$ and the estimated symbol $\hat{S}_{in}(k)$. This mode is beneficial when the channel is varying; however, it is more susceptible to wrong decisions ($\hat{S}_{in}(k) \neq S_{in}(k)$). For this reason, it takes a longer time for $\underline{C}(k)$ to converge than in the training mode. In an indoor VLC environment, the channel can be considered stationary, consequently making the training mode more suitable for use in VLC.

The additional SNR required for ZFE and DFE to equalise the aliased channels are given by [46].

$$\text{SNR penalty for ZFE} = 20\log_{10}\left(\frac{1}{\text{BW}}\int_{-\frac{\text{BW}}{2}}^{\frac{\text{BW}}{2}}\frac{1}{Y(f)}\,\text{df}\right)^{-1} \tag{17}$$

$$\text{SNR penalty for DFE} = 20\log_{10}\left\{\exp\left(\frac{1}{\text{BW}}\int_{-\frac{\text{BW}}{2}}^{\frac{\text{BW}}{2}}\ln\big(Y(f)\big)\,\text{df}\right)\right\} \tag{18}$$

$Y(f)$: Received power spectrum

When the signal bandwidth does not surpass the available bandwidth, $Y(f)$ is 1. Thus, no penalty occurs for both ZF and DFE. However, in a band-limited system, the SNR penalty occurs in accordance with the channel's spectral shape. In a typical VLC channel, the limited BW of sources and detectors leads to a low-pass -filter like channel.

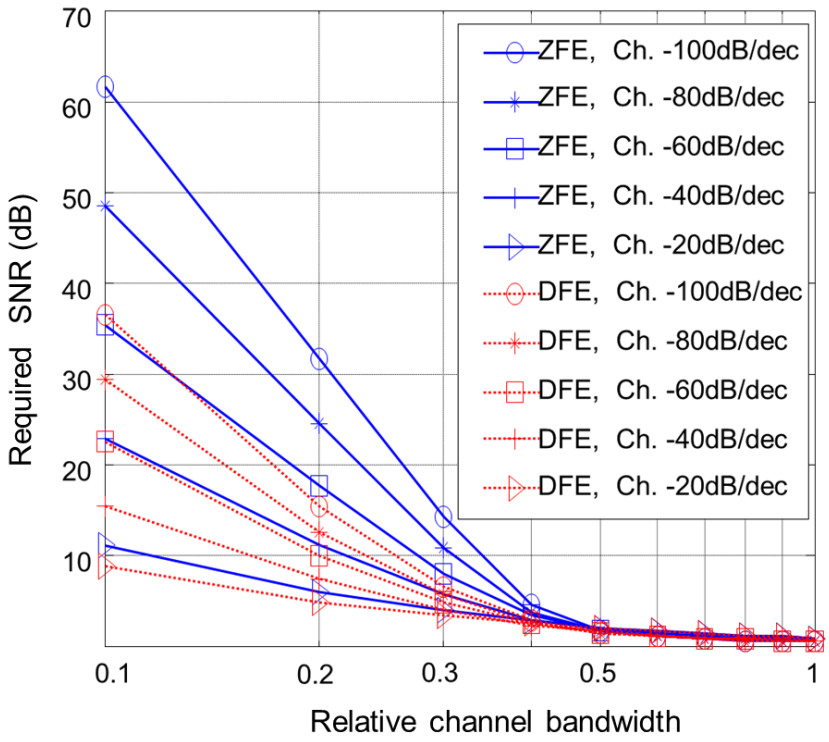

Figure 14. SNR penalty for ZFE and DFE in low-pass-filter channels with various slopes and relative 3-dB BW

Figure 14 shows the calculated SNR requirements for ZFE and DFE to compensate the impact of low-pass-filter (LPF) channels with a slope from -20dB/decade (dec) to -100dB/dec, considering a relative 3 dB BW from 0.1 to 1.

When the channel BW is half of the modulation BW, an SNR penalty of ~2 dB is observed, regardless of equaliser types and channel slope. However, when the relative channel bandwidth is 0.1 with a modulating signal BW 10 times beyond the available BW, the required SNR shows significant differences. In this case, DFE demands less SNR than ZFE for all channel slopes. This difference varies from ~2 dB to ~24 dB in channel slopes from -20dB/dec to -100dB/dec. This is because ZFE is accompanied by significant noise enhancement due to channel flattening, whereas DFE minimises error from both noise and ISI together.

3.3.2 Channel adaptive bit and power loading

O-OFDM schemes allow the segmentation of frequency spectrum and enable capacity approaching bit and power loading schemes. There are several loading algorithms, which can be categorised as i) maximising bit-rate given the available power-margin [57] and ii) Maximising power-margin given the same target bit-rate [58]. The second approach is preferred when comparing the performance of the algorithm for the same target data-rate and BER in various channel environments.

The algorithm shown in [58] is known as the Levin-Campello (LC) algorithm. The LC algorithm assigns bits to each subcarrier, in a way that maximises the total ‘left-over’ SNR margin at each assignment. The bit assignment is repeated until no subcarrier has any margin for adding one more bit. At the end of this process, the residual margins over all subcarriers are equalised so that each sub-carrier can have the same amount of residual margin.

However, there are two problems in applying LC algorithm directly for O-OFDM schemes which are based on optimum clipping; i) the clipping changes the available SNR margin, and ii)

taking out the residual margin from the derived SNR is not straightforward. This is because the residual SNR contains the clipping noise. Therefore, a novel composite LC based bit/power loading algorithm, i) jointly optimising clipping level and SNR margin and ii) leaving zero residual margin at the end, is newly introduced as shown in Figure 15.

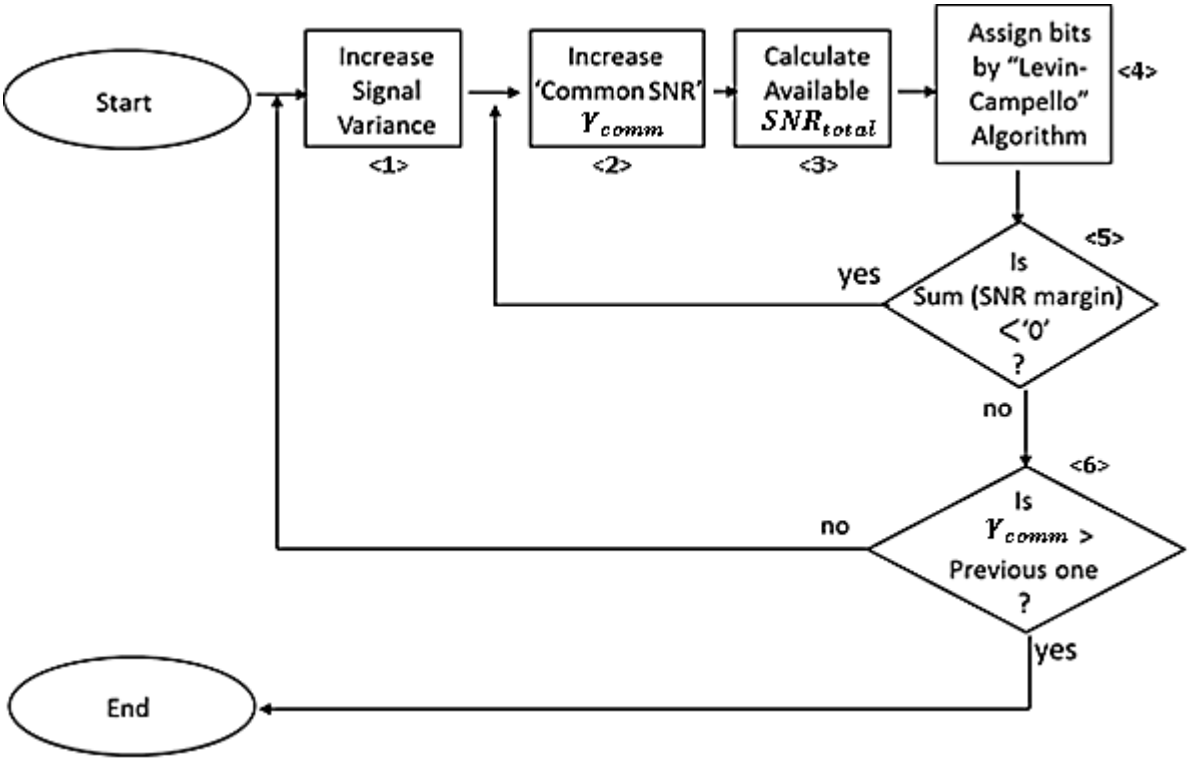

Figure 15. A composite bit and power loading algorithm jointly optimising clipping level and SNR margin to calculate the required common SNR, $\gamma_{comm,req}$

Firstly, the number of bits to be transmitted in each frame is determined, including the overhead of cyclic-prefix required for various channel slopes and BWs (Appendix 3.), and types of O-OFDM schemes used. Then, the following steps are taken.

Step <1>: O-OFDM signal variance is increased from a small initial value under a given dynamic-range. Clipping is applied for the signal peaks that lie outside this dynamic-range.

Step <2>: The common SNR, γ_{comm}, is increased from a small initial value.

Step <3>: The available total SNR, SNR_{total}, comprising the impacts of clipping noise from step <1> and AWGN from step <2> with respect to the signal variance is calculated

Step <4>: The LC algorithm is executed until all bits are assigned.

Step <5>: The sum of residual SNR margin is checked. If negative, the procedure in step <2> is repeated with higher SNR. This is achieved by reducing the AWGN. If positive, the bit and power loading method is feasible.

Step <6>: The current common SNR is compared with the best value. If smaller, the common SNR is decreased by increasing the signal variance, in return adding more clipping noise in step <1>. If larger, the algorithm ends with a conclusion that the signal variance (clipping-level) is the optimum and its common SNR required for a target BER is the minimum.

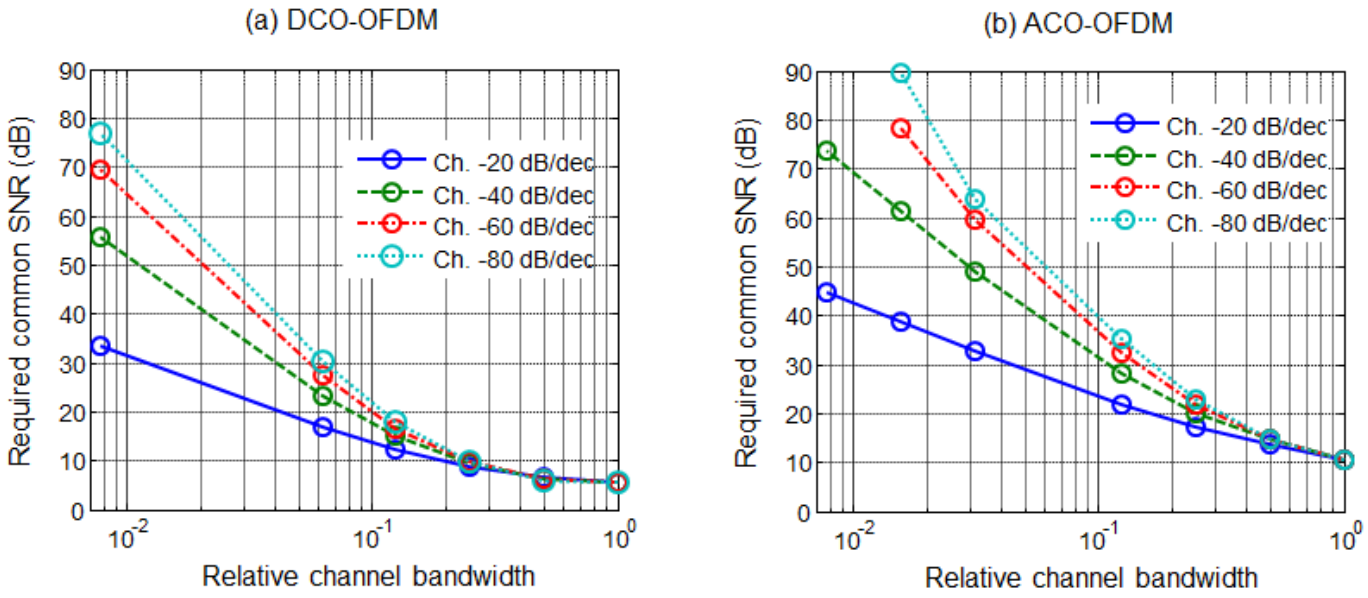

Figure 16. SNR requirement for optimally bit/power loaded (a) DCO-OFDM and (b) ACO-OFDM in various LPF channels

Figure 16 shows the simulated SNR requirement for (a) DCO-OFDM and (b) ACO-OFDM by using the introduced composite bit and power loading algorithm in LPF channels with slopes of -20, -40, -60, and -80 dB/dec. An FFT size of 256, and dynamic range $\frac{\mathrm{DR}}{\mathrm{P_{optical}}}$ of 2 are used for both O-OFDM schemes.

Overall, DCO-OFDM performs better than ACO-OFDM, and the gap in performance becomes greater in channels with faster roll-off. In addition to the penalty from the limited dynamic-range, high frequency sub-carriers in ACO-OFDM are more susceptible to the LPF channel's high-frequency attenuation as only odd-subcarriers are used. In the -20 dB/dec channel, the optimally

bit/power loaded DCO-OFDM shows outstanding performance. When using only 1/100 of the bandwidth, it requires an SNR of ~30 dB, which can be achieved in practical cases.

By applying the above algorithm, [33] demonstrated 3 Gb/s VLC link based on a µLED and a low-noise PD with (1 GHz BW). A system BW was 60 MHz (1/50 of the data-rate). This was possible because the slope of the channel was ~ -20 dB/dec up to ~500 MHz. (The waveform generator used in the experiment had a BW of ~500 MHz so there was a limited performance beyond this frequency.)

According to the above analysis, if the µLED has sufficient power for ~30 dB SNR and if high-speed equipment preserving the ~ -20 dB/dec channel slope is used, 100 times the available BW could be used and rate of 6 Gb/s, should be feasible.

3.4 TECHNOLOGY CURVE

Until now, VLC schemes have been compared, in terms of SNR and BW (or spectral efficiency). However, there is usually a relationship between the available BW and SNR for a particular transmitter/receiver pair. At the transmitter, a particular source technology (such as a GaN LED) will typically emit higher power for lower BW. For a particular type of device, this can be described by a ‘technology curve’ that relates power to BW. At the receiver, a larger area detection allows more power to be collected, but a proportionately lower BW due to the capacitance.

Therefore, high SNR links tend to have lower system bandwidth, and vice versa. To generalise these assumptions the following models can be postulated.

$$BW_{source} = C_{source} \left(\frac{1}{P_{source}}\right)^{K_{source}} \quad (33)$$

$$BW_{detector} = C_{detector} \left(\frac{1}{A_{detector}}\right)^{K_{detector}} \quad (34)$$

,where C_{source}, K_{source}, $C_{detector}$, and $k_{detector}$ are constants describing a specific source and detector technology. P_{source} and $K_{detector}$ mean source power and detector area. In order to verify this model, data from real devices was obtained. Figure 17-(a) shows the available source power vs bandwidth from a range of different diameter GaN µLEDs [72]. The optical power and bandwidth were measured by UP-VLC project partners in Strathclyde University. The fitted line using (33) with C_{source} = 2.564x10^6 and K_{source} = 0.6 brings the minimum squared error, and is in reasonably good agreement with the measured results.

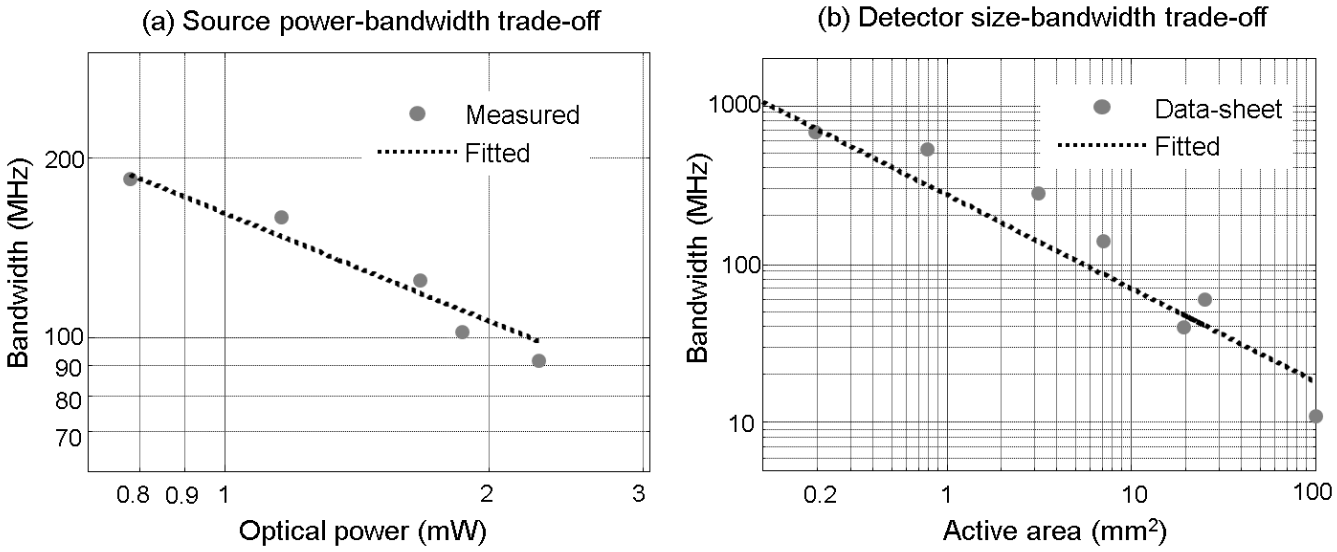

Figure 17. (a) Source power vs source BW from GaN µLEDs and (b) detector area vs BW from Hamamatsu S8664 series, with actual points and a fitted line

Figure 17-(b) shows the detection area vs. bandwidth from a commercial detector (Hamamatsu S8664 series). A fitted line using (34) with $C_{detector}$ = 7.9x10^4 and $K_{detector}$ = 0.59 is in reasonable agreement. The effect of these 'technology curves' on the optimum communication scheme can be examined by observing the SNR gain by changing the BW.

$$\mathrm{SNR_{gain}} = \frac{\mathrm{SNR_2}}{\mathrm{SNR_1}} = \left(\frac{\mathrm{P_{received,2}}}{\mathrm{P_{received,1}}}\right)^2 = \left(\Delta \mathrm{BW}_{\mathrm{source}}^{-(1/\mathrm{K_{source}})} \cdot \Delta \mathrm{BW}_{\mathrm{detector}}^{-(1/\mathrm{K_{detector}})}\right)^2 \qquad (35)$$

$$\simeq \Delta \mathrm{BW}_{\mathrm{system}}^{-2\mathrm{K}_{\mathrm{system}}^{-1}}$$

,where $P_{received,1}$ and $P_{received,2}$ are the received optical power at the two design points on the technology curve. Using equation (34) (35), SNR_{gain} can be calculated as a function of BW changes of source, ΔBW_{source}, and detector, $\Delta BW_{detector}$. If ΔBW_{source} and $\Delta BW_{detector}$ are the same, the SNR_{gain} is simplified by introducing K^{-1}_{system} (=$1/K_{source}$+$1/K_{detector}$). When signal dependent noise (such as shot-noise) is dominant, the SNR_{gain} becomes$\Delta BW_{system}^{-K_{system}^{-1}}$. This is because in this case the SNR gain linearly changes with the optical power gain [36][37].

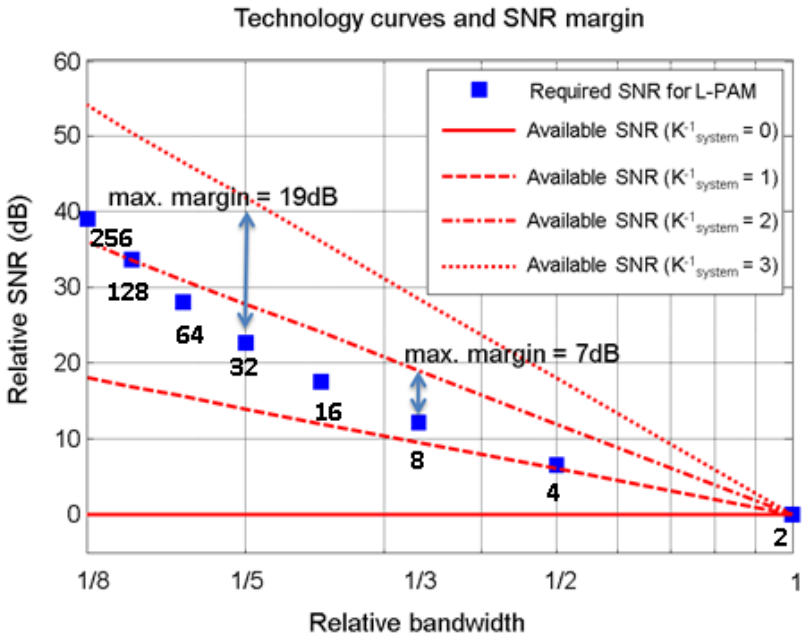

Figure 18. Required SNR for L-PAM and the available SNR vs relative BW for various K^{-1}_{system}

Figure 18 shows the additional SNR required for *L*-PAM vs BW relative to 2-PAM. Also shown are the available SNR (technology curves) for different values of K^{-1}_{system}. Assuming a 0 dB margin for 2-PAM the additional margin can be calculated using the technology curves for other schemes.

K^{-1}_{system} = 0 implies BW and optical power are independent, so there is no further SNR improvement despite reducing the bandwidth. However, when K_{system} increases, it is seen that increasing the number of levels in the *L*-PAM scheme brings a great benefit in terms of system margin.

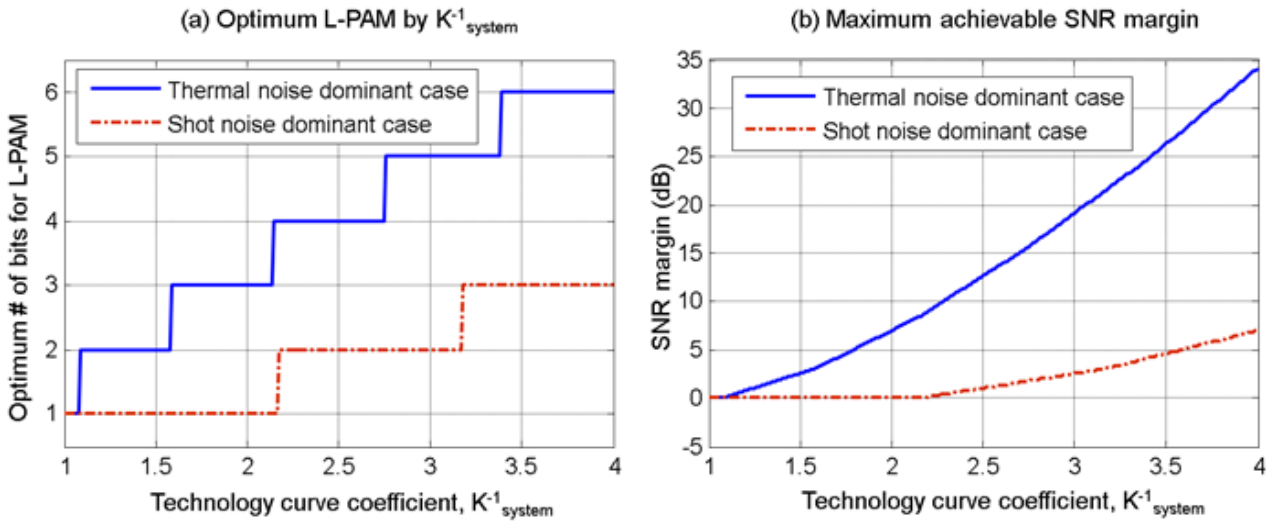

Figure 19. (a) Optimum number of bits for L-PAM, and (b) achievable SNR margins from technology curve vs different K^{-1}_{system} , in the thermal noise or shot noise dominant case.

Figure 19 shows (a) the optimum number of bits per symbol for *L*-PAM, and (b) the achievable maximum margins for different K^{-1}_{system}. It is observed that using higher level PAM and lower BW leads to a larger margin, especially for high K^{-1}_{system}.This tendency is more prominent in a thermal noise dominant case.

As an example, for a system using a specific GaN μLED and a specific detector out of Hamamatsu S8664 series, the estimated K^{-1}_{system} is 3.36. If the system meets the target date-rate/BER performance for OOK, the graph in Figure 19 (a) suggests the use of 32-PAM and a reduction in BW to 1/5 of the original in thermal noise dominant case. Figure 19 (b) indicates that a 23 dB margin can be created by doing so. However, in shot noise dominant case, a maximum of 4 dB margin can be obtained with 8-PAM using 1/3 of the original bandwidth.

Chapter 4
Multi-input-multi-output schemes for VLC

4.1 INTRODUCTION

In this section, multi-input-multi-output VLC (MIMO-VLC) systems are investigated. MIMO-VLC uses a number of transmitters and receivers, which allows parallel data transmission. This can lead to improved spectral efficiency or enhanced link margin, depending on the particular approach used.

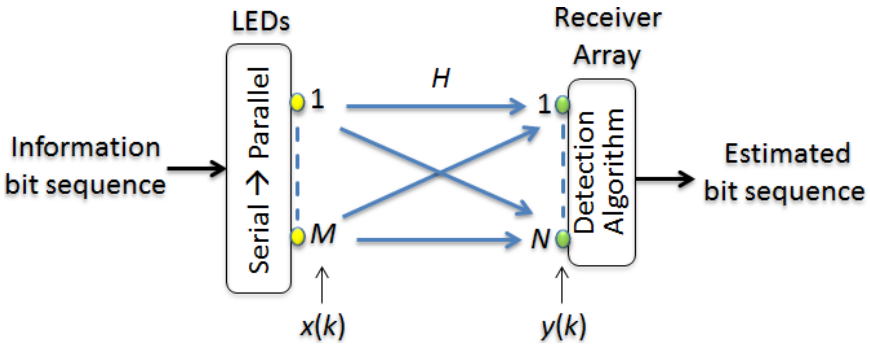

Figure 20. MIMO-VLC system diagram

Figure 20 illustrates a MIMO-VLC system. *M* and *N* denote the number of LEDs and sub-elements of a receiver (Rx). **x**(k) is the transmitted column vector (*M* x 1) and and **y**(k) is the received column vector (*N* x 1) at the k^{th} time sample. The system model can be expressed as

$$\boldsymbol{y}(k) = \mathbf{H}\cdot\boldsymbol{x}(k) + \boldsymbol{n}(\mathrm{k}) \tag{18}$$

where $\boldsymbol{n}(\mathrm{k})$ is noise column vector (N x 1) due to the shot noise and thermal noise of each receiver element. The N by M channel matrix $\mathbf{H}$ is defined by

$$\mathbf{H} = \begin{bmatrix} h_{11} & \cdots & h_{1M} \\ \vdots & \ddots & \vdots \\ h_{N1} & \cdots & h_{NM} \end{bmatrix} \tag{19}$$

where h_{ij} is channel gain from the j^{th} LED to the i^{th} receiver elements. In order to have a full-rank matrix, a requirement for inverting the matrix, the number of receiver elements (N) should be larger or equal to that of LEDs (M).

In addition the H-matrix must have a good condition number. This is governed by spatial correlation between channels. When there is crosstalk between channels due to the spatial correlation, a particular receiver cannot determine which transmitter is transmitting. This leads to a poor matrix condition number, in turn leading to poor MIMO performance.

There have been several investigations of MIMO-VLC [42][59][60][61][43]. These analyses were based on specific cases and do not assist in more general design. Moreover, previous work does not provide a straightforward way to find SNR and BW requirements needed for various modulation schemes used in different MIMO approaches.

This section aims to provide a general method to compare and select the optimum MIMO approach in a given VLC environment. Firstly, some representative MIMO-VLC approaches are described. A general correlated VLC channel modelling method is then introduced. Lastly, representative MIMO schemes are compared.

4.1.1 MIMO-VLC receiver algorithms and schemes

1) Representative schemes

Ganging is the simplest method of using multiple sources and receivers. Here, multiple sources transmit the same information and multiple receivers process the information together. Compared to SISO, this can provide more link margin, allowing higher level modulation, or increasing link-distance and/or coverage area whilst maintaining the same data-rate.

Spatial modulation (Smod) [62][63] assigns information to each source's location. In contrast to Ganging, Smod turns on only one source at a time. An Smod receiver determines which source is turned on by comparing the arrived light intensity at each of it receiver channels, and translates the source's location into data information using pre-defined spatial symbols. Smod allows an improved spectral efficiency by a factor of $\log_2(M)$, but is susceptible to spatially correlated MIMO-VLC channels.

Spatial multiplexing (Smux) [59][61][64] assigns information to each source, as Smod. However, Smux turns on all sources at once, transmitting M independent streams together. Smux allows an enhanced spectral efficiency by a factor of M, but is most vulnerable to correlated MIMO-VLC channels. This is because Smux allocates more symbols than Smod to the same spatial domain.

2) Representative algorithms

There are several detection algorithms to estimate the transmitted signal, **x**(k), from a given received signal, **y**(k). The most straightforward method is zero-forcing (ZF) [65]. ZF is designed to suppress the cross channel interference by multiplying by the matrix, $\mathbf{C}_{zf}$, which is equivalent to the pseudo inverse, $\mathbf{H}^{\dagger}$, of channel matrix **H**. $\mathbf{C}_{zf}$ is given by:

$$\mathbf{C}_{zf}\ \boldsymbol{y}(k) = \mathbf{H}^{\dagger}\,\mathbf{H}\,\boldsymbol{x}(k) + \mathbf{H}^{\dagger}\,\boldsymbol{n}(\mathrm{k}) = \hat{x}(k) \tag{20}$$

However, ZF can be ineffective when a channel is 'ill-conditioned', due to the large estimation error and enhanced noise [65]. The estimated vector $\hat{x}(k)$ contains the remaining noise term, $\mathbf{H}^{\dagger}$ $\boldsymbol{n}$(k), whose covariance matrix is

$$\mathrm{E}[\ \mathbf{H}^{\dagger}\,\boldsymbol{n}(\mathrm{k})\boldsymbol{n}^{*}(\mathrm{k})\,\mathbf{H}^{\dagger *}\ ] = \sigma^{2}_{\mathrm{n}}\cdot(\ \mathbf{H}^{\dagger}\mathbf{H}^{\dagger *}) \tag{21}$$

where σ^{2}_{n} denotes the noise variance of each Rx element before applying the ZF algorithm. This expression assumes that noise of each receiver is uncorrelated, i.e. $\mathrm{E}[\ \boldsymbol{n}(\mathrm{k})\boldsymbol{n}^{*}(\mathrm{k})\ ] = \sigma^{2}_{\mathrm{n}}\mathbf{I}$, where **I** means the identity matrix. ('*' denotes conjugate transpose operator.) It can be seen that the pseudo inverse of channel covariance matrix ($\mathbf{H}^{\dagger}\mathbf{H}^{\dagger *}$) may enhance the total noise variance when the channel is ill-conditioned. For instance, when **H** is a perfectly uncorrelated M x M matrix, $\mathbf{H}^{\dagger}\mathbf{H}^{\dagger *}$ becomes **I**. Therefore the total noise variance, $\mathrm{tr}(\sigma^{2}_{\mathrm{n}}\mathbf{I})$, becomes $M\sigma^{2}_{\mathrm{n}}$. But, when **H** is highly correlated, $\mathbf{H}^{\dagger}\mathbf{H}^{\dagger *}$ becomes an almost singular matrix (**A**). Therefore, the total noise variance, $\mathrm{tr}(\sigma^{2}_{\mathrm{n}}\mathbf{A})$, tends to infinity.

The MMSE algorithm [65] is designed to minimise the interference and noise simultaneously so as to mitigate the noise enhancement. Given channel information and noise statistics, the solution matrix for MMSE ($\mathbf{C}_{mmse}$) is as follows.

$$\mathbf{C}_{mmse} = (\mathbf{H}^*\mathbf{H} + \sigma^2_n/\sigma^2_x \cdot \mathbf{I}_M)^{-1}\ \mathbf{H}^* \qquad (22)$$

where σ^2_x is the variance of transmitted signal and $\mathbf{I}_M$ denotes the M by M identity matrix. MMSE normally performs better than ZF, but when σ^2_n is 0 they perform equally, since the remaining term in (22), $(\mathbf{H}^*\mathbf{H})^{-1}\mathbf{H}^*$, simply represents the pseudo inverse $\mathbf{H}^{\dagger}$.

A better performing (but more complex) algorithm is maximum-likelihood-decoding (MLD) [66]. MLD uses channel knowledge to estimate all the possible received vectors given a particular modulation scheme. It then compares the received vector $\mathbf{y}(k)$, and the most probable transmitted vector $\boldsymbol{x}(k)$ out of all possibilities is chosen. The solution leading to the maximum probable $\boldsymbol{x}(k)$ is

$$\arg\min_{x_m} \| \boldsymbol{y}(k) - \mathbf{H}\, \boldsymbol{x}_m(k) \| \qquad (23)$$

where $\boldsymbol{x}_m$ represents all possible cases of transmitted vector. For instance, when the number of Tx is 3 and the modulation format is BPSK, $\mathbf{x}_m$ has 2^3 possibilities. The benefits of this technique are that the number of Rx (N) needs not to be more than that of Tx (M) since it does not require channel matrix inversion. However, when the number of Tx and constellation points increases, $\mathbf{x}_m$ has to be found by exhaustive search, resulting in exponentially increasing complexity.

Another approach is **V-BLAST** [67]. The algorithm first utilises ZF or MMSE to estimate an element of the transmitted vector $\mathbf{x}(k)$, then using knowledge of the channel $\mathbf{H}$, the interference caused by the estimated element is erased from $\mathbf{H}$. Subsequently, ZF or MMSE is again applied to

estimate another element **x**(k). This process keeps repeating until all components of **x**(k) are estimated. Meanwhile, optimal detection ordering (the order to estimate each component of **x**(k)) is carried out by monitoring the erased channel matrix. This ordering provides the best post-detection SNR.

4.1.2 A correlated MIMO-VLC channel model

There are a number of MIMO scheme-algorithm pairs, but the one that best suits a given MIMO-VLC channel is complex to determine. In RF, MIMO channels are normally assumed to be richly scattering, and thus identically and independently distributed (i.i.d) with complex-valued coefficients [68]. However, the VLC link is conventionally constructed of strong line of sight (LOS) paths with high directionality. Using IM-DD transmission leads to a highly spatially correlated channel with real-valued coefficients. The correlated channel may induce significant inter-channel interference causing severe performance degradation in a Smod and Smux based MIMO-VLC system.

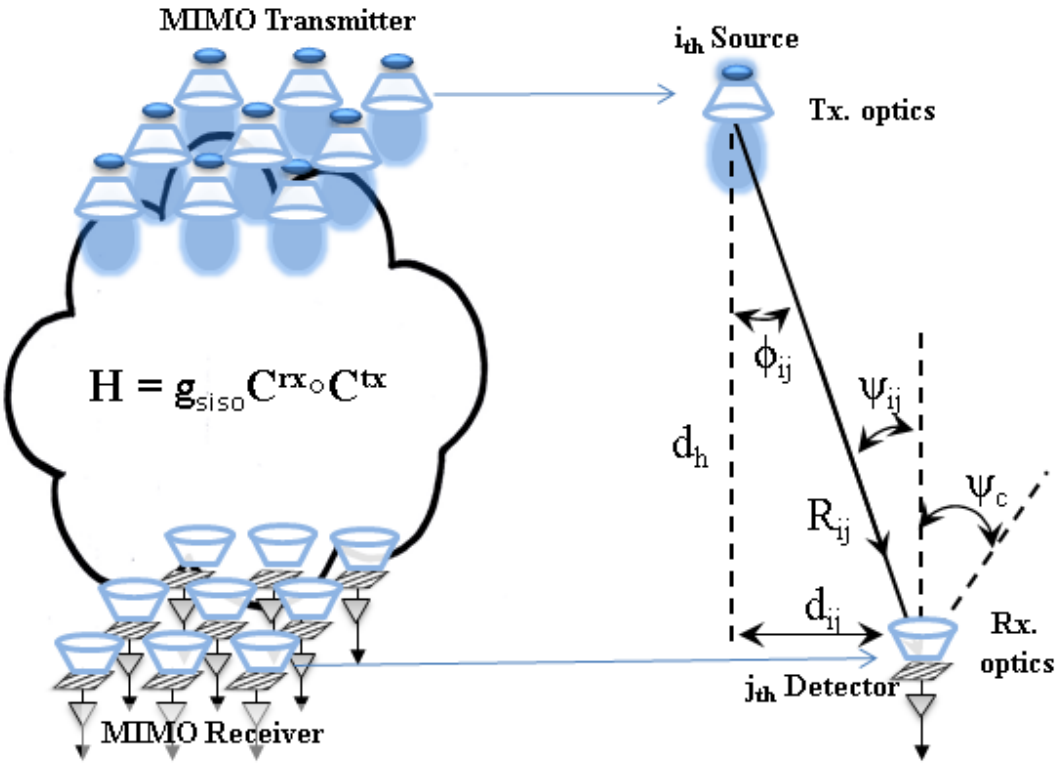

$$h_{ij} = \frac{(m_l + 1)}{2\pi R_{ij}^2} \cos^{m_l}(\emptyset_{ij}) \cos(\psi_{ij}) g(\psi_{ij})$$

h_{ij}: channel gain from i_{th} source to j_{th} detector
m_l: Lambertian mode number
R_{ij} : propagation distance
d_{ij} : horizontal distance between source and detector
d_h: vertical height
$\emptyset_{ij}$: radiation angle
ψ_{ij}: angle of incidence

Rx. optics gain: $g_{ij}(\psi) = \begin{cases} \frac{n^2}{\sin^2 \psi_c}, & 0 \le \psi_{ij} \le \psi_c \\ 0, & \psi_{ij} > \psi_c \end{cases}$

Ψ_c: FOV (half angle)

Figure 21. MIMO-VLC channel model

The MIMO-VLC channel depends on a number of variables, such as transmitter/receiver location, size, emission angle, receiver FOV and geometry. Reference [42][69] compared the

performance of Smux and Smod in non-imaging and imaging receiver cases. Reference [42] showed that in a low correlated channel Smux performs better, and in a high correlated channel Smod performs better, in a non-imaging receiver scenario. Reference [69] showed that for a low spectral efficiency schemes Smod performs better, and for a high spectral efficiency schemes Smux performs better, in an imaging receiver scenario. However, these investigations were conducted for several selected MIMO-channels, and it is difficult to generalise the results from such limited cases.

Figure 21 shows the MIMO-VLC channel model adapted here and presents how an individual channel is constructed. Each individual element of the channel matrix **H** is mostly determined by the source's Lambertian emission pattern and receiver's FOV dependent gain. In this analysis a correlated form of the H matrix shown in [70] is used, and modified to fit the MIMO-VLC environment.

$$\mathbf{H} = g_{siso}\, \mathbf{C^{rx}} \circ \mathbf{C^{tx}} \tag{24}$$

where g_{siso} is the constant making the maximum element of the H matrix unity. Using g_{siso} allows separate analysis of channel loss and cross-talk penalty, and enables a comparison between SISO and MIMO performance. $\mathbf{C^{tx}}$ represents the impact of the Lambertian emission profile determined by the radiation angle ($\emptyset_{ij}$) from a transmitter to a receiver. $\mathbf{C^{rx}}$ describes the impact of receiver FOV on the correlated MIMO-VLC channel. The FOV angle (ψ_c) can be represented by a critical distance (d_c). For instance, the i^{th} source is detected by the j^{th} detector only when the horizontal distance d_{ij} is less than d_c.

'$\circ$' is an element-wise multiplication operator.

References [42][69] chose several MIMO geometries, constructed H-matrices, and compared the performance of MIMO schemes. Therefore, it is difficult to generalise the results from such limited cases. However, a number of different combinations of d_h, d_{ij}, and m_l can lead to the same c_{ij}^{tx}, and the same H-matrix. In this thesis we use a single parameter, Kcorr, to describe a number of MIMO VLC channels. Kcorr allows more general conclusions to be drawn and a common understanding of MIMO performance for various geometries. $d_{ij,min}$ is the minimum horizontal separation between the i^{th} source and the j^{th} detector. $d'_{ij,min}$ and d'_h are unity. $\emptyset_{1/2}$ is half-angle making half the intensity from the source. Kcorr can be further simplified by using the small angle and log approximation.

It can be seen that there is a simple relationship between. $\emptyset_{1/2}$, d_h, and $d_{ij,min}$. This approximation was tested and verified for a wide range of cases, as set out below.

Figure 22, Figure 23, and Figure 24 show perfectly uncorrelated (case-i), partially correlated (case-ii), and completely correlated (case-iii) 4x4 MIMO-VLC channel matrices, respectively. Each example shows Kcorr, a number of transmitter/receiver geometries that can be described by the same Kcorr, their schematics, H-matrix, and corresponding condition number (an indicator of channel cross-talk). These examples show that Kcorr can characterise a wide range of MIMO-VLC channels.

- Kcorr < 0.07

- Geometry: (a) d_h=1m, d_{12}=d_{13}=1cm, d_{14}=√2cm, $\emptyset_{1/2} \leq 0.2^o$

(b) d_h=0.5m, d_{12}=d_{13}=1cm, d_{14}=√2cm, $\emptyset_{1/2} \leq 0.4^o$

(c) d_h=1m, d_{12}=d_{13}=10cm, d_{14}=10√2cm, $\emptyset_{1/2} \leq 2^o$

(d) d_h=0.5m, d_{12}=d_{13}=10cm, d_{14}=10√2cm, $\emptyset_{1/2} \leq 4^o$

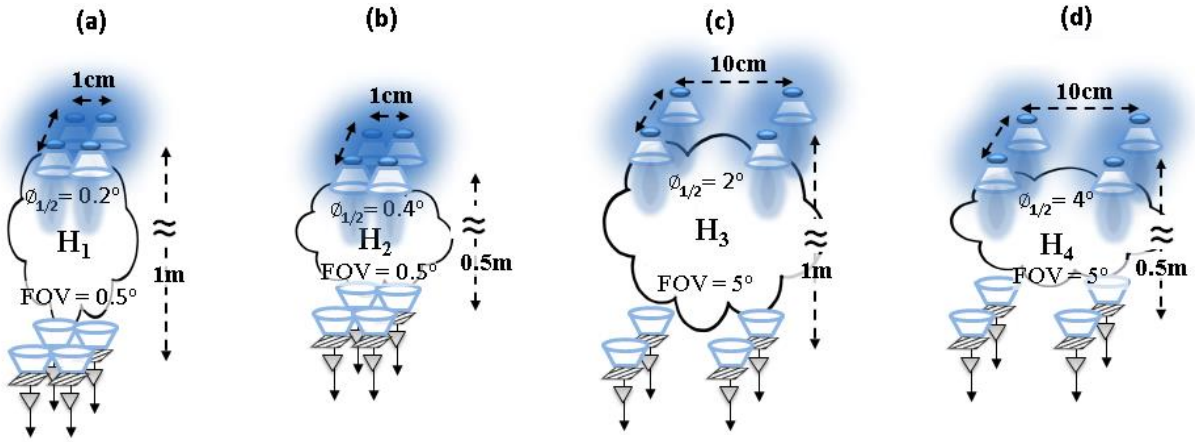

$$H_1 \approx H_2 \approx H_3 \approx H_4 \approx H$$

$$\mathbf{H} = g_{siso}\mathbf{C}^{rx} \circ \mathbf{C}^{tx} = g_{siso} \begin{pmatrix} 1 & 0 & 0 & 0 \\ 0 & 1 & 0 & 0 \\ 0 & 0 & 1 & 0 \\ 0 & 0 & 0 & 1 \end{pmatrix} \circ \begin{pmatrix} 1 & 0 & 0 & 0 \\ 0 & 1 & 0 & 0 \\ 0 & 0 & 1 & 0 \\ 0 & 0 & 0 & 1 \end{pmatrix} = g_{siso}\,\mathbf{I}$$

- Condition number = 1

Figure 22. Case-i: perfectly aligned and uncorrelated channel

- Kcorr = 1.5

- Geometry: (a) d_h=1m, d_{12}=d_{13}=1cm, d_{14}=√2cm, $\emptyset_{1/2}$ =1°

  (b) d_h=0.5m, d_{12}=d_{13}=1cm, d_{14}=√2cm, $\emptyset_{1/2}$=2°

  (c) d_h=1m, d_{12}=d_{13}=10cm, d_{14}=10√2cm, $\emptyset_{1/2}$=10°

  (d) d_h=0.5m, d_{12}=d_{13}=10cm, d_{14}=10√2cm, $\emptyset_{1/2}$=20°

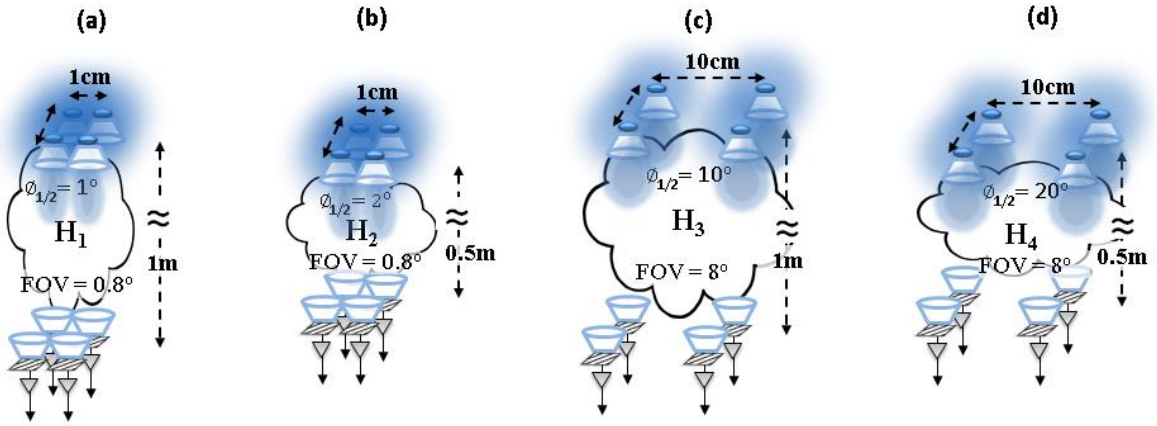

$$H_1 \approx H_2 \approx H_3 \approx H_4 \approx H$$

$$\mathbf{H} = g_{siso}\mathbf{C}^{rx} \circ \mathbf{C}^{tx} = g_{siso} \begin{pmatrix} 1 & 1 & 1 & 0 \\ 1 & 1 & 0 & 1 \\ 1 & 0 & 1 & 1 \\ 0 & 1 & 1 & 1 \end{pmatrix} \circ \begin{pmatrix} 1 & .79 & .79 & .69 \\ .79 & 1 & .69 & .79 \\ .79 & .69 & 1 & .79 \\ .69 & .79 & .79 & 1 \end{pmatrix}$$

$$= g_{siso} \begin{pmatrix} 1 & .79 & .79 & 0 \\ .79 & 1 & 0 & .79 \\ .79 & 0 & 1 & .79 \\ 0 & .79 & .79 & 1 \end{pmatrix}$$

- Condition number = 4.3

Figure 23. Case-ii: partially correlated channel by Lambertian emitters and FOV

- Kcorr > 38

- Geometry: (a) d_h=1m, d_{12}=d_{13}=1cm, d_{14}=√2cm, $\emptyset_{1/2}$>5°

(b) d_h=0.5m, d_{12}=d_{13}=1cm, d_{14}=√2cm, $\emptyset_{1/2}$>10°

(c) d_h=1m, d_{12}=d_{13}=10cm, d_{14}=10√2cm, $\emptyset_{1/2}$>50°

(d) d_h=0.5m, d_{12}=d_{13}=10cm, d_{14}=10√2cm, $\emptyset_{1/2}$>90°

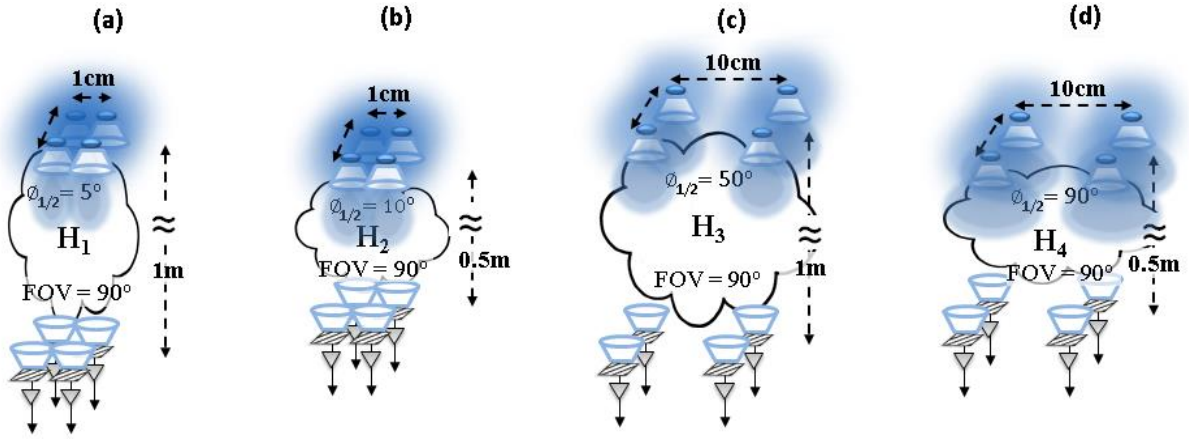

$$\boxed{H_1 \approx H_2 \approx H_3 \approx H_4 \approx H}$$

$$\mathbf{H} = g_{siso}\mathbf{C}^{rx} \circ \mathbf{C}^{tx} = g_{siso} \begin{pmatrix} 1 & 1 & 1 & 1 \\ 1 & 1 & 1 & 1 \\ 1 & 1 & 1 & 1 \\ 1 & 1 & 1 & 1 \end{pmatrix} \circ \begin{pmatrix} 1 & .99 & .99 & .99 \\ .99 & 1 & .99 & .99 \\ .99 & .99 & 1 & .99 \\ .99 & .99 & .99 & 1 \end{pmatrix}$$

$$= g_{siso} \begin{pmatrix} 1 & .99 & .99 & .99 \\ .99 & 1 & .99 & .99 \\ .99 & .99 & 1 & .99 \\ .99 & .99 & .99 & 1 \end{pmatrix}$$

- Condition number = 3997

Figure 24. Case-iii: completely correlated channel

As shown, a Kcorr represents a number of channel matrixes derived for a number of non-imaging receiver cases. Further work is required to investigate its applicability to the more complex imaging case. The simulations between the two cases suggest that this should be feasible.

4.1.3 Comparison of MIMO-VLC schemes and algorithms

As shown in the previous section, MIMO-VLC channels can be generalised by introducing a correlation coefficient, Kcorr. In this section, we compare the performance of MIMO schemes and algorithms with channels that have different Kcorr. For comparison of the three representative schemes (ganging / Smod / Smux), we limit our investigation to MLD (most complex) and ZF (least complex). Table 9 shows the spectral efficiency of the three MIMO-VLC schemes compared to the SISO case, and Table 10 presents their BER expressions.

Table 9. Spectral efficiency of selected MIMO schemes

Schemes	**Ganging**	**Smod**	**Smux**
Spectral efficiency	1	Log_2 (M)	M

*M: Number of transmitters

.

.

Table 10. BER expressions of selected *L*-PAM based MIMO-VLC system

Algorithm \ Scheme	MLD	ZF
Ganging	BER $\simeq$ $$\mathrm{Q}\left(\sqrt{\frac{\mathrm{SNR_{SISO}}}{\mathrm{M^2N\,(L-1)^2}}\left(\sum_{\mathrm{n}}\sum_{\mathrm{m}}\|\|h_{nm}\|\|\right)^2}\right)$$ (27)	
Smod	BER $\simeq$ (28) $$\underbrace{\frac{1}{\mathrm{LM\log_2 LM}}\cdot\sum_{i=1}^{\mathrm{LM}}\sum_{j=1}^{\mathrm{LM}}\left\{\mathrm{d_H(b_i,b_j)\,Q(\cdot)}\right\}}$$ $$\mathrm{Q}\left(\sqrt{\gamma_{\mathrm{Smod}}\cdot\mathrm{SNR_{SISO}}\sum_{\mathrm{n}}\|\|\mathbf{H}\cdot(\mathbf{S_i}-\mathbf{S_j})\|\|^2}\right)$$	BER $\simeq$ (30) $$\mathrm{Q}\left(\sqrt{\frac{\gamma_{\mathrm{Smod\_ZF}}}{(\mathrm{L}-1)^2}\cdot\mathrm{SNR_{SISO}}}\right)$$

Smux	BER $\simeq$ (29) $\frac{1}{\mathrm{L^M}\log_2 \mathrm{L^M}} \cdot \sum_{i=1}^{\mathrm{L^M}} \sum_{j=1}^{\mathrm{L^M}} \{ \mathrm{d_H}(\mathrm{b_i}, \mathrm{b_j})\, \mathrm{Q}(\cdot) \}$ $\mathrm{Q}\left(\sqrt{\gamma_{\mathrm{Smux}} \cdot \mathrm{SNR_{SISO}} \sum_{\mathrm{n}} \lvert\lvert \mathbf{H} \cdot (\mathbf{S_i} - \mathbf{S_j}) \rvert\rvert^2} \right)$	BER $\simeq$ (31) $\mathrm{Q}\left(\sqrt{\frac{\gamma_{\mathrm{Smux\_ZF}}}{(\mathrm{L}-1)^2} \cdot \mathrm{SNR_{SISO}}} \right)$

- M: Number of transmitters; N: Number of receivers; m: transmitter index; n: receiver index;
- h_{nm}: (n^{th} row, m^{th} column) element of MIMO channel; SNR_{siso}: SISO SNR; L: PAM level;
- γ_{Smod}: Smod coefficient; γ_{Smux}: Smux coefficient; $\gamma_{ZF}^{penalty}$: Zero-forcing penalty $\|\cdot\|$: Frobenius norm

Ganging schemes aim to achieve higher SNR than can be achieved by SISO. The receiver sums the electrical amplitude from all channels. Each source emits 1/*M* optical power to have the same total output power as the SISO case. The noise variance increases by factor of *N*. As expected, (27) shows that if the MIMO channel constructs an identity H-matrix, SNR can be reduced by a factor of *N* compared to SISO since *N* times more receivers cause *N* times lower SNR. However, when the MIMO channel constitutes a highly spatially correlated H-matrix, then ganging scheme achieves *N* times higher SNR (when $N = M$) than the SISO case.

Smod normally uses an MLD algorithm [62], and (28) shows the union bound BER approximation. In Smod, there are $L \cdot M$ different symbols, and the equation shows summations of symbol error probabilities, and by the number of corresponding error bits, over all $L \cdot M$ possible symbols. γ_{Smod} indicates the penalty caused by generating Smod symbols.

This penalty is because one of the sources has to be turned on at any one time for a spatial index to be encoded. Hence, the modulation depth has to be reduced, possibly causing considerable penalty. Unlike [42][69] using fixed modulation depth reductions of $L/(L+1)$ for L-PAM based Smod, the optimum reduction factors can be significantly changed by the degree of MIMO channel correlation, and this factor sets γ_{Smod} of MLD based Smod.

Figure 25 shows the optimum peak to peak reduction factor of 2-PAM based Smod, found by using (28) for a number of MIMO-VLC channels represented by Kcorr. As shown, if the MIMO channel constructs a near identity matrix (Kcorr = 0.1), the peak to peak amplitude has to be reduced by 60%. When the MIMO channel constitutes a highly correlated matrix (Kcorr = 10), the optimum peak to peak amplitude reduction is 95%. This means that decoding the spatial index for a higher degree of channel correlation demands a higher minimum L-PAM signal level.

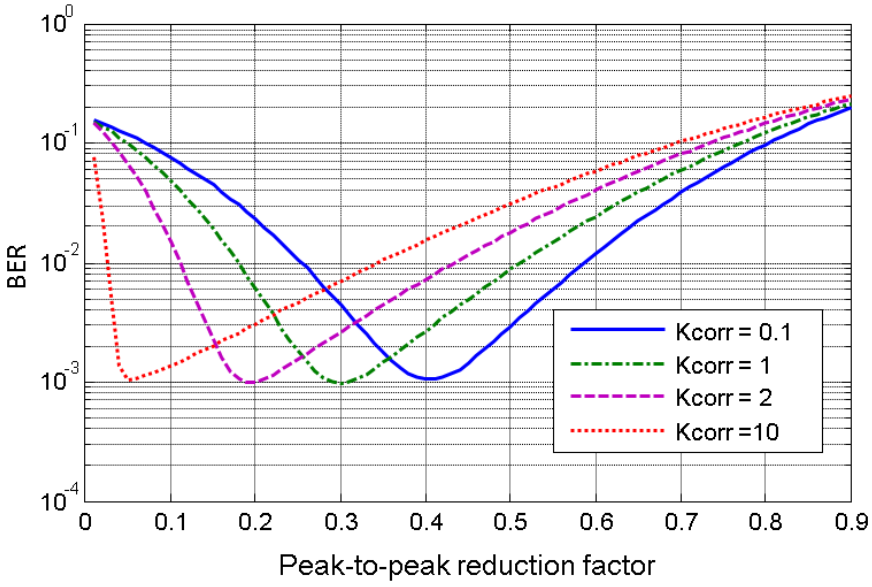

Figure 25. BER versus peak-to-peak reduction factor in 2-PAM based Smod for different degrees of MIMO channel correlation

Table 11. Optimum peak-to-peak reduction factors

	Kcorr = 0.1	Kcorr = 0.2	Kcorr = 1	Kcorr = 2	Kcorr = 5	Kcorr = 10	Kcorr = 20	Kcorr = 100	Values used in [42][69]
2-PAM	0.4	0.39	0.3	0.19	0.09	0.05	0.03	0.005	0.67
4-PAM	0.68	0.66	0.55	0.42	0.24	0.11	0.08	0.015	0.8
16-PAM	0.92	0.91	0.87	0.8	0.63	0.38	0.31	0.069	0.94
64-PAM	0.98	0.98	0.96	0.95	0.88	0.73	0.64	0.24	0.98

Table 11 shows the optimum peak-to-peak reduction factors for *L*-PAM based Smod. It is seen that higher order multi-level PAM schemes require less peak-to-peak reduction. This is because the possibility of errors caused by the reduced minimum Euclidean distance becomes comparable to the possibility of errors caused by the higher order *L*-PAM.

Smux can be decoded using MLD, which does not bring about noise enhancement, as generally happens in linear channel inversion approaches. Equation (29) shows the union bound BER approximation of MLD based Smux. In Smux, there are L^M different symbols, and the equation shows the same pair-wise comparison based calculation as used in Smod, but this time the summation is done over all L^M symbols. γ_{Smux} indicates the penalty caused by applying Smux. Smux turns on all light sources at the same time like ganging, leading to the optical power reduction by 1/*M*. Therefore, γ_{Smod} becomes simply 1/*M*.

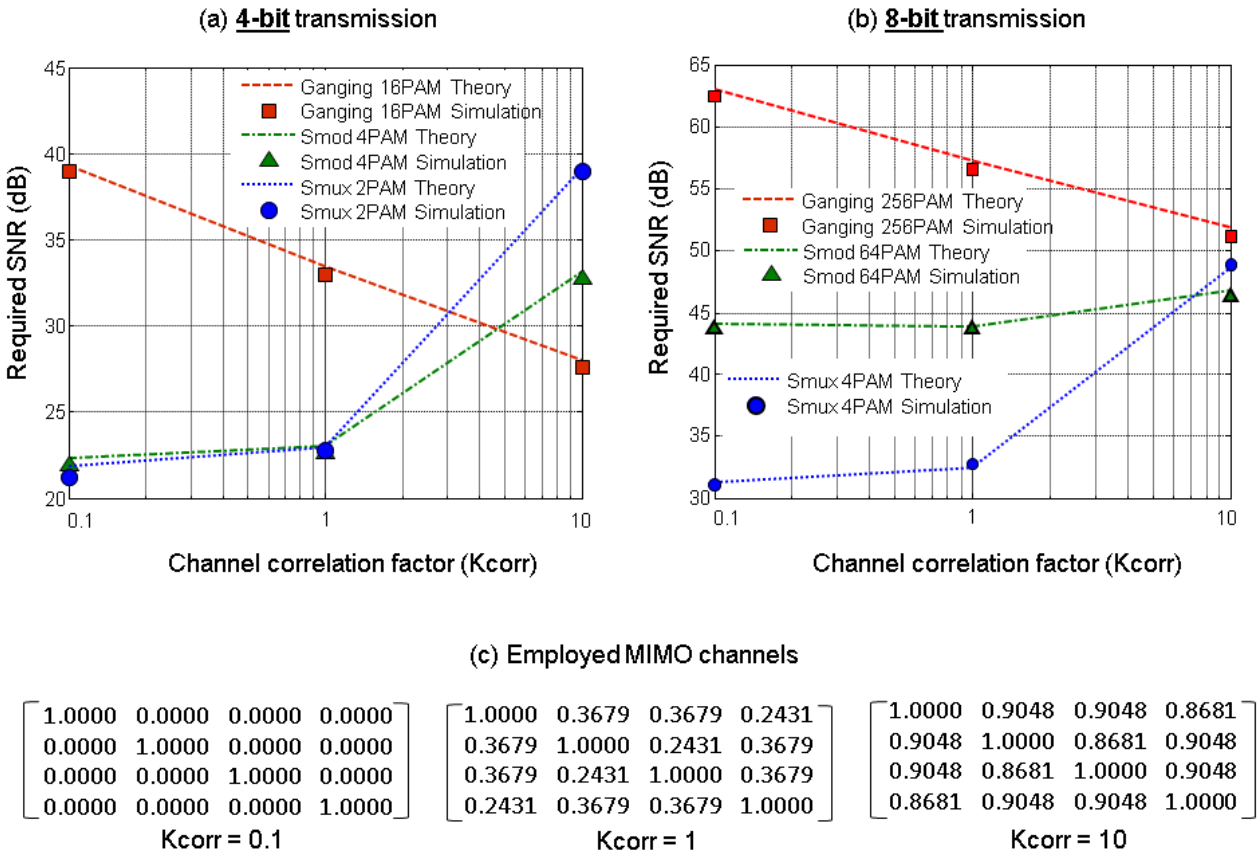

Figure 26. Required SISO SNR (dB) of MLD based ganging, Smod, and Smux schemes for (a) 4-bit transmission and (b) 8-bit transmission, and (c) considered 4x4 MIMO channels.

Figure 26 shows the comparison among the three schemes: ganging, Smod, and Smux in 4 x 4 MLD systems. Required SNRs are obtained by the equations in Table 10 and Monte-Carlo simulation. The spectral efficiency is equally set to 4-bit and 8-bit for all three schemes. For instance, for a spectral efficiency of 4 bits/symbol, ganging requires 2^4 levels of modulation, Smod requires 2^2 levels of modulation, and Smux requires 2 levels of modulation. Figure 26 (a) shows the case of 4-bit transmission and (b) shows the case of 8-bit transmission. Figure 26 (c) shows the considered channel matrix. Smux demands the lowest SNR for a low Kcorr of 0.1, which is

constituted mostly of LOS SISO channels. However, Smux requires the highest SNR in a highly correlated channel (Kcorr = 10), for both 4-bit and 8-bit cases. Smod demands lower SNR than Smux in this high Kcorr for both these also. This is because the correlated channel has less influence on Smod than Smux as symbols from sources are turned on one at a time. In 8-bit transmission, the multi-level penalty of ganging becomes more significant and the non-zero intensity constraint of Smod becomes less significant. This makes Smod perform the best of the schemes at a high Kcorr (=10) for these reasons. Ganging requires lower SNR as Kcorr increases as it has more power to sum (compared to SISO). Ganging demands the lowest SNR at a Kcorr of 10 in 4-bit transmission case.

These results imply that when the MIMO system has a small channel correlation, Smux is the appropriate scheme, and for highly correlated channel, either ganging or Smod becomes the optimum scheme depending on the degree of correlation and/or the spectral efficiency. This analysis assumes the use of MLD, which optimally decodes MIMO signals. However, the number of possible symbols for the pair-wise comparison required in MLD increases rapidly as the number of sources increases. This constraint is true for both MLD based Smod and Smux, since Smod has to have a larger symbol set for the same spectral efficiency as Smux.

Table 12. Penalty induced by inverting MIMO-VLC channel

	Kcorr = 0.1	Kcorr = 0.2	Kcorr = 1	Kcorr = 2	Kcorr = 5	Kcorr = 10	Kcorr = 20	Kcorr = 100
Penalty (dB) Theory	0	0	2.8	7.1	14.3	20.1	26	40
Penalty (dB) Simulation	0	0	2.9	7	14.3	20.1	26	39.9
Condition number	1.0002	1.0273	3.9004	9.6645	29.1891	62.9236	130.982	677.064

Linear matrix inversion such as ZF can be used as an alternative. Assuming that the MIMO-VLC channel does not change much between channel estimates, the computational cost of the matrix inversion can be relatively small compared with MLD. After the matrix inversion each data stream can be treated as a SISO channel with a corresponding penalty, $\gamma_{\mathrm{Smod\_ZF}}$ for Smod and $\gamma_{\mathrm{Smux\_ZF}}$ for Smux. These penalties are obtained using the same total optical output constraint for Smux and peak-to-peak reduction factor for Smod, respectively.

However, when inverting the MIMO channel using ZF, Smux and Smod experience the same amount of noise enhancement. The enhanced noise power in ZF output ($\sigma^2_{\mathrm{noise\_after\_ZF}}$) can be calculated as [71]

$$\sigma^2_{noise\_after\_ZF} = \mathrm{E}\left[\frac{\sigma^2_{noise\_before\_ZF}}{\sigma^2_m}\right] \tag{32}$$

,where σ^2_m denotes the m^{th} squared singular value of channel matrix H. Table 12 summarises the calculated and simulated ZF penalty and condition number of the 4x4 MIMO channel with different Kcorr.

Figure 27 shows the required SISO SNR for ganging, Smod, and Smux schemes in the 4x4 MIMO system using ZF for channel inversion. Required SNRs are obtained from equations in Table 10 and Monte-Carlo simulation. The spectral efficiency is equally set to 4-bit and 8-bit for all three schemes. Figure 27 (a) shows the case of 4-bit transmission and (b) shows the case of 8-bit transmission. Figure 27 (c) shows the considered channel matrix. ZF based Smod does not perform as well as MLD based Smod. This is due to i) the same ZF penalty as Smux, ii) an

additionally required comparator after the ZF to decide the spatial index, iii) the signal peak-to-peak amplitude reduction, and iv) the higher number of modulation levels required to match the spectral efficiency of Smux. Therefore, it can be seen that Smux always demands less SNR than Smod, and ganging requires the least in the highly correlated channel.

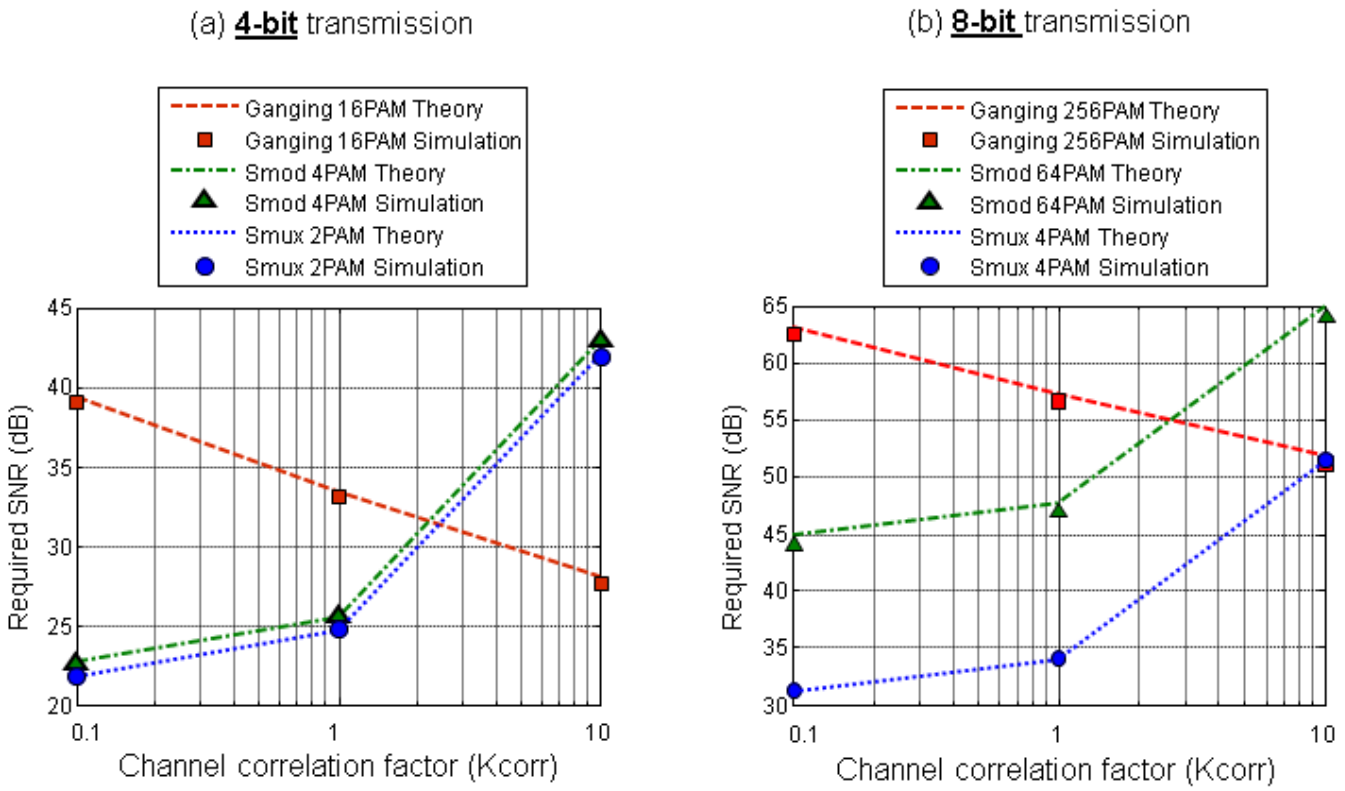

Figure 27. Required SISO SNR (dB) of ZF based ganging, Smod, and Smux schemes for (a) 4-bit transmission and (b) 8-bit transmission, and (c) 4x4 MIMO channels.

Chapter 5
Optimised VLC System Design and Examples

5.1 INTRODUCTION

As shown throughout the previous chapters, there are a number of communication schemes and devices, requiring and providing different SNR and BW. Figure 28 summarises all the VLC schemes and techniques discussed, by plotting the required SNR and BW of selected cases. The requirements are normalised with respect to those of OOK. OOK needs an SNR of 9.8 dB for BER of 10^{-3}, and $\frac{\mathrm{DR}}{\mathrm{P_{optical}}}$ of 2 is assumed unless labelled otherwise. In such cases ∞ DR is used. There are a number of interesting observations.

1. A link using devices with K^{-1}_{system} of 3 shows considerable SNR margin improvement for almost all schemes as the BW reduces. The margin declines in a shot-noise dominant link.
2. However, the SNR margin improvement can be limited by practical system constraints. For example, for K^{-1}_{system} of 3, reducing the BW below 29 % and 24% is not helpful in a 7-bit and 8-bit resolution system, respectively. This is because the maximum system SNR is limited by the quantisation noise of the DACs.
3. For a K^{-1}_{system} of 1 and in a shot-noise dominant case, *L*-PPM is optimal when the system has enough dynamic-range to take advantage of *L*-PPM's outstanding power efficiency.

4. The best scheme depends on channel frequency response. It is observed that when -60 dB/dec LPF channel with relative BW greater than 0.15 is assumed, OOK with DFE requires the smallest SNR. When below 0.15, bit/power loaded DCO-OFDM demands the smallest SNR.
5. The effectiveness of ganging and MIMO schemes (ZF based Smod and ZF based Smux) can be incorporated into the graph. As shown in the inset, the reference OOK point is shifted according to the correlation factor, Kcorr, and a comparison with other SISO cases can be made after this reference shift.

   For example, for a low MIMO channel correlation (Kcorr = 0.1), 4x4 Smux requires an SNR of 22 dB. SISO 16-PAM has the same spectral efficiency as 4x4 Smux, and it requires an SNR of 27dB, and thus 4x4 Smux is preferred. However, for a high correlation (Kcorr = 10), a 4x4 Smux requires an SNR of 33 dB. Therefore, SISO 16-PAM is preferred.

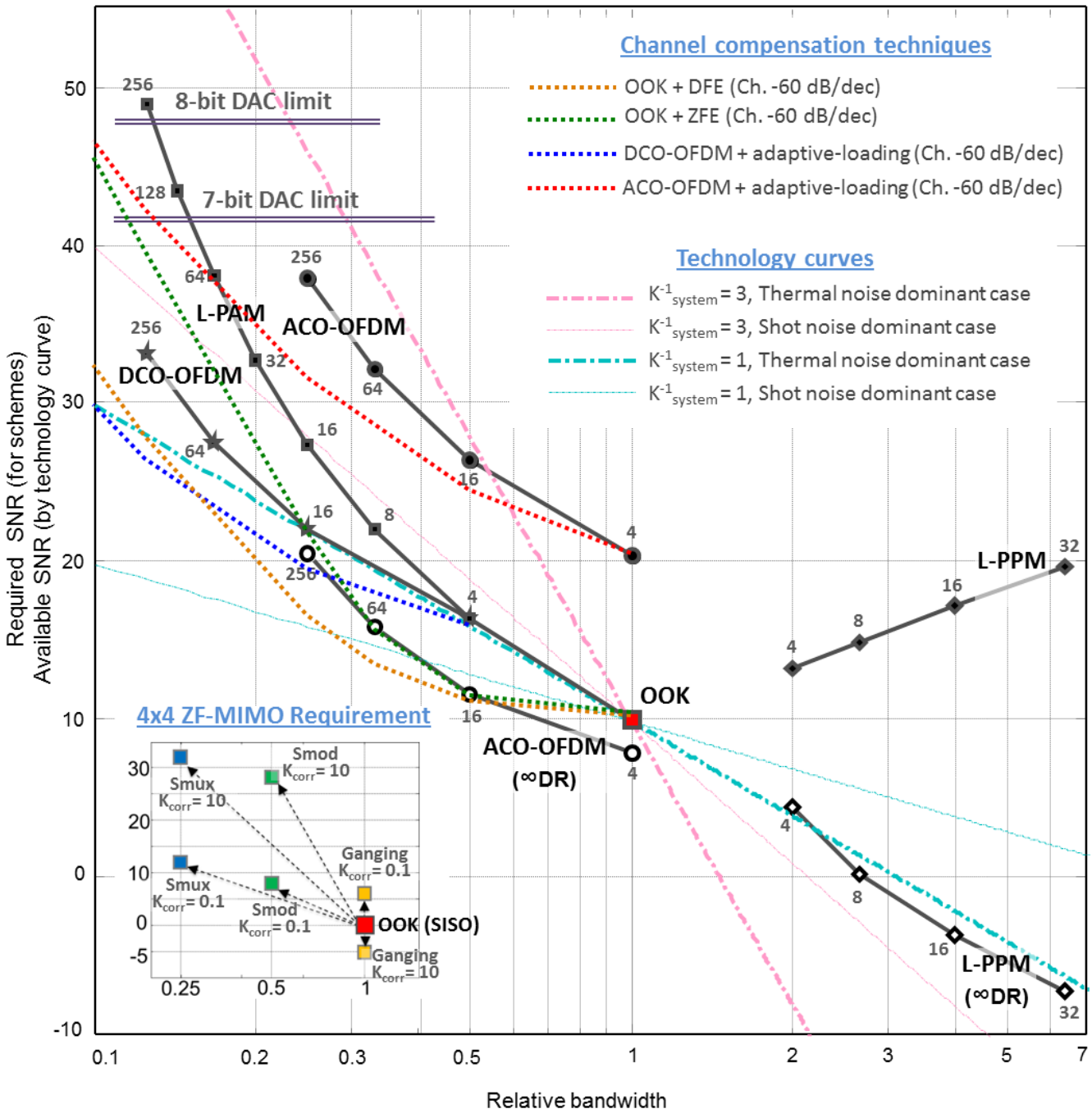

Figure 28. SNR and BW requirements for various VLC schemes and techniques compared to OOK demanding SNR of 9.8 dB for a BER of 10^{-3}

It can be seen that the optimum scheme depends on the particular type of device used for transmitter and receiver, and the relationship between SNR and BW. In this section, two examples of constructing multi Gbit/s VLC systems are presented.

The first example explains the design method for an information broadcasting system. Multiple sources are used to broadcast the same information and a single detector is used for the signal reception. The maximum achievable data-rate rate is found under given constraints.

The latter presents the design method for a 4 (sources) by 4 (detectors) MIMO module. In this example the target data-rate is given and the optimum conditions such as modulation scheme and source/detector size are found.

5.1.1 (Design Task-I) Information broadcasting system design

Table 13 shows the specifications of different elements and the tasks required.

Table 13. Design Task-I

"Given conditions below, design the fastest VLC based broadcasting system in a typical room"		
Illumination scenario		**Figure 2**
Transmitter	Source type	WLEDs (phosphor + GaN LED)
	Total luminous flux	5000 lumen
	B/W and power of individual source	To be determined by 'technology curve'
	Divergence angle	120^{o} (full)

Receiver	Detector type	APD (Hamamatsu S8664 series)
	B/W and active detection area	To be determined by 'technology curve'
	Receiver noise	10pA/√Hz
	Coverage area	5m x 5m
	FOV	90º (full)
Other constraints	DAC resolution	8 bit
	Noise property	AWGN
	Blue-filtering loss	3 dB (optical)
	Frequency response slope	-60 dB / decade

The design steps are as follows.

<Step-1> Draw the technology curve.

1) The total luminous flux from all WLEDs are fixed by the given illumination requirements. Therefore, the technology curve only includes the APD properties. The number of LEDs needed for the illumination level and BW can be calculated once the optimised BW is found.
2) Condition-i) WLDEs are composed of phosphor and blue GaN LED, and the blue component follows the power-bandwidth relationships derived from GaN μLEDs shown in Figure 17-(a).
3) Condition-ii) APD with area-bandwidth relationships of Hamamatsu S8664 series is considered as shown in Figure 17-(b).

   Then,

$$\mathrm{SNR}_{\mathrm{gain}} = \begin{cases} \Delta\mathrm{BW}_{\mathrm{system}}^{-\frac{2}{0.59}}, & \text{Thermal noise limit} \\ \Delta\mathrm{BW}_{\mathrm{system}}^{-\frac{1}{0.59}}, & \text{Shot noise limit} \end{cases} \quad (40)$$

<Step-2> Prepare curves of signal and noise variance by OOK data-rate.

Using the information in Table 13 and the area-bandwidth relationships of the photodiode, the relative signal and noise variance are obtained according to the applied OOK data-rate. From Figure 29, it can be seen that the system is mostly thermal noise limited. The SNR can be calculated by subtracting the dominant noise variance from the signal variance.

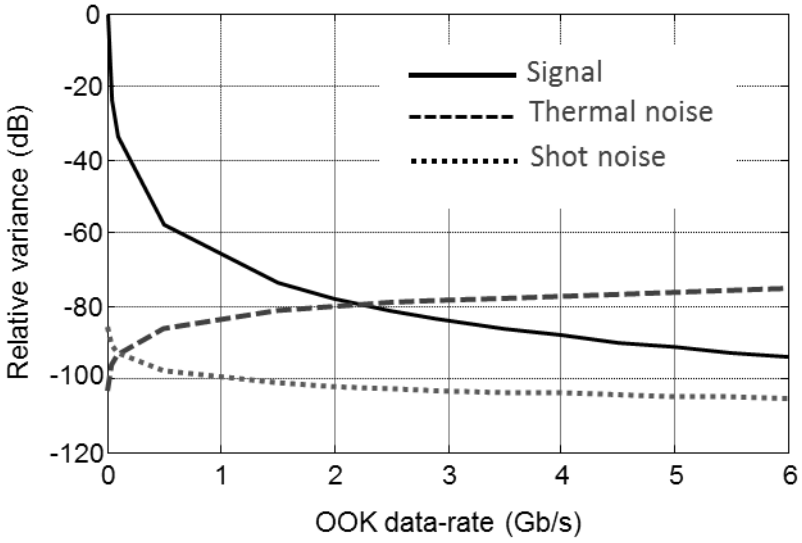

Figure 29. Relative variance of signal, and thermal and shot noise according to OOK data-rate

<Step-3> Locate the technology curves at the point where they are tangential to the requirement curve of the communication schemes.

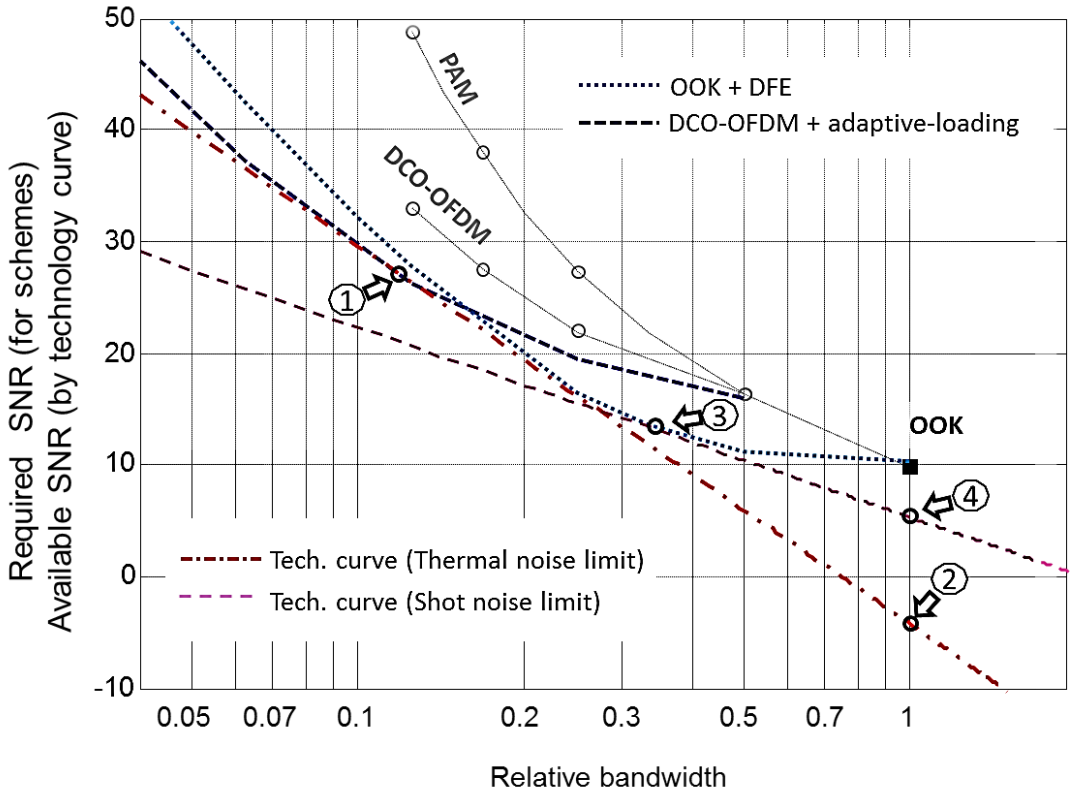

Figure 30. Required SNR vs relative BW, given selected communication schemes

1) Thermal noise limited operation,

The technology curve meets the curve of DCO-OFDM with adaptive loading at ① where the relative BW is 0.12. This means that this scheme operates even though the SNR for the OOK is -4.5 dB (at ②)

2) Shot noise limited operation,

The technology curve meets the curve of OOK with DFE at ③ where relative BW is 0.33. This means that this scheme operates even though the SNR for OOK is 6 dB (at ②).

<Step-4> Identify the optimum conditions and find out the maximum data-rate.

As shown in Figure 29, the system noise is mostly thermal noise. Therefore,

1) The optimum modulation scheme is DCO-OFDM with adaptive loading, which uses a BW of 8.3 (=1/0.12) times higher than the available BW.

2) The achievable data-rate is 2.9 Gb/s at which the OOK SNR becomes -4.5 dB in Figure 29.

3) The optimised detector bandwidth is 350 MHz (=0.12 x 2.9 GHz). This bandwidth is obtained by having a detector size of 0.7 mm^2 according to the technology curve of the Hamamatsu S8664 series.

5.1.2 (Design Task-II) 4 x 4 MIMO module design

Table 14 shows the design task and given conditions.

Table 14. Design Task-II

"Given conditions below, design a 4x4 MIMO VLC module supporting 10 Gb/s at 1m distance"		
MIMO	Scheme	Non-imaging Spatial multiplexing (Smux)
	Dimension	4 channels (4 transmitters, 4 receivers)
	Decoding algorithm	Zero-forcing (ZF)
	Size of module	< 50 cm^2
Transceiver properties	Source type	GaN μLED

	Beam divergence angle	10^{o} (full)
	Detector type	APD (Hamamatsu S8664 series)
	FOV	10^{o} (full)
Other constraints	Same as Design Task-I (see Table 13)	

The design steps are as follows.

<Step-1> Choose suitable transceiver geometry

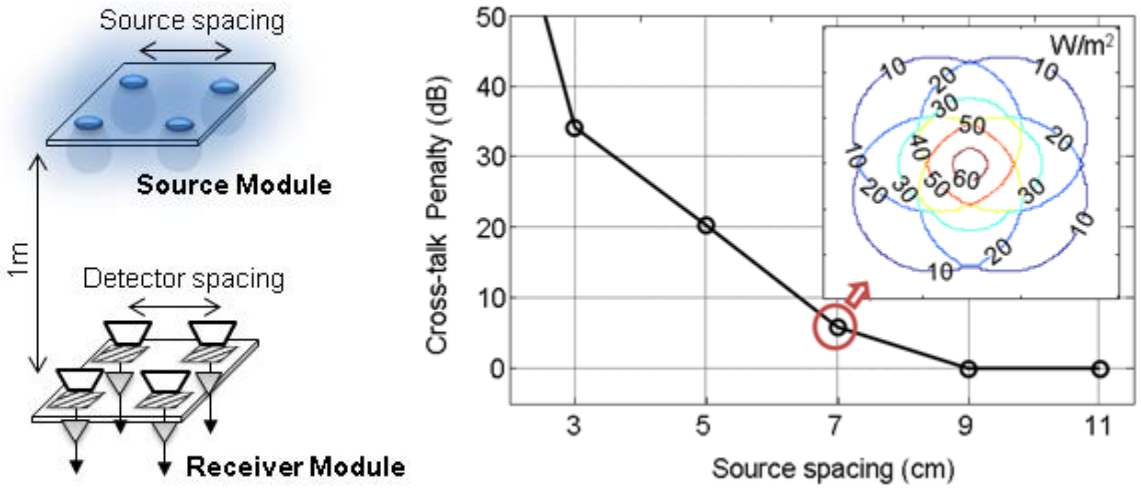

Figure 31. Zero-forced spatial multiplexing cross-talk penalty vs. source spacing

Figure 31 shows the 4x4 MIMO modules and the cross-talk penalty by the source spacing. The link distance is 1m, and beam divergence angle (full) and receiver FOV (full) is 10^{o}. The graph shows that a larger area module allows less cross-talk between channels. (The detector spacing is assumed to be the same as the source spacing.) The penalties are calculated by using the simulated

irradiance distribution and equation (32) for the case of zero-forcing algorithm. It is shown that a source spacing of 7cm leads to a penalty of 5.7 dB while meeting the size constraint.

<Step-2> Given conditions, determine the technology curve.

1) The source power-bandwidth relationship follows the curve derived from GaN μLEDs shown in Figure 17-(a).
2) An APD with area-bandwidth relationships of Hamamatsu S8664 series is considered as shown in Figure 17-(b).

Then,
$$\mathrm{SNR}_{\mathrm{gain}} = \begin{cases} \Delta \mathrm{BW}_{\mathrm{system}}^{-2\left(\frac{1}{0.59}+\frac{1}{0.6}\right)}, & \text{Thermal noise limit} \\ \Delta \mathrm{BW}_{\mathrm{system}}^{-\left(\frac{1}{0.59}+\frac{1}{0.6}\right)}, & \text{Shot noise limit} \end{cases} \quad (40)$$

<Step-3> Prepare curves of signal and noise variance by OOK data-rate.

Using the information in Table 13 and Table 14, the area-bandwidth relationships of Hamamatsu S8664 series, and power-bandwidth relationships of GaN μLEDs, relative signal and noise variance are obtained for each OOK data-rate. The SNR can be calculated by subtracting the signal variance from the dominant noise variance. When 10 Gb/s OOK is applied, the SNR becomes -75 dB.

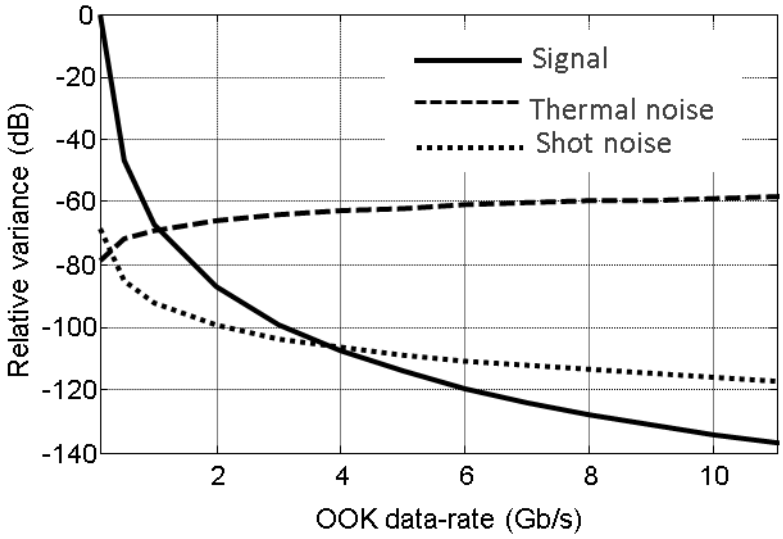

Figure 32. Relative variance of signal, and thermal and shot noise according to OOK data-rate

<Step-4> Locate the technology curves.

1) Relocate the requirement curves.

   As shown at ①, the MIMO OOK reference relative to SISO OOK reference can be obtained by applying the zero-forcing penalty calculated in <Step-1>.

2) In the case of shot noise limited operation,

   The technology curve meets the curve of DCO-OFDM with adaptive loading at ② where BW relative to SISO OOK is 0.03. It means that this scheme works even though SNR for SISO OOK is -19 dB (at ③). However, as calculated in <Step-2>, when applying 10 Gb/s of SISO OOK, -75 dB SNR (at ④) is expected. Therefore, this case cannot support the data-rate, as it is. If there is an initial SNR margin of 56 dB, 10 Gb/s becomes possible. The most straightforward way without compromising other

optimisations is to assign more uLEDs per channel. For the 56 dB, however, about 40k units are required per channel. This number is impractical. Therefore, more parallel channels may be required for 10 Gb/s.

3) In the case of thermal noise limited operation,

From Figure 32**,** it can be seen that the system is mostly thermal noise limited. In this case, DCO-OFDM with adaptive loading can support a SISO OOK SNR of -75 dB. By placing the technology curve at ④, the available margin can be calculated. An 8 bit resolution system with an SNR upper bound = 48.1 dB is assumed in this system. The maximum margin is obtained at the relative bandwidth of 0.015 (at ⑤) where the technology curve meets the upper bound. The gap between the available SNR and the required SNR at the bandwidth is 5 dB. This value becomes the margin.

<Step-5> Identify the optimum communication scheme, source and detector parameters for the 10 Gb/s 4x4 MIMO system.

1) The optimum modulation scheme is DCO-OFDM with adaptive loading, which uses a BW of 150 MHz (=0.015 x 10 GHz).

2) For the BW, the optimised detector size is 2.77 mm^2 and the optimised source power is 1.1 mW, according to the technology curves of Hamamatsu S8664 series and GaN μLEDs.

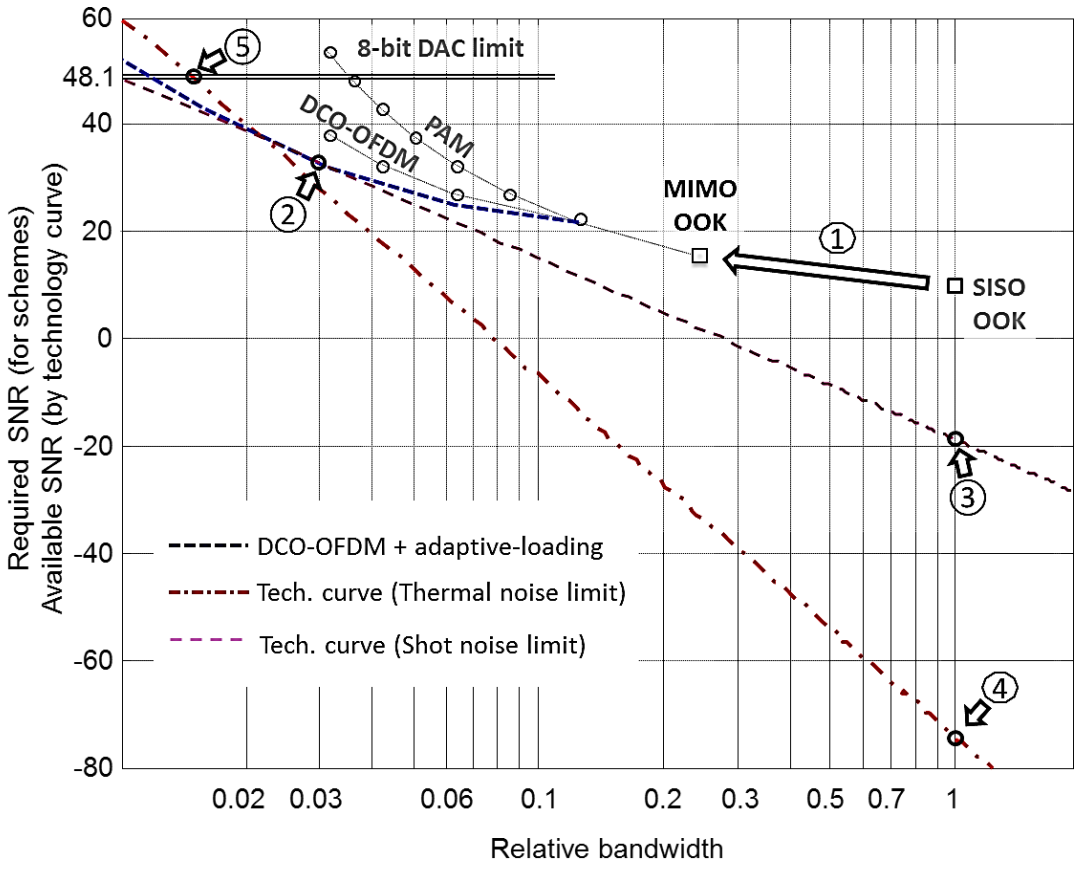

Figure 33. Required SNR vs relative BW, given selected communication schemes for the 4x4 MIMO system described in Table 14

5.2 CONCLUSIONS

In this chapter, two VLC system design examples were introduced, in order to demonstrate the optimisation of design parameters given practical constraints and targets. The first example considered an illumination constraint. A maximum achievable data-rate of 2.9 Gb/s was found by using adaptively loaded DCO-OFDM with a modulation BW of 350 MHz. The second example showed an optimised design of 10 Gb/s 4x4 MIMO VLC module. The largest SNR margin of 5 dB was achieved by using adaptively loaded DCO-OFDM with a modulation BW of 150 MHz.

Chapter 6
Multi-Gigabit/s VLC system demonstrations

6.1 INTRODUCTION

This chapter presents several practical demonstrations of multi-Gb/s VLC systems. Three systems, published in [33][34][73], are introduced. It was not possible to apply the technology curve based optimisation introduced in the previous chapter in these cases due to the limited choice of experimental devices. However, comments, and comparison with the optimum, are given where relevant.

6.2 A 3 GIGABIT/S VLC LINK USING A GALLIUM NITRIDE µLED

In this section, the communication capabilities of Gallium Nitride µLEDs in conjunction with OFDM are investigated. OFDM is selected because as shown in chapter 3, OFDM can outperform other modulation schemes when the SNR is sufficient to modulate the LED at >10 times the available BW. The channel conditions shown later in this section indicate that this system meets this criterion. Moreover, the scheme is robust to low-frequency interference caused by ambient light and by the baseline wander in electrical components. A performance comparison is also made between fixed-rate data loading with pre-equalisation and adaptive bit/power loading.

6.2.1 System descriptions

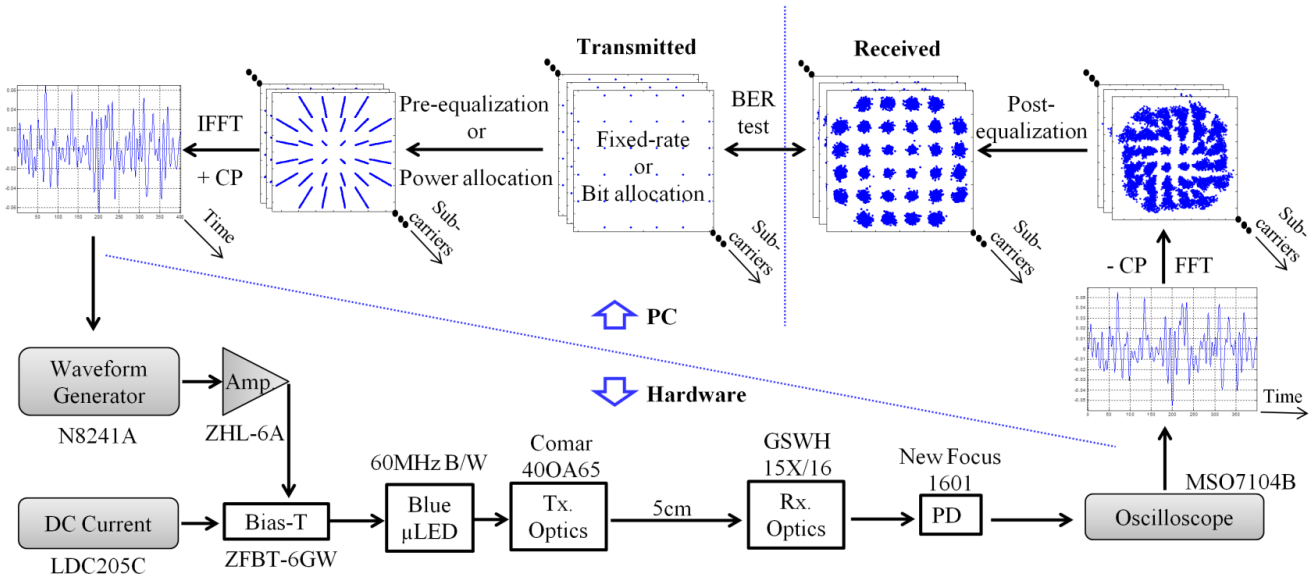

Figure 34. Experimental set-up

Figure 34 shows a diagram of the experimental set-up. Firstly, an incoming bit stream is encoded into *M*-QAM symbols. Secondly, the symbols are assigned to different subcarriers and rescaled when pre-equalisation is employed. Afterwards, an IFFT operation is applied on a block of symbols which produces a discrete time-domain signal. This signal is conditioned for transmission by clipping any peaks outside the dynamic range set by the electrical characteristics of the µLED.

All digital processing steps are performed using MATLAB®. Then, the conditioned signal is supplied to an arbitrary waveform generator (AWG), Agilent N8241A, which assigns it to an analogue signal. This is amplified with a high-power amplifier (Mini-Circuits ZHL-6A) which

drives the µLED. The µLED emits blue light with a wavelength distribution centered at ~450 nm and has a maximum optical power of approximately 4.5 mW. This µLED was supplied by Strathclyde University, a UP-VLC project partner. A DC bias from a laser driver is added to the drive signal using a bias-T (Mini-Circuits ZFBT-6GW). Light from the µLED is imaged onto a high-speed photo-detector (New Focus 1601FS-AC) using a high numerical aperture (NA) microscope objective (Comar Optics 40OA65). The output signal of the photo-detector is captured by a digital oscilloscope (Agilent MSO7104B). Afterwards, it is processed in MATLAB® with a sequence of steps that include: synchronization, FFT, equalisation, and M-QAM demodulation. QAM mapping and de-mapping were undertaken using an efficient algorithm supplied by Edinburgh University, and the other algorithms were developed here as part of by the author thesis. The distance between the transmitter and the receiver is set at 5 cm. This is limited by the optical power of the µLED and the small area of the PD.

The dynamic range of the µLED is limited in terms of a minimum and a maximum signal level. Hence, clipping of the signal on both sides of the time-domain distribution is practically unavoidable. In this work, exhaustive experiments have determined the best clipping levels at -3.2σ and 3.2σ, where σ is the standard deviation of the time-domain signal. The optimal biasing point is at 5.2 V (I_{bias} = 40 mA). The peak-to-peak voltage swing of the modulating signal is at Vpp = 2.5 V in order to use the full dynamic range of the µLED. The sampling frequency of the AWG is fixed at Fs = 1.25 Gs/s, which results in a maximum achievable single-sided BW = 625 MHz.

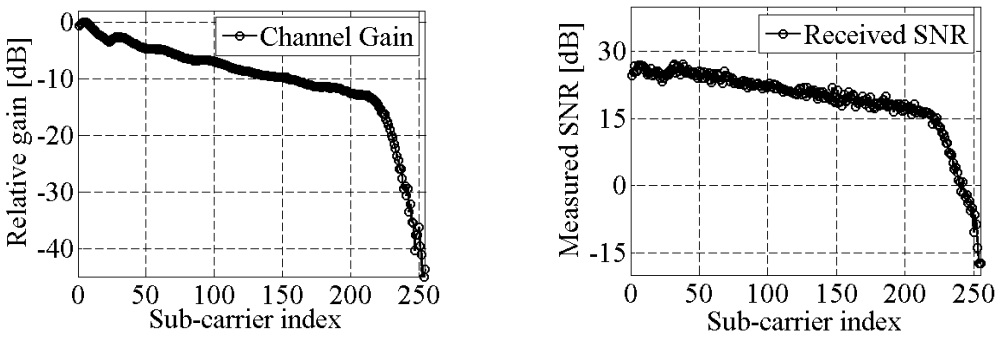

(a) (b)

Figure 35. Estimated: (a) channel gain and (b) SNR

Channel estimation using a pilot sequence that is composed of random binary phase shift keying symbols with constant energy. The relative channel gain and the SNR values, obtained through error vector magnitude estimation, are shown in Figure 35 for the different frequency subcarriers. The channel attenuation follows closely the frequency profile of the μLED whose 3-dB attenuation occurs at a frequency of 60 MHz. The remaining elements in the system have a flat BW up to a frequency of at least 500 MHz. This assumption is supported by Figure 35 (a) where the gain factor experiences a sudden drop after carrier 220 which corresponds to a frequency of approximately 540 MHz.

The estimated SNR profile of the communication channel follows closely the estimated frequency profile. This suggests that the additive white Gaussian noise (AWGN) distribution in the system is uniform within the communication bandwidth.

6.2.2 Communication performance

In this work, two approaches are employed for maximizing the data rate. In the first approach, a fixed rate *M*-QAM scheme is used on all modulated subcarriers. Power pre-equalisation is used in an attempt to equalise the achievable SNR values on each subcarrier at the receiver. In the second approach, both the constellation size and the energy on each subcarrier are decided based on the achievable SNR at that particular frequency. It is expected that the second approach will exhibit better results as it provides more freedom in the signal optimisation procedure.

The first DCO-OFDM implementation is based on pre-equalisation. The pre-equalisation is achieved by applying the inverse function of the system frequency response on all subcarriers before transmission. This effectively scales the energy in each frequency band with the inverse of the system gain. Hence, after propagating to the receiver, all subcarriers should exhibit the same average energy level. The power spectral densities (PSD) of the received signal for the case without pre-equalisation and for the case with pre-equalisation are shown in Figure 36.

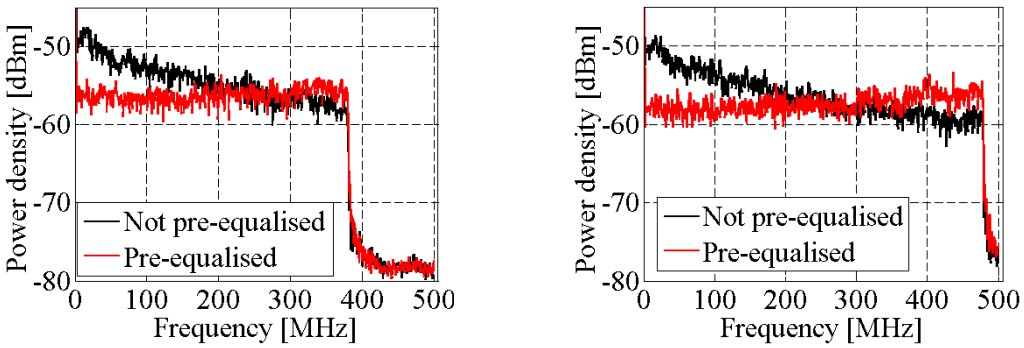

Figure 36. Power-spectrum of 64QAM DCO-OFDM with the last (a) 100 and (b) 60 sub-carriers unused

This shows pre-equalisation leads to a uniform SNR distribution on all subcarriers. In these experiments, the highest data-rate using this approach can be achieved for a constellation size of M = 64.

Figure 36 (a) illustrates the signal PSD when the last 100 subcarriers are not used and the signal BW is approximately 380 MHz. Figure 36 (b) illustrates the case when the last 60 subcarriers are omitted, and the signal bandwidth is approximately 480 MHz. The case in Fig. 3(a) achieves higher SNR values and so a lower BER because the signal energy is distributed over a smaller frequency range. The system throughput, however, is also lower than in the case presented in Figure 36 (b) where the data-rate reaches a value of 2.8 Gb/s for a BER < 0.002. The addition of a forward error correction (FEC) code with an overhead of about 7% can guarantee an error-free transmission in practice. Due to the overhead, the throughput decreases to 2.63 Gb/s.

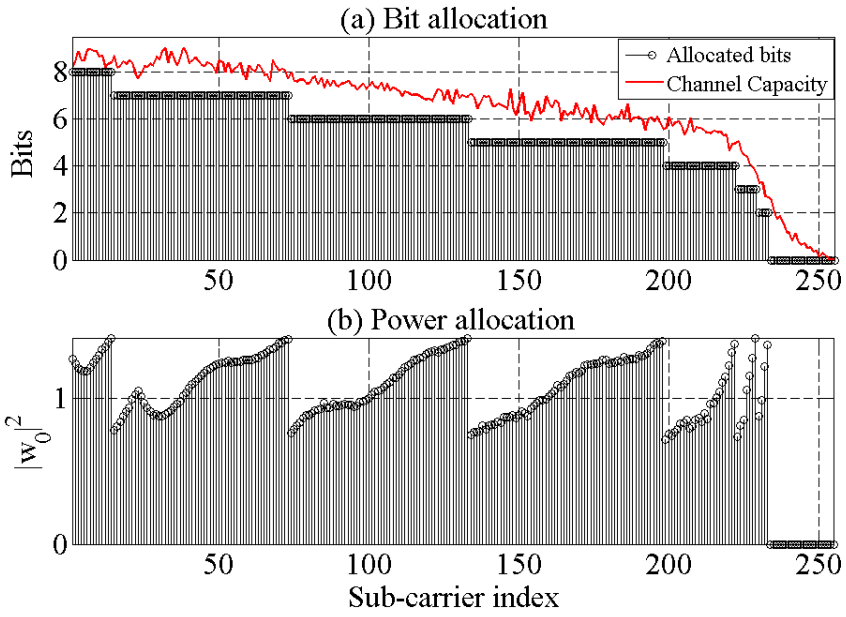

Figure 37. Allocated (a) bits and (b) power

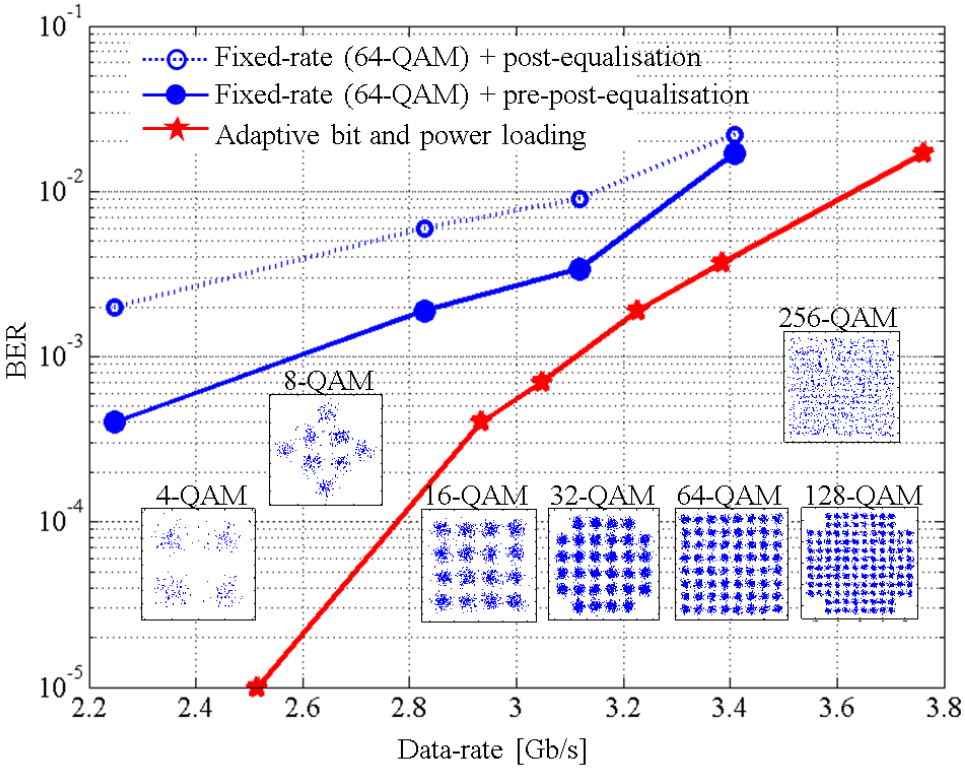

Figure 38. BER results and received constellations for 3.22 Gb/s with adaptive bit and power loading

DCO-OFDM can be optimally used by applying a channel adaptive loading algorithm. In this case, the modified Levin algorithm introduced in Chapter 4 is used. The optimal bit allocation can be seen in Figure 37 (a). The theoretical system capacity for the achieved SNR values on the different subcarriers is also shown. Figure 37 (b) shows the allocated energy on each subcarrier. The algorithm aims to ensure a constant SNR on all received subcarriers with the same constellation size. This optimised modulation signal achieves 3.22 Gb/s with a BER < 0.002. With the 7% overhead for FEC, the data-rate becomes 3 Gb/s. These results are summarised in Figure 38, and the received *M*-QAM constellations are also shown.

6.3 A 1.68 GIGABIT/S WHITE-LIGHT VLC LINK USING A GALLIUM NITRIDE μLED AND PLOYMER BASED COLOUR CONVERTER

In this section, we investigate the feasibility of using a conjugated polymer colour converter to overcome the limitations of existing phosphors. Conjugated polymers are an important class of organic semiconductors that have high fluorescence quantum yields, short (~1 ns) radiative lifetimes and they are simple to process from solutions. Another advantage of using polymers is that they can be blended to obtain a higher quality white-light than the conventional blue LED chip with a phosphor. These properties make them attractive alternatives to current phosphors.

Here, a scheme is proposed to create white-light suitable for both illumination and high-speed VLC, by using the blue electro-luminescence (EL) of a GaN μLED and the yellow photo-luminescence (PL) of a conjugated copolymer of poly para-phenylene vinylene, “Super Yellow” (S-Y; PDY132, Merck KGaA). The μLED with conjugated polymer design can not only generate white-light but also provide higher modulation BW than that of the blue chip and phosphor based commercial WLEDs.

6.3.1 White-light generation

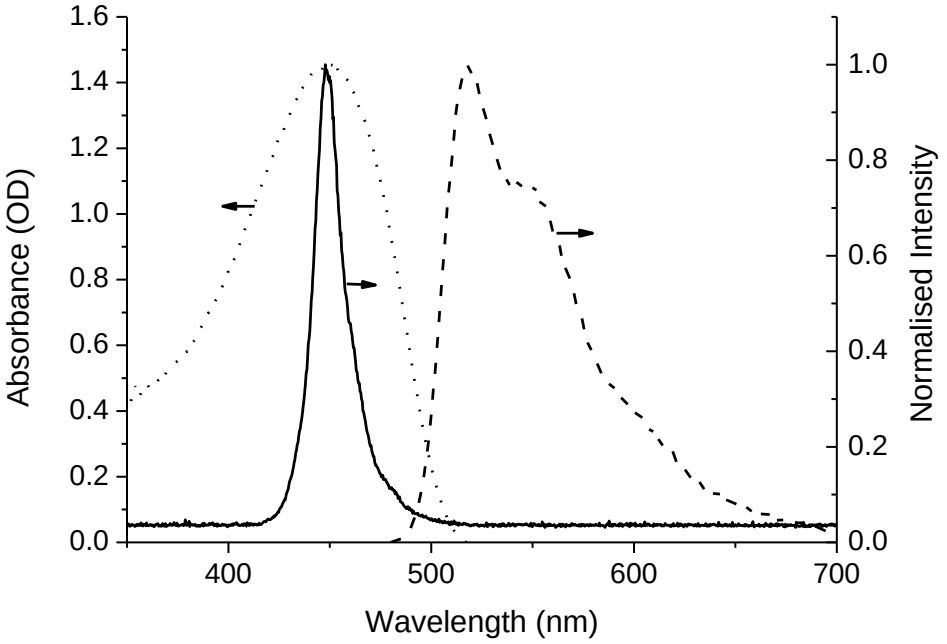

Figure 39. EL spectrum of a GaN μLED (solid line). PL (dashed line) and absorption (dotted line) spectrum of S-Y.

Figure 39 shows the EL emission spectrum of the GaN μLED and the PL emission and absorption spectrum of the S-Y. The S-Y material was supplied by St Andrews University, a UP-VLC project partner. The GaN μLED used in this work has a diameter of 50 μm, Electrical-Optical-Electrical (EOE) B/W of 60 MHz and total radiant flux of 3.5 mW at 60 mA. Higher driving current can increase the B/W, but this value was selected to allow operation in the linear region of its response.

S-Y has a photoluminescence quantum yield (PLQY) of 60%. The measured BW of S-Y in solution is > 200MHz, which can provide a ~50 times higher B/W than a typical phosphor based colour-converter, due to the short fluorescence lifetime (100s of ps) of the material.

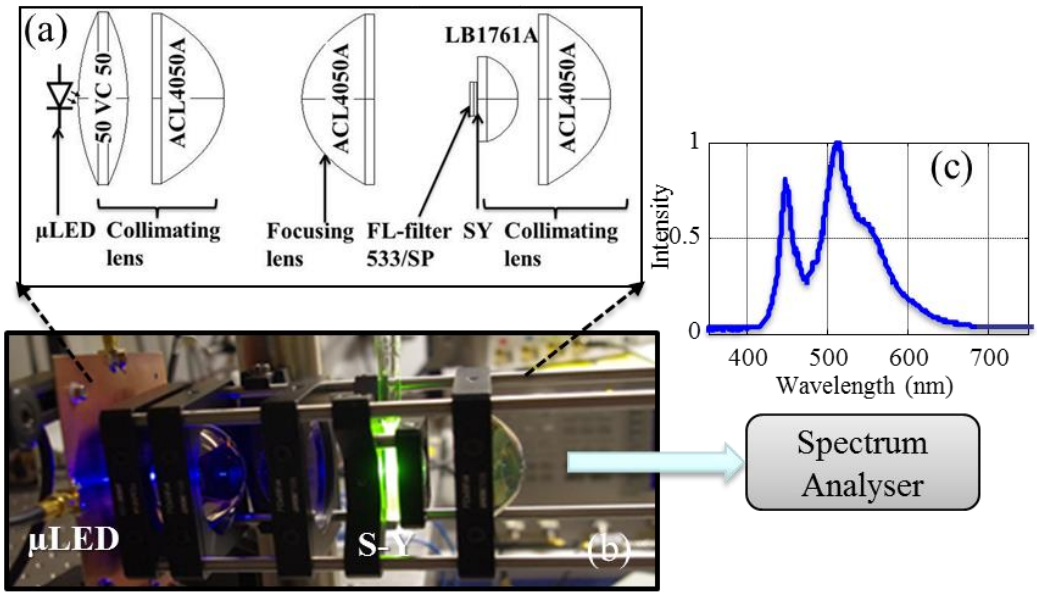

Figure 40. Experimental set-up for white-light generation a) block diagram of the set-up, b) picture of the set-up and c) measured emission spectrum for GaN µLED illuminating a S-Y sample of optical density 0.96.

Figure 40 shows the experimental set up used to generate white-light. Blue light from the GaN µLED was collimated and focused onto the S-Y colour-converter via a series of high numerical aperture (NA) lenses as detailed in the figure. The high NA optics design was used because of the

limited optical power from the µLED and its Lambertian emission profile (half divergence angle of 60°).

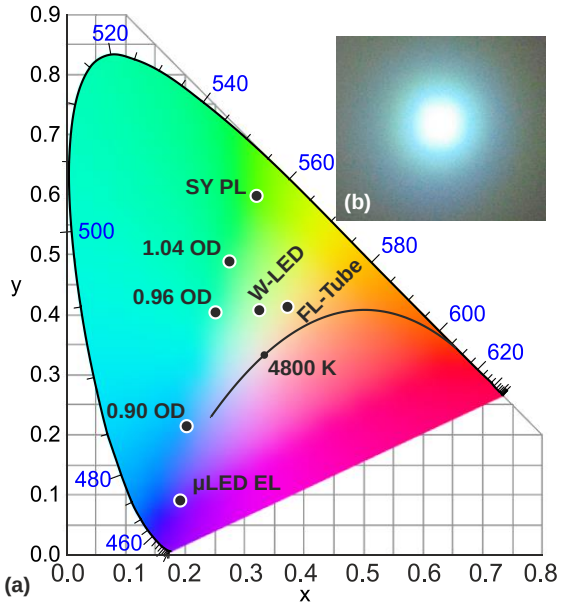

Figure 41. (a) Representation of measured colours on the CIE chromaticity diagram. For comparison, the colours of a commercial WLED, and a fluorescent light tube together with the black body locus (solid line) are presented. (b) Photograph of the projected light of 0.96 OD solution.

The S-Y colour-converter is composed of a 2 mm path length cuvette containing a solution of S-Y in chlorobenzene. This forms a Lambertian emitter and the mixture of emitted yellow and transmitted blue that is emitted from the cuvette holding the S-Y material is highly divergent. Another high NA optical system is used to collect and collimate this emission. To increase the emission efficiency in the forward direction a dichroic mirror, transparent for blue but reflecting

yellow light, is placed just before the S-Y converter. This reflects part of the backward propagating yellow light into the forward direction, increasing the efficiency by approximately 20%.

The composition of the white-light generated in this process can be altered by changing the concentration of the S-Y solution, which controls both the transmittance of the LED light and the intensity of yellow emission. It was found experimentally that the S-Y follows the Beer-Lambert law and the optical density (OD) is proportional to concentration of the solution: OD=5.2*c*, where *c* is the concentration in mg/ml.

Figure 41 (a) shows a CIE plot of the colour generated as the OD is varied. Experiments verified that an OD of 0.96 creates light with the smallest distance from the reference white point (0.33, 0.33). This results in a cool white-light as can be seen in Figure 41 (b). For comparison, the coordinates of a commercial WLED and a fluorescent light tube were also measured, and are also shown in the figure.

6.3.2 Communication performance

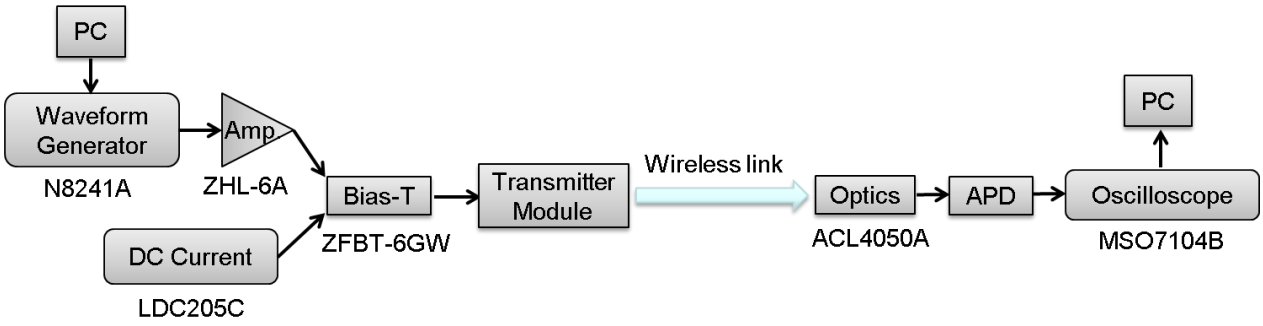

Figure 42. Experimental set up for data communication

DCO-OFDM is used to transmit data as used in the section 5.2. Figure 42 shows experimental set-up for the data communication. The transmitter module is described in Figure 40. The modulated white-light generated from the module is focused onto APD based receiver, through a collecting lens. Two link distances (3 cm and 2 m) were tested, in order to investigate potential of this approach in terms of data-rate and link distance. A small area (0.8 mm^2) and 900 MHz BW APD for the 3cm link and a large area (3 mm^2) and 200 MHz BW APD with higher sensitivity for the 2 m link were used. The output signal is captured by a digital oscilloscope, Agilent MSO7104B. Finally, signal processing for recovery is executed in MATLAB® after synchronization.

The optimal biasing point was determined to be at 60 mA and the peak-to-peak AC voltage swing is set at Vpp = 3.5 V, for full modulation depth. An FFT size of 256 and a cyclic prefix length of 3 were selected as there was no significant improvement for a greater CP (the CP overhead was ~ 1.2%). The applied FFT sampling rate is 1250-Ms/s and 625 Ms/s, which results in a maximum achievable single-sided B/W of 625 MHz and 312.5 MHz, for the 3 cm and the 2 m link, respectively. A bit and power loading scheme was applied. Figure 43 shows the allocated bits and power on each subcarrier. Figure 44 summarises the measured BER results from the two link distances. As shown in the 3 cm link results, ±2.5σ clipping was found to be the optimum for the system we used. The BER curve using ± 3.0σ clipping follows that of the optimum one with a slightly higher BER. Using the optimum clipping level, a data-rate of 1.81 Gb/s was achieved with a BER of 1.2×10^{-3}. Considering a FEC overhead of 7%, the data-rate becomes 1.682 Gb/s. For the 2 m link, 904 Mb/s at a BER of 1.2×10^{-3} was achieved, and this becomes 840 Mb/s after taking account of the FEC overhead.

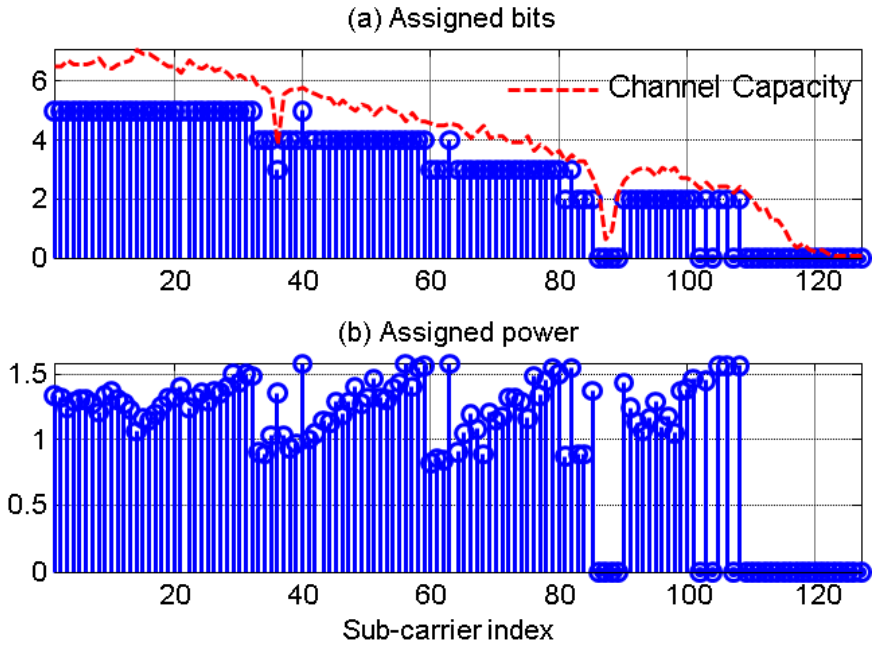

Figure 43. (a) bit and (b) power loading scheme for 1.8 Gb/s with 240 lx (3cm link) using OD 0.96 colour converter

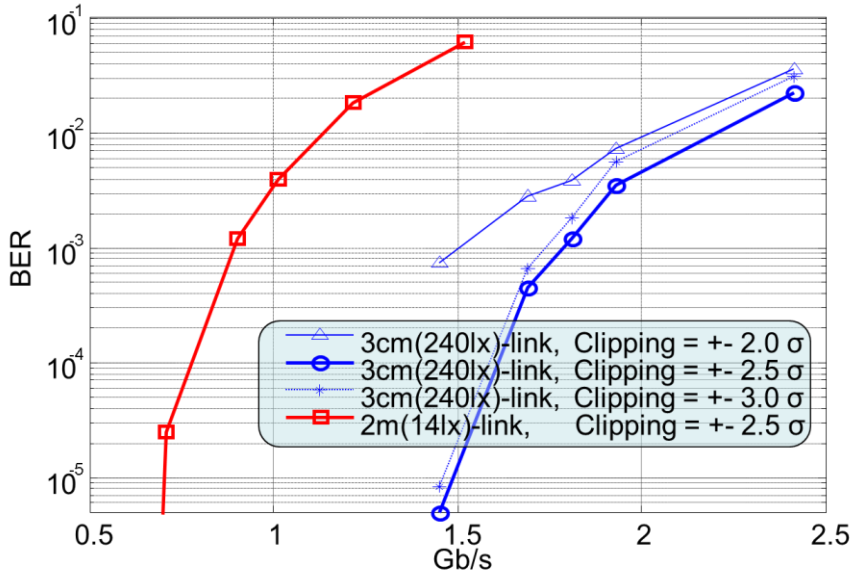

Figure 44. BER results of 3cm and 2m link-distances.

Table 15. Data-rate comparison on the same illumination level

Available Illumination level	**Data-rate in** [60]	**Data-rate in** [74]	**Data-rate in the current work**
14 lx	-	~650 Mb/s	840 Mb/s
240 lx	~300 Mb/s	~950 Mb/s	1682 Mb/s

Table 15 shows that at an illumination level of 240 lx, the 'fast-white' LED described here can provide significant additional capacity. These are the fastest results so far reported for a single white LED source based VLC.

6.4 A 6.52 GIGABIT/S SISO AND 10 GIGA-BIT/S MIMO VLC LINK USING A LASER DIODE BASED REMOTE PHOSPHOR TECHNIQUE

As seen in the previous sections, increasing the BW of the source and generating white-light whilst supporting high-data transmission are key challenges. The combination of a blue laser diode (LD) and a phosphor plate is examined in this section. Despite the low BW of the commercial phosphor plate, it is seen here that the high BW of the LD allows considerable improvement in data-rate.

In the next sub-section, the characteristics of white-light generated by this approach are examined. Parameter optimisation and demonstration of high data-rate VLC using the white-light generated is detailed in the following section.

6.4.1 Laser diode based remote phosphor lighting

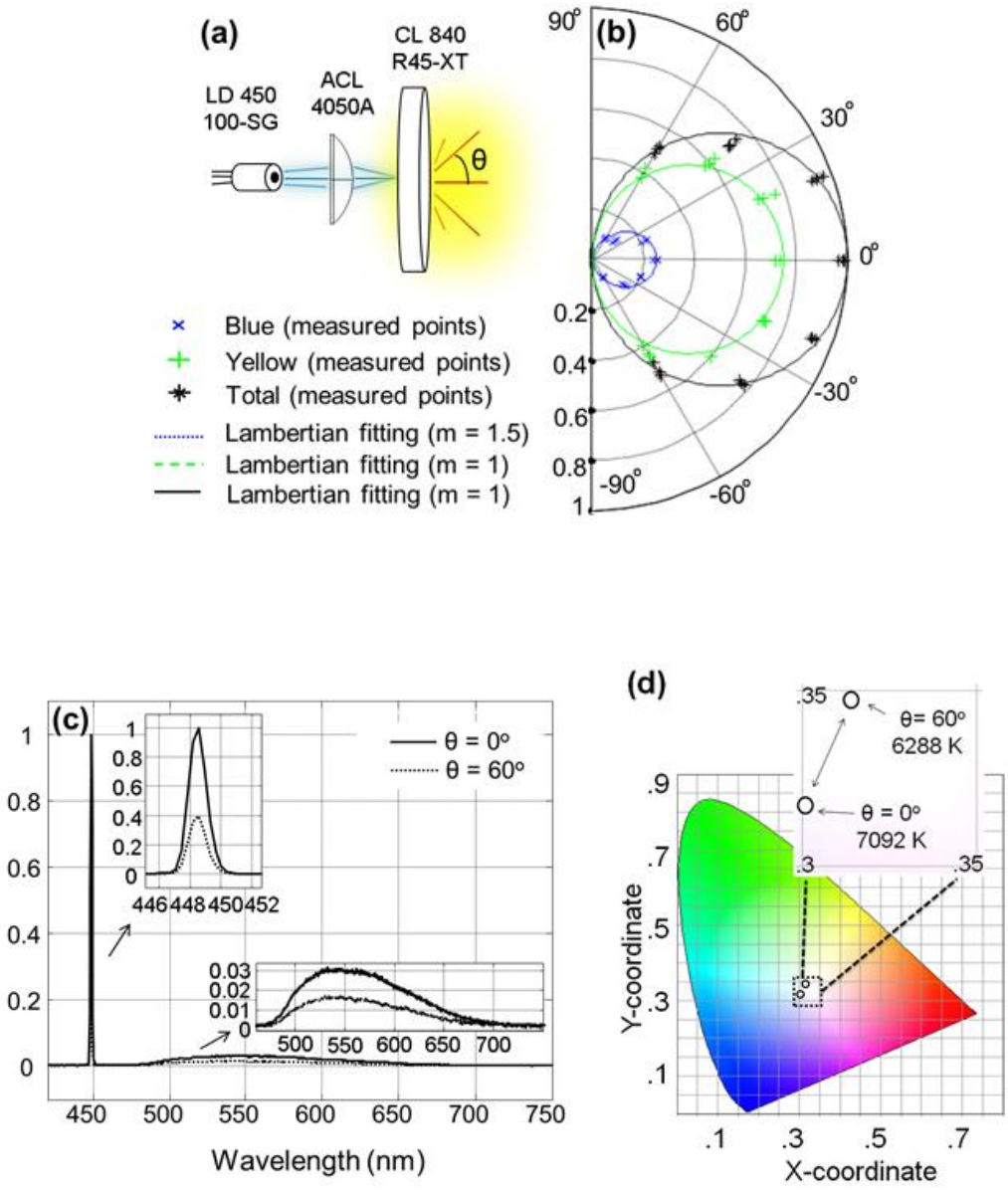

Figure 45. Lighting properties of the blue LD base remote phosphor approach: (a) schematic, (b) emission profile, (c) optical spectrum, and (d) CIE colour coordinate.

Remote phosphor approaches typically use a phosphor plate some distance from the source, and this can improve the efficiency and reliability of the emitter by reducing deleterious thermal effects on the phosphor, compared with typical phosphor coated WLEDs. Another benefit of this remote phosphor approach is that it provides room to optimise the source module as shown in [75] where a very high efficiency of 162.3 lm/W was achieved.

There has been little work on using LD based lighting, although some suggests that the overall system cost may be lower than LED based approaches in the future [76]. There are also few studies on human perception of such sources [77]. LD eye safety also requires investigation, although the diffusing effect of the phosphor plate and the highly divergent source should allow a safe source to be created [78].

Figure 45-(a) shows a schematic of a remote phosphor lighting source based on a blue LD. Blue light from the LD is focused on the phosphor plate through an aspheric lens. This is to create a quasi-point source. The optical spectrum of converted light is measured by a spectrometer (SD2000) while mechanically varying the measurement angle and maintaining the distance from the point source. Then, the properties of each colour component are analysed. Figure 45-(b) shows the measured emission profile, together with a Lambertian fit to the data. The Lambertian pattern shows a normalised intensity profile of $\cos^m(\theta)$ with the highest intensity at normal direction (θ = 0^o). The converted yellow light shows an almost perfect Lambertian profile (m=1). The blue component from the LD shows a Lambertian profile with order of m = 1.5, resulting in a half intensity half angle of ~ 50^o. The phosphor plate therefore not only converts colour, but also scatters the residual blue component. Figure 45-(c) shows the measured optical spectrum. Despite a sharp peak observed at 448.5 nm, the total power (obtained by integration) in blue wavelengths

was less than half of that in the converted broad wavelengths. As the measurement angle θ tends to 60^{o}, the proportion of the blue EL component reduces. This leads to a small change in colour temperature, as indicated in the CIE colour coordinate shown in Figure 45-(d).

6.4.2 Communication performance

DCO-OFDM is applied to test the communication performance. As shown in previous sections, it is important to optimise the signal (such as clipping-level and cyclic-prefix optimisation) beforehand. The optimum condition was obtained by a series of experiments, and then the maximum data-rate was determined, using both a fixed-rate quadrature amplitude modulation (QAM) and a rate adaptive scheme based on the estimated channel information.

Figure 46-(a) shows the experimental set up for single channel VLC using the blue LD based remote phosphor lighting system. First, a PC generates unclipped DCO-OFDM sequences using a 512 IFFT, followed by pulse shaping if needed. In this work, a root raised cosine filter with roll off factor of 0.1 and oversampling factor of 2 is applied. The shaped sequences are further constrained by clipping the upper and lower part. Then, the clipped signal is converted into an analogue signal by an arbitrary waveform generator (Agillent 81180B) with sampling rate set to 4.5 GHz. The analogue signal (7.8Vpp @50Ω load), in addition to a DC current (100mA) supplied by a current source (LDC205C), is applied to a blue LD (LD450 100-SG) via a bias-T (ZFBT-6GW). This peak to peak voltage value was selected as it provides almost full modulation depth and linear response. The blue EL light is focused through an aspheric lens and is incident on a phosphor plate (CL840 R45-XT), creating a white emission. The light is collimated by another aspheric lens (ACL4050A). The distance between the lens and the plate is first adjusted to provide 100 lx at a

1m range. Higher lux levels are easily achievable by decreasing the range (i.e., 400 lx @40 cm, 1000 lx @15 cm).

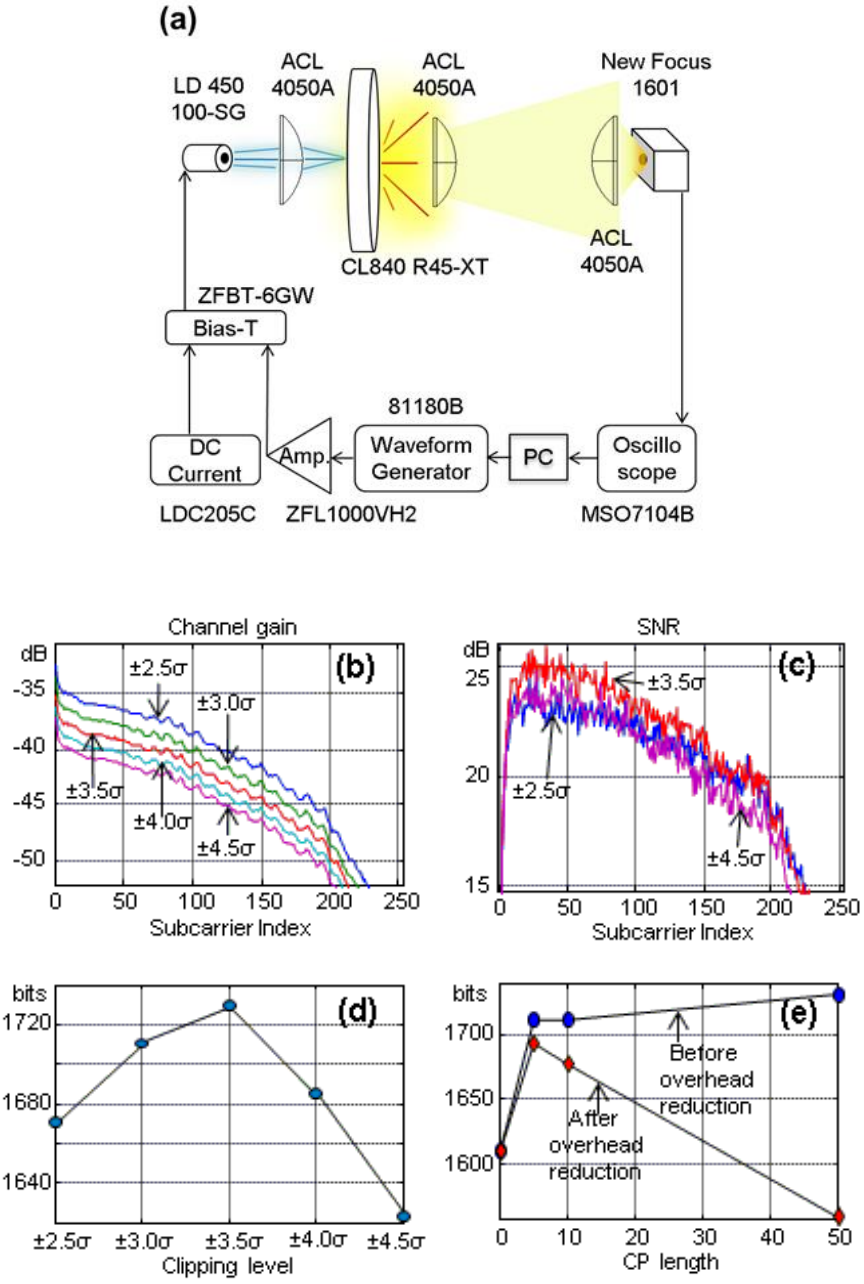

Figure 46. (a) Experimental set up, (b) channel gain and (c) SNR by varying the clipping level, (d) clipping level optimization by calculated capacity, and (e) cyclic prefix optimization

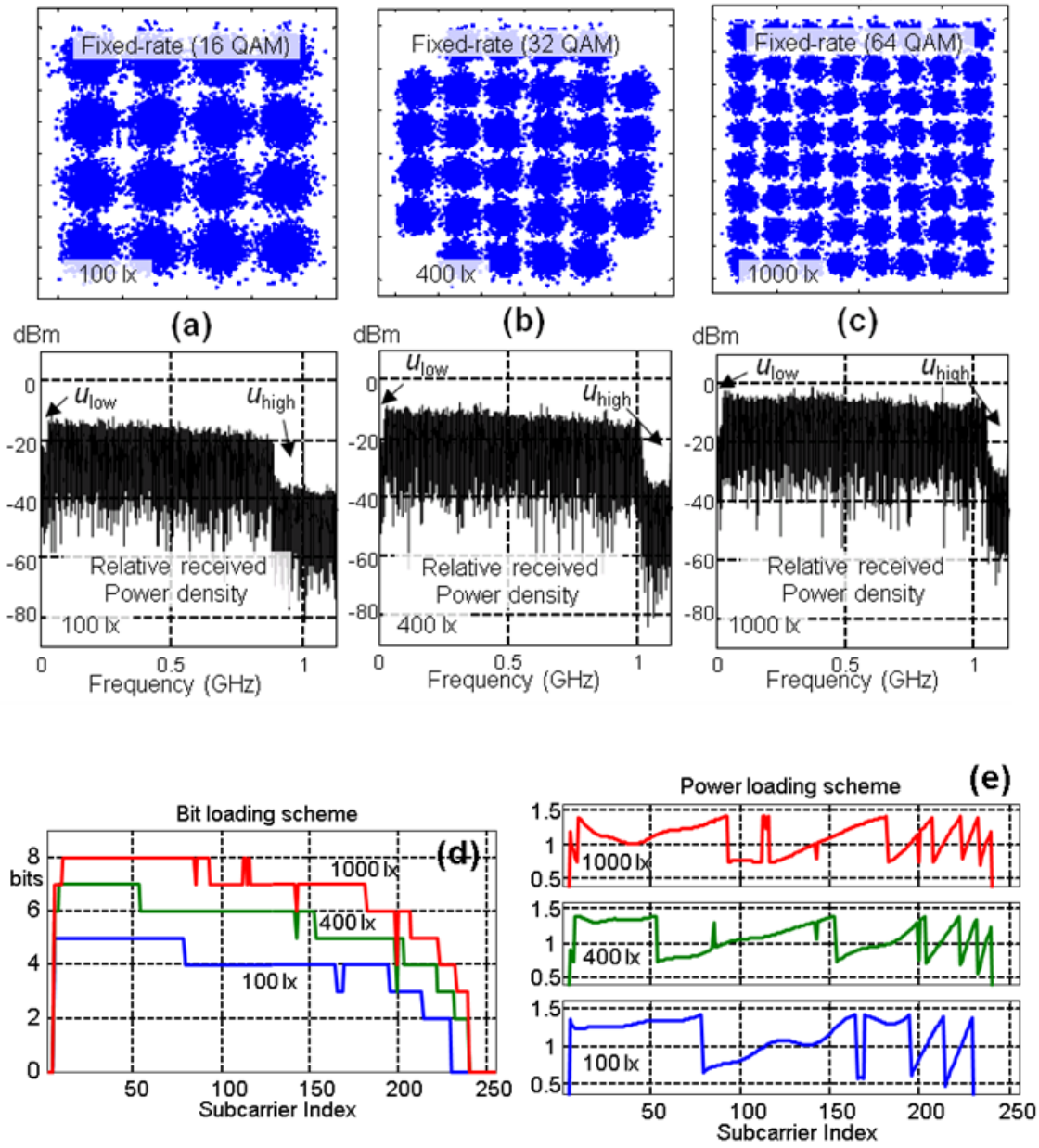

Figure 47. Received constellation and relative power spectral density of the fixed-rate approach at illumination levels of (a) 100 lx, (b) 400 lx, and (c) 1000 lx applied (d) bit loading and (e) power loading scheme for the three lux levels

The collimated light is focused onto a high-speed photo detector (New Focus 1601) using a further lens. An oscilloscope (MSO7104B) captures the electrical signal from the detector and sends it back to the PC for demodulation.

Figure 46-(b) shows the measured channel gain at 400 lx for different clipping levels. Generally, in DCO-OFDM, clipping is applied symmetrically and is expressed relative to the unclipped signal's standard deviation. In the figure, it can be seen that increasing clipping also increases the channel gain. This is mostly because the power in the unclipped signal for the given transmitter's dynamic range is inversely proportional to the clipping level. For this reason, compared to the channel gain for clipping of ±4.5σ, that of ±2.5σ is higher by ~5dB (= $20\log_{10}(4.5/2.5)$). Figure 46-(c) shows the *SNR*, incorporating the effect from the additive noise and the clipping noise. A ±3.5σ clipping level presented the best *SNR* throughout all subcarriers. Figure 46-(d) shows the capacity vs the measured *SNR*, and clearly shows that ±3.5σ offers the maximum capacity. Figure 46-(e) shows the CP optimisation. This time the clipping level was fixed to the optimum value (±3.5σ). It can be seen that after a length of 5 the capacity shows a slight increase, but considering the capacity reduction due to the CP overhead, a length of 5 is optimal.

The communication performance was measured at illumination levels of 100 lx, 400 lx, and 1000 lx . The optimal clipping level is found to be ±2.5σ and ±4.5σ at 100 lx and 1000 lx, respectively. The first 5 subcarriers (up to 22.1 MHz) were not used to avoid impairments caused by the wide band amplifier, which has a low frequency cut off of 20 MHz. Then, by changing the number of subcarriers used and QAM level, the highest data-rates with bit error rate (BER) < 2x10-3 were determined. Figure 47-(a), (b), and (c) show the constellations and received power

spectral density at 100 lx, 400 lx, and 1000lx, respectively. The measured data-rates were 3.42 Gb/s, 4.89 Gb/S, and 6.05 Gb/s, respectively.

Next, a channel adaptive bit and power loading technique was applied. Figure 47-(d) and (e) show the optimised bit loading and power loading schemes at illumination levels of 100 lx, 400 lx, and 1000 lx. Data rates of 4 Gb/s, 5.67 Gb/s, and 7.01 Gb/s were achieved, respectively.

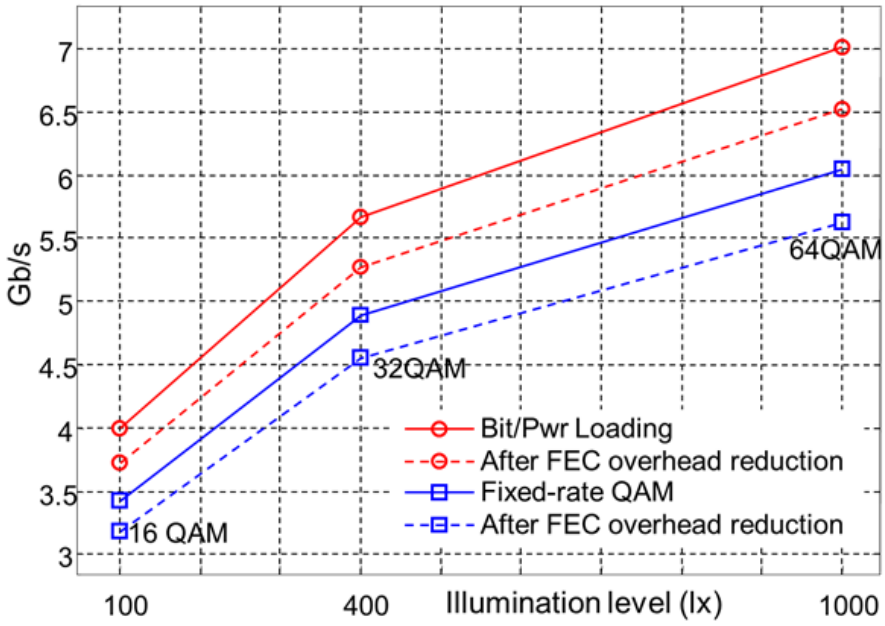

Figure 48. Data-rates for different illumination levels using fixed-rate and adaptive loading approaches

Figure 48 summarises the results of both fixed-rate and adaptive loading approaches, before and after 7 % of FEC overhead reduction. Overall, adaptive loading showed better results than the fixed-rate approach. Compared to previous results using a blue LED plus phosphor coating (1 Gb/s) and an RGB WDM approach (3 Gb/s), this blue LD based remote phosphor technique allowed

6.52 Gb/s @ 1000 lx after overhead reduction. Using the simple fixed-rate method it was still possible to achieve a data-rate of 5.62 Gb/s after overhead reduction.

The potential of using an imaging receiver for spatial-multiplexing was also investigated. It is essential to explore the spatial dimension because i) a proper room illumination level, between 400 lx and 1000 lx, creates a communication system in a BW limited regime of channel capacity, where the capacity increases logarithmically by increasing SNR, and ii) there is significant difficulty in increasing the overall BW mainly due to the limited availability of high BW optical and electronic devices. Here, the performance of a two channel imaging system using the blue LD based remote phosphor technique is investigated.

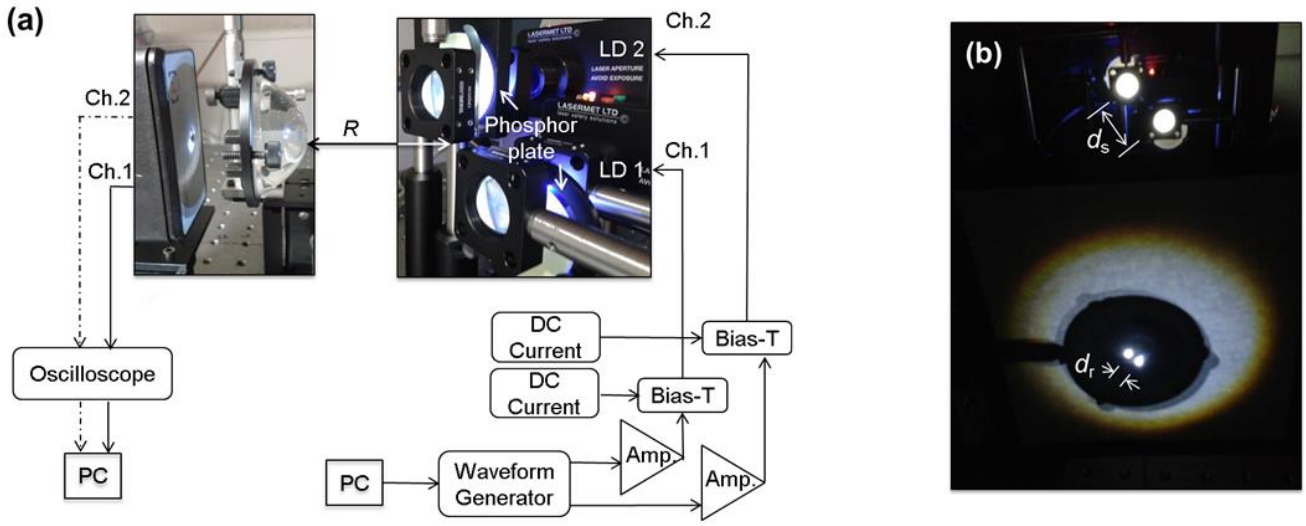

Figure 49. (a) Experimental set up for two channel imaging system and (b) picture showing sources and images for this system

Figure 49-(a) shows the experimental set up for the two channel imaging system. The transmitter system is identical to the system described in the single channel case, except that two LDs were modulated using two independent data streams. At a link distance of 35 cm, two optical beams overlap sufficiently to provide almost equal power to the receiver module. At this distance, a total illumination level of 500 lx was measured. Then, using an aspheric concentrator lens with a diameter of 5.5 cm and f-number of 1, two distinct images of sources are formed. The main advantage of such a imaging system is that it can de-correlate a combination of highly directional light sources, and Figure 49-(b) shows this.

By placing the PD at these image points, it was feasible to capture the individual channel and process independently. Note that only the data from each single channel was captured at one time as a large commercial detector module did not allow placing two photo detector units at the imaging points. However, we verified the validity of this approach by measuring the channel matrix, and there was no optical cross-talk.

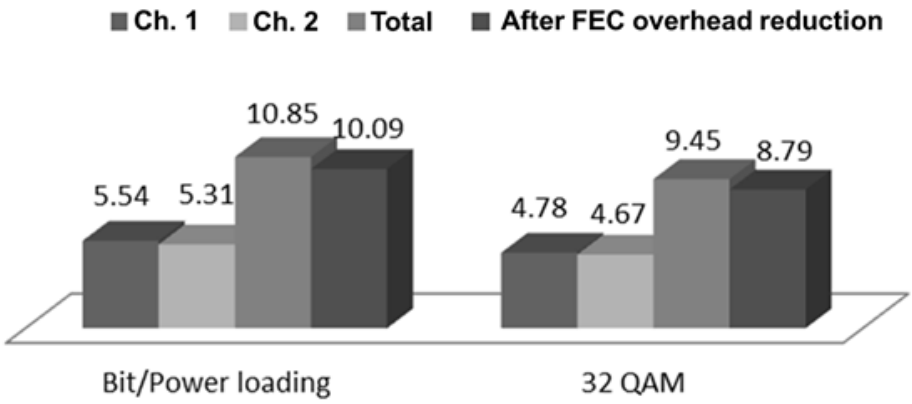

Figure 50. Data-rates for two channel imaging system

Figure 50 summarises the achieved data-rates for a BER of $< 2 \times 10^{-3}$. As before, fixed-rate with pre-equalisation and channel adaptive bit and power loading were investigated. Parameter optimisation was undertaken for each channel, following the same procedure as detailed earlier in this section. Both channels presented similar performance (< 5% difference), and the adaptive loading approach offered higher data-rates than the fixed-rate case. The total data-rate after FEC overhead reduction was 10.09 Gb/s and 8.79 Gb/s for the two approaches, respectively. These results demonstrate the considerable potential for the high-speed VLC using a blue LD based remote phosphor lighting technique combined with spatial multiplexing.

6.5 CONCLUSIONS

In this chapter, three high-speed VLC demonstrations were introduced. First, the feasibility of a 3-Gb/s wireless link with a single Gallium Nitride μLED was investigated. Also, the feasibility of using a conjugated polymer for white-light VLC was investigated. Here, white-light (for illumination) with a high modulation BW (for Gb/s communication) was generated. A 1.68 Gb/s white-light communication link was demonstrated at 3-cm distance. It was also verified that the scheme can be used in a distance of 2m. Lastly, it was found that LD based remote phosphor white-lighting has considerable potential to provide high data-rate. After optimisation, data-rates of up to 6.52 Gb/s were achieved at 1000 lx. Furthermore, by employing a two-channel imaging system, a total data-rate of 10 Gb/s was found to be achievable.

It was not possible to optimise the source and detector based on the technology curve introduced in the previous chapters due to the limited choice of experimental devices. However, the outcomes of these demonstrations are very promising and show that the multi-Gb/s VLC

systems are feasible. Future work includes improving the coverage area, implementing real-time systems, and investigating the human acceptance associated with the generated light, especially for the laser-based white-light.

Chapter 7
Conclusions and Future work

7.1 CONCLUSIONS

VLC can potentially assist in alleviating the wireless communications spectrum 'drought', thanks to a considerable amount of unlicensed spectrum. For the optimum design of a multi Gigabit VLC system, however, a comprehensive modelling approach is required. The main aim of this thesis is to create a general modelling for multi Gb/s VLC system design. This was achieved by analysing and comparing a number of VLC schemes, techniques, and devices in terms of the SNR and BW requirement (and the availability), given the same practical VLC constraints. Novel design methods, such as optimisation for band-limited O-OFDMs, generalisation of MIMO VLC channels, and technology curve including device characteristics, were newly presented.

The thesis begins with the illumination and communication channel modelling. It was shown that optimisation of lighting for both communications and illumination has substantial benefits. Two lighting designs were studied. The square illumination design has a steep gradient in illumination level (and hence the received optical power) compared with the hollow design. The hollow design having a low STD can relieve the dynamic range requirements of VLC receivers, reducing the complexity. In terms of bandwidth, both designs showed only ~5 dB attenuation to 100 MHz at the worst receiver position. It implicates the overall channel frequency response follows that of LOS, high speed data transmission is still feasible through these worst channels.

A number of VLC schemes and techniques were compared to estimate their required SNR and BW. A technology curve approach that incorporates device parameters was also introduced. From this investigation it was found that for typical devices with device property parameter K-1system of > 3, significant gain in margin can be obtained by using low BW high SNR approaches. When a -60 dB/dec LPF channel with relative BW greater than 0.15 is used, OOK with DFE requires the smallest SNR. When below 0.15, bit/power loaded DCO-OFDM demands the smallest SNR. The effectiveness of MIMO schemes (Ganging, ZF based Smod, and ZF based Smux) can also be incorporated into the analysis. It was shown that depending on the degree of MIMO channel crosstalk, the optimum MIMO scheme is determined.

Two optimised system design examples using this comprehensive modelling were introduced. The first example considered an illumination constraint. A maximum achievable data-rate of 2.9 Gb/s was found by using adaptively loaded DCO-OFDM with a modulation BW of 350 MHz. The second example showed an optimised design of 10 Gb/s 4x4 MIMO VLC module. The largest SNR margin of 5 dB was achieved by using adaptively loaded DCO-OFDM with a modulation BW of 150 MHz. These examples showed how to maximise data-rate (or margin) when illumination level (or target data-rate) is given.

To check the feasibility of the multi Gb/s VLC system by a series of ‘proof-of-concept’ experiments were also conducted. A 3-Gb/s wireless link with a single Gallium Nitride µLED is feasible. The result shown here is the fastest single LED based wireless VLC system demonstration up-to-date. A 1.68 Gb/s white-light communication link can be constructed, using a conjugated polymer for the white-light generation. The data-rate is the fastest result so far reported for a single white LED based VLC. LD based remote phosphor white-lighting has considerable

potential to provide high data-rates. After optimisation, data-rates of up to 6.52 Gb/s were achieved at 1000 lx. Moreover, by employing a two-channel imaging system, a total data-rate of 10 Gb/s was found to be feasible. These demonstrations show the potential of VLC to construct high-speed communication links as well as the generation of white-light suitable for illumination.

From the modelling, numerical analysis, and experimental investigations conducted throughout this thesis, it can be seen that choosing the optimum VLC schemes is crucial, and the characteristics of the devices used must be taken into account. There is considerable potential for further optimisation of data transmission using custom designed transmitters and receivers. The new generalized modelling method incorporating these important aspects enables the optimum design of multi Gb/s VLC systems.

7.2 FUTURE WORK

Future work should focus on including VLC schemes not examined in this thesis since it will allow more options for the optimum design of multi Gb/s VLC systems. In addition, the overall signal energy consumption might be modelled in an optimisation process in conjunction with commercialisation.

7.2.1 Further investigations in VLC schemes

Investigations in VLC schemes should be done mainly in two aspects: 1) research on variations of O-OFDM schemes and 2) further generalisation of MIMO schemes. Variations of O-OFDM schemes, such as ADO-OFDM shown in [45], introduced in the recent two years or so should be studied. Some claim that the new OFDM schemes they introduced are both power and spectrally

efficient, but there have not been any experimental verification. Their performances have to be investigated not only by modelling but also by experiments, given practical VLC constraints.

In this thesis, only 4 x 4 MIMO was examined. For a better generalisation, the impact of adding more MIMO channels, deviating from the centre alignment, and applying different pitch sizes have to be investigated. Also, incorporating imaging MIMO schemes and a more general analysis between imaging and non-imaging, using the MIMO crosstalk coefficient introduced in this thesis, Kcorr, is an area worthy of investigation.

7.2.2 Energy consumption and commercialisation

It was shown that constructing a multi Gb/s VLC system is feasible. One of the most significant barriers for the commercialisation of this system could be the cost. Generally, the cost means the installation and the operating cost. As discussed in the introduction, since VLC can reuse the existing lighting infrastructure, the installation cost can be smaller than the other candidates supporting multi-Gb/s links, such as IR or RF (mm-wave) based systems.

The operating cost is closely related to the energy consumption of the system. Investigation of the energy consumption of a number of VLC schemes or sets should be investigated. Then, the overall signal energy consumption can be modelled in the communication performance optimisation process in this thesis. The performance-energy optimised Gb/s class VLC system can then be compared with the other candidates. When the VLC's operating cost turns out to be smaller than the other candidates, there can be more opportunities for VLC in the market.

Appendix 1
SNR requirement for L-QAM O-OFDM

(A) Useful signal power over total noise power

$$\mathrm{SNR}_{\mathrm{O-OFDM}} = \frac{\frac{\mathrm{K}^2}{\mathrm{G}}\left(\frac{\sigma_{\mathrm{x}}}{\mathrm{P}_{\mathrm{optical}}}\right)^2 (\mathrm{RP}_{\mathrm{optical}})^2}{\left(\frac{\sigma_{\mathrm{cl}}}{\mathrm{P}_{\mathrm{optical}}}\right)^2 (\mathrm{RP}_{\mathrm{optical}})^2 + \mathrm{i}^2_{\mathrm{comm}}} \quad (A1)$$

$$\therefore\ \mathrm{SNR}_{\mathrm{O-OFDM}} = \frac{\frac{\mathrm{K}^2}{\mathrm{G}}\left(\frac{\sigma_{\mathrm{x}}}{\mathrm{P}_{\mathrm{optical}}}\right)^2}{\left(\frac{\sigma_{\mathrm{cl}}}{\mathrm{P}_{\mathrm{optical}}}\right)^2 + \frac{\mathrm{i}^2_{\mathrm{comm}}}{(\mathrm{RP}_{\mathrm{optical}})^2}} \quad (A2)$$

$$= \frac{\eta_{\mathrm{O-OFDM}}}{\gamma^{-1}_{\mathrm{clip,O-OFDM}} + \gamma^{-1}_{\mathrm{comm}}}$$

K (Bussgang's coefficient)
$=Q(-Bot/\sigma_x) - Q(DR\text{-}Bias/\sigma_x)$
Bot = 0 (for ACO),
= Bias (for DCO)
Q : Q-function

σ_x^2 : time signal variance σ_{cl}^2 : clipping noise variance
G : spectral gain [47]
= .5(ACO)
≃ 1(DCO)

(B) Required γ_{comm} for L-QAM O-OFDM

$$\mathrm{BER}_{\mathrm{LQAM}} \approx \frac{2\left(\sqrt{\mathrm{L}}-1\right)}{\sqrt{\mathrm{L}}\log_2\sqrt{\mathrm{L}}}\,\mathrm{Q}\left(\sqrt{\frac{3\mathrm{SNR}_{\mathrm{O-OFDM}}}{\mathrm{L}-1}}\right) \quad (A3)$$

From
Eq17. in [50]

$$\mathrm{SNR}_{\mathrm{O-OFDM}} \approx \frac{\mathrm{L}-1}{3}\left[\,\mathrm{Q}^{-1}\left(\frac{\sqrt{\mathrm{L}}\log_2\sqrt{\mathrm{L}}}{2\left(\sqrt{\mathrm{L}}-1\right)}\mathrm{BER}_{\mathrm{LQAM}}\right)\right]^2 \quad (A4)$$

- $Eb/N0 = \gamma = SNR_{ACO} / \log_2 L$
- $\gamma_{comm,req} = \log_2 L\ \gamma_{b\ comm,req}$

$\therefore$ From (A2) and (A4), required SNR(common), $\gamma_{comm,req}$ becomes

$$\gamma_{comm,req} \approx \left(\frac{\frac{K^2}{G}\left(\frac{\sigma_x}{P_{optical}}\right)^2}{\frac{L-1}{3}\left[\, Q^{-1}\left(\frac{\sqrt{L}\log_2\sqrt{L}}{2\left(\sqrt{L}-1\right)} BER_{LQAM}\right)\right]^2} - \left(\frac{\sigma_{cl}}{P_{optical}}\right)^2 \right)^{-1} \qquad \text{(A5)}$$

Appendix 2
Clipping noise in O-OFDM

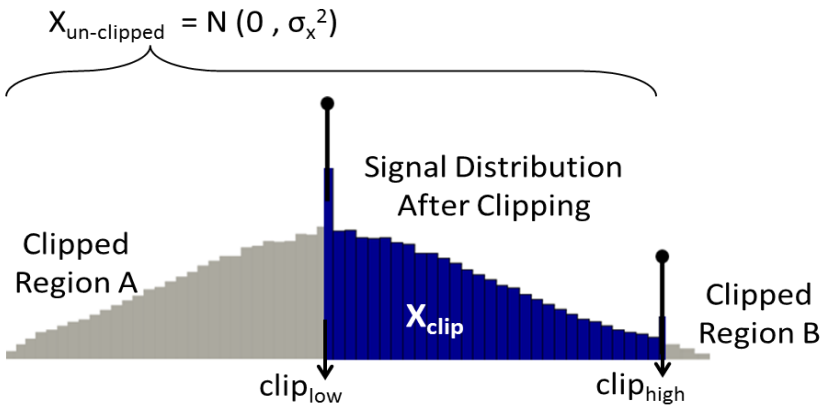

Figure 51. Clipped O-OFDM time-domain signal distribution

(A) DC component generated by clipping, $E[X_{clip}(k)]$

$$E[X_{clip}(k)] = \int_{clip_{low}}^{clip_{high}} x\, pdf(X_{clip})\, dx \qquad (A6)$$

$$= \Phi(hc) - \Phi(lc) + \frac{Bias}{Q(lc) - Q(hc)}$$

$$+ clip_{low}(1 - Q(lc)) + clip_{high} Q(hc)$$

(B) Clipping noise variance, σ_{cl}^2

$$\sigma_{cl}^2 = var[X_{clip}] - K^2\sigma_x^2 \qquad (A7)$$

$$= \int_{clip_{low}}^{clip_{high}} x^2\, pdf(X_{clip})\, dx - E^2[X_{clip}(k)] - K^2\sigma_x^2$$

Φ : normal gaussian pdf

hc

$$= \frac{clip_{high} - Bias}{\sigma_x}$$

lc

$$= \frac{clip_{low} - Bias}{\sigma_x}$$

Bias : applied bias to obtain the desired optical power

[Note]
For ACO-OFDM, clipping

$$= \frac{2\text{Bias}}{Q(lc) - Q(hc)}\left(\Phi(hc) - \Phi(lc) + \frac{\text{Bias}}{Q(lc) - Q(hc)}\right)$$

$$- \frac{\text{Bias}^2}{Q(lc) - Q(hc)} + \sigma_x^2 \left(lc\Phi(lc) - hc\Phi(hc) + \frac{1}{Q(lc) - Q(hc)}\right)$$

$$+ clip_{low}^2\left(1 - Q(lc)\right) + clip_{high}^2 Q(hc) - E^2\left[X_{clip}(k)\right] - K^2\sigma_x^2$$

in region A does not create clipping noise on odd subcarriers. Thus, σ_{cl}^2 for ACO is calculated by setting $clip_{low}$ to $-\infty$.

Appendix 3
Cyclic-prefix overhead in low-pass-filter channels

In a band limited communication channel, inter-symbol-interference occurs. For an OFDM to be free from the inter-symbol-interference, a cyclic-prefix is required. This uses a portion of the OFDM frame and reduces the overall data-rate. For a fair performance comparison of OFDM with respect to OOK in the band limited channel, this has to be included.

Table 16. Relative RMS delay spread of LPF channel with various BWs and slopes

Slope\ BW	**1/2**	**1/4**	**1/8**	**1/16**	**1/32**	**1/64**	**1/128**
10 dB/dec	0.062	0.087	0.147	0.273	0.515	0.959	1.720
20 dB/dec	0.112	0.225	0.450	0.900	1.800	3.601	7.202
30 dB/dec	0.159	0.318	0.636	1.273	2.546	5.092	10.185
40 dB/dec	0.194	0.389	0.779	1.559	3.118	6.237	12.474
50 dB/dec	0.225	0.450	0.900	1.800	3.601	7.202	14.400

Table 16 shows the RMS delay spread relative to one OOK symbol duration $T_{s,OOK}$. For instance, when a signal occupies 8 times the 3-dB BW (relative BW = 1/8) of a low-pass-filter channel with a slope of 30 dB/dec, the relative RMS delay spread ($T_{rel,DS} = T_{DS}/T_{s,OOK}$) is 0.636.

For ISI free operation of OFDM, a cyclic prefix duration (T_{CP}) with 2~4 times the RMS delay spread has to be applied [79]. Then, the ratio between the increased number of required bits to apply a CP (b_{with_CP}) and the required number of bits without CP ($b_{without\_CP}$) for optical OFDMs is calculated as below.

$$\frac{b_{with_{CP}}}{b_{without_{CP}}} = \frac{T_{OFDM} + T_{CP}}{T_{OFDM}} = \frac{T_{OFDM} + 4T_{DS}}{T_{OFDM}}$$

$$= \frac{N_{subcarriers} T_{s,OOK} + 4T_{rel,DS} T_{s,OOK}}{N_{subcarriers} T_{s,OOK}} = \frac{N_{FFT} + 8T_{rel,DS}}{N_{FFT}} \qquad (A3)$$

,where T_{OFDM}, $N_{subcarriers}$, and N_{FFT} denotes OFDM symbol duration, number of sub carriers, and FFT size, respectively. For example, when $T_{rel,DS}$ 0.636 and FFT size is 64, $\frac{b_{with_{CP}}}{b_{without_{CP}}}$ becomes 1.08, meaning that 8 % more bits have to be allocated to achieve the same data-rate as the case without CP overhead.

Publications

❖ Journal

[1] S. Videv, D. Tsonev, **H. Chun**, S. Rajbhandari, J. J. D. McKendry, E. Gu, G. Faulkner, M. D. Dawson, D. O'Brien, H. Haas, "A Gb/s Single-LED Wireless VLC Link Using a Gallium Nitride μLED at a Distance of up to 10m," IEEE Photonics Technology Letters (being reviewed).

[2] S. Rajbhandari, **H. Chun**, G. Faulkner, K. Cameron, A. V. N. Jalajakumari, R. Henderson, D. Tsonev, M. Ijaz, Z. Chen, H.Haas, E. Xie, J. J. D. McKendry, J. Herrnsdorf, E. Gu, M. D. Dawson, D. O'Brien, "High-Speed Integrated Visible Light Communication System: Device Constraints and Design Considerations," IEEE JSAC Special Issue on Optical Wireless Communications, 2015.

[3] M.T. Sajjad, P.P. Manousiadis, **H. Chun**, D. Amarasinghe, S. Rajbhandari, A.L. Kanibolotsky, G. Faulkner, D. O'Brien, P.J. Skabara, I.D.W. Samuel, and G.A. Turnbull, "Novel Fast Color-Converter for Visible Light Communication Using a Blend of Conjugated Polymers ", ACS photonics, 2015.

[4] M. T. Sajjad, P. P. Manousiadis, C. Orofino, D. Cortizo-Lacalle, A. L. Kanibolotsky, S. Rajbhandari, D. Amarasinghe, **H. Chun**, G. Faulkner, D. C.O'Brien, P. J. Skabara, G. A. Turnbull and I. D. W. Samuel "Fluorescent red-emitting BODIPY oligofluorene stars as a novel color converter material for visible light communications" , Journal Advanced Optical Materials, 2014.

[5] **H. Chun**, P. Manousiadis, S. Rajbhandari, D. A. Vithanage, G. Faulkner, D. Tsonev, J. J.D. McKendry, S. Videv, E. Xie, E. Gu, M. D. Dawson, H. Haas, G. A. Turnbull, I. D.W. Samuel, D. O'Brien, "Visible Light Communication using a Blue GaN μLED and Fluorescent Polymer Colour Converter", IEEE Photonics Technology Letters, 26(20), 2035-2038, 2014.

[6] Tsonev, D*.; **Chun, H***.; Rajbhandari, S.; McKendry, J.; Videv, S.; Gu, E.; Haji, M.; Watson, S.; Kelly, A.; Faulkner, G.; Dawson, M.; Haas, H.; O'Brien, D., "A 3-Gb/s Single-LED OFDM-based Wireless VLC Link Using a Gallium Nitride μLED," IEEE Photonics Technology Letters, 26(7), 637 – 640, 2014. * First two authors contributed equally to this work, as shown in the acknowledgement.

[7] **Hyunchae Chun**; Chien-Jung Chiang; Monkman, A.; O'Brien, D., "A Study of Illumination and Communication using Organic Light Emitting Diodes," Lightwave Technology, Journal of , vol.31, no.22, pp.3511,3517, Nov.15, 2013.

❖ Conference

[1] P. Manousiadis, **H. Chun** S. Rajbhandari, R. Mulyawan, D. A. Vithanage, G. Faulkner, D. Tsonev, J. J.D.McKendry, M. Ijaz, S. Videv, E.Xie, E. Gu, M.D. Dawson, H. Haas, G. A. Turnbull, I.D.W. Samuel, and D. O'Brien, "Demonstration of 2.3 Gb/s RGB White-light VLC using Polymer based Colour-converters and GaN micro-LEDs," IEEE Summer Topicals Meeting 2015, Visible Light Communications (VisC), Nassau, Bahamas, 2015 (Invited).

[2] S. Rajbhandari, **H. Chun**, G. Faulkner, K. Cameron, A. V. N. Jalajakumari, R. Henderson, D. Tsonev, M. Ijaz, Z. Chen, E. Xie, J. J. D. McKendry, J. Herrnsdorf, E. Gu, M. D. Dawson, H. Haas, and D. O'Brien, "Multi-Gigabit Integrated MIMO Visible Light Communication System: Progress and Updates," IEEE Summer Topicals Meeting 2015, Visible Light Communications (VisC), Nassau, Bahamas, 2015.

[3] D. Chitnis, L. Zhang, **H. Chun**, S. Rajbhandari, G. Faulkner, D. O'Brien, and S. Collins, "A 200 Mb/s VLC demonstration with a SPAD based receiver," IEEE Summer Topicals Meeting 2015, Visible Light Communications (VisC), Nassau, Bahamas, 2015.

[4] S. Collins, R. Mulyawan, S Rajbhandari, **H. Chun**, G.E. Faulkner, D.C. O'Brien, P.P. Manousiadis, D.A. Vithanage, G.A. Turnbull and I.D.W. Samuel, "A simple wide field of view concentrator of free space visible light communications," IEEE Summer Topicals Meeting 2015, Visible Light Communications (VisC), Nassau, Bahamas, 2015.

[5] **H. Chun**, S. Rajbhandari, G. Faulkner, K. Cameron, A. V. N. Jalajakumari, R. Henderson, D. Tsonev, M. Ijaz, Z. Chen, E. Xie, J. J. D. McKendry, J. Herrnsdorf, E. Gu, M. D. Dawson, H. Haas, and D. O'Brien, "Visible light communication using Gallium Nitride micro-LEDs," Royal Society special meeting on Communication networks beyond the capacity crunch, May 2015.

[6] **H. Chun**, S. Rajbhandari, G. Faulkner, D. Tsonev, H. Haas, and D. O'Brien, "Visible Light Communication using Laser Diode based Remote Phosphor Technique" IEEE International Conference on Communications (ICC), June 2015.

[7] M. Ijaz, D. Tsonev, J. D. McKendry, E. Xie, S. Rajbhandari, **H. Chun**, G. Faulkner, E. Gu, M. D Dawson, D. O'Brien, and H. Haas, "Experimental Proof-of-Concept of Optical Spatial Modulation OFDM using Micro LEDs," IEEE International Conference on Communications (ICC), June 2015.

[8] Dominic O'Brien, Harald Haas, Sujan Rajbhandari, **Hyunchae Chun**, Grahame Faulkner, Katherine Cameron, Aravind V. N. Jalajakumari, Robert Henderson, Dobroslav Tsonev, Muhammad Ijaz, Zhe Chen, Enyuan Xie, Jonathan J. D. McKendry, Johannes Herrnsdorf, Erdan Gu, Martin D. Dawson, "Integrated multiple input multiple output visible light communications systems: recent progress and results," SPIE Photonics West, San Francisco, 2015.

[9] Enyuan Xie, Jonathan J. D. McKendry, Ricardo Ferreira, Johannes Herrnsdorf, Sujan Rajbhandari, **Hyunchae Chun**, Grahame Faulkner, Erdan Gu, Dominic O'Brien, and Martin D. Dawson, "Individually-n-addressable GaN-based micro-LED arrays for high-speed visible light communications at over 1 m," SPIE Photonics West, San Francisco, 2015.

[10] S. Rajbhandari, **H. Chun**, G. Faulkner, K. Cameron, A. V. N. Jalajakumari, R. Henderson, D. Tsonev, M. Ijaz, Z. Chen, H. Haas, E. Xie, J. J. D. McKendry, J. Herrnsdorf, E. Gu, M. D. Dawson, D. O'Brien "Imaging-MIMO Visible Light Communication System using μLEDs and Integrated Receiver", Globecom 2014 Workshop - Optical Wireless Communications,2014.

[11] **H. Chun**, S. Rajbhandari, G. Faulkner, D. Tsonev, H. Haas, and D. O'Brien, "Demonstration of a Bi-directional Visible Light Communication with an overall Sum-rate of 110 Mb/s using LEDs as Emitter and Detector" 27th IEEE Photonics Conference, pp. 132-133, San Diego, USA, 2014.

[12] D. O'Brien, S. Collins, **H. Chun**, G. Faulkner, S. Rajbhandari, A. Watt, P. Manousiadis, D. A. Vithanage, G. A. Turnbull, I. D.W. Samuel, R. Henderson, K. Cameron, D. Tsonev, S. Videv, H. Haas, E. Xie, E. Gu, J.J.D. McKendry, and M. D. Dawson, "Visible Light Communications: improving data rate, link margin and field of view", 27th IEEE Photonics Conference, pp. 128-129, San Diego, USA 2014.

[13] **H. Chun**, S. Rajbhandari, G. Faulkner, and D. O'Brien "Effectiveness of Blue-filtering in WLED based Indoor Visible Light Communication", 3rd International Workshop on Optical Wireless Communications, 2014.

[14] **Hyunchae Chun**; Chien-Jung Chiang; O'brien, D., "Visible light communication using OLEDs: Illumination and channel modeling," Optical Wireless Communications (IWOW), 2012 International Workshop on, Oct. 2012.

[15] A. Murakami, **H. C. Jeon (H. Chun)**, K. Y. Cho, A. Agata, Y. Takushima, Y. C. Chung, and Y. Horiuchi , "Reflection tolerance enhancement of RSOA-based WDM PON by using optical frequency dithering," Optical Fiber Communication Conference 2009, OMN4, San Diego, California, USA, 2009.

[16] **H. C. Jeon (H. Chun)**, K. Y. Cho, Y. Takushima, and Y. C. Chung, "Reflection Tolerance of RSOA-based WDM PON employing Seed light," Photonics Conference 2008, F1A-4, Je-cheon, Rep. of Korea, Nov. 2008.

[17] **H. C. Jeon (H. Chun)**, K. Y. Cho, Y. Takushima, and Y. C. Chung, "High reflection tolerance of 1.25-Gb/s RSOA-based WDM PON employing spectrum-sliced ASE source," Asia-Pacific Optical Communications Conference 2008, paper 7136-23, Hangzhou, China, 2008.

References

[1] L. Hanzo, H. Haas, and S. Imre, “Wireless myths, realities, and futures: from 3G/4G to optical and quantum wireless,” IEEE Proc. Special Centennial Issue, pp. 1853–1888, May 2012.

[2] D. O’Brien, G. Parry, and P. Stavrinou, “Optical hotspots speed up wireless communication,” Nature Photonics, vol. 1, no. 5, pp. 245–247, May 2007.

[3] Cisco, “802 . 11ac : The Fifth Generation of Wi-Fi,” no. March, pp. 1–25, 2014.

[4] Report ITU-R, “Multiple Gigabit Wireless Systems in frequencies around 60 GHz,” M.2227, 2011.

[5] G. Staple and K. Werbach, “The End of Spectrum Scarcity,” Spectrum, IEEE , vol.41, no.3, pp.48,52, March 2004.

[6] S. Berger, A. Drozd, and Don Heirman, “a New Challenge for Emc Policy Defined Radio,” IEEE EMC Soc. Newsl., no. January, pp. 1–13, 2005.

[7] A. General, “4G radio spectrum auction : lessons learned,” no. March, 2014.

[8] A. Ghosh, T. Thomas, M. Cudak, and R. Ratasuk, “Millimeter wave enhanced local area systems: A high data rate approach for future wireless networks,” vol. 32, no. 6, pp. 1152–1163, 2014.

[9] W. Roh, J. Y. Seol, J. Park, B. Lee, J. Lee, Y. Kim, J. Cho, K. Cheun, and F. Aryanfar, “Millimeter-wave beamforming as an enabling technology for 5G cellular communications: Theoretical feasibility and prototype results,” IEEE Commun. Mag., vol. 52, no. 2, pp. 106–113, 2014.

[10] S. Hranilovic, Wireless optical communication systems. 2005.

[11] A. Gomez, K. Shi, C. Quintana, M. Sato, G. Faulkner, B. C. Thomsen, and D. O. Brien, “Beyond 100-Gb/s Indoor Wide Field-of-View Optical Wireless Communications,” 2014.

[12] F. Demers, H. Yanikomeroglu, and M. St-Hilaire, “A survey of opportunities for free space optics in next generation cellular networks,” CNSR 2011, pp. 210–216, 2011.

[13] F. R. Gfeller and U. Bapst, “Wireless in-house data communication via diffuse infrared radiation,” Proc. IEEE, vol. 67, no. 11, pp. 1474–1486, 1979.

[14] F. E. Goodwin, “A review of operational laser communication systems,” Proc. IEEE, vol. 58, no. 10, 1970.

[15] IrDA, http://www.irda.org. .

[16] H. Du, R. Green, and Y. Chen, “Optical wireless 2x2 indoor MIMO system based on OOK modulation,” Int. Conf. Transparent Opt. Networks, vol. 1, no. c, pp. 3–5, 2013.

[17] D. O. Brien, R. Turnbull, H. Le Minh, G. Faulkner, O. Bouchet, P. Porcon, M. El Tabach, E. Gueutier, M. Wolf, L. Grobe, and J. Li, “High-Speed Optical Wireless Demonstrators : Conclusions and Future Directions,” vol. 30, no. 13, pp. 2181–2187, 2012.

[18] Vishay Semiconductors, “Vishay Semiconductors Eye Safety Risk Assessment of Infrared Emitting Diodes According IEC 62471 (based on CIE S009) Eye Safety Vishay Semiconductors,” vol. 62471, no. 1, pp. 1–5, 2008.

[19] U.S. Department of Energy, “Solid-State Lighting Research and Development: Multi-Year Program Plan.” 2013.

[20] Y. Narukawa, M. Ichikawa, D. Sanga, M. Sano, and T. Mukai, “White light emitting diodes with super-high luminous efficacy,” J. Phys. D. Appl. Phys., vol. 43, no. 35, p. 354002, Sep. 2010.

[21] McKinsey & Company, “Lighting the way: Perspectives on the global lighting market.”, 2011.

[22] Visible Light Communication Consotium, “http://www.vlcc.net.”

[23] L. Grobe, A. Paraskevopoulos, J. Hilt, D. Schulz, F. Lassak, and F. Hartlieb, “High-Speed Visible Light Communication Systems,” Communications Magazine, IEEE , vol.51, no.12, pp.60,66, December 2013.

[24] Y. Z. Y. Zheng and M. Z. M. Zhang, “Visible Light Communications-Recent Progresses and Future Outlooks,” Photonics Optoelectron. (SOPO), 2010.

[25] D. Tsonev, S. Videv, and H. Haas, “Towards a 100 Gb/s visible light wireless access network,” Opt. Express, vol. 23, no. 2, p. 1627, Jan. 2015.

[26] H. Lu, Y. Lin, P. Wu, C. Chen, M. Chen, and T. Jhang, “A multiple-input-multiple-output visible light communication system based on VCSELs and spatial light modulators,” Opt. Express, vol. 22, no. 3, pp. 3468–3474, 2014.

[27] G. Cossu, a Wajahat, R. Corsini, and E. Ciaram, “5.6 Gbit/s Downlink and 1.5Gbit/s Uplink Optical Wireless Transmission at Indoor Distances (>1.5m),” ECOC 2014, pp. 5–7, 2014.

[28] F. M. Wu, C. T. Lin, C. C. Wei, C. W. Chen, Z. Y. Chen, H. T. Huang, and S. Chi, "Performance Comparison of OFDM Signal and CAP Signal Over High Capacity RGB-LED-Based WDM Visible Light Communication," IEEE Photonics J., vol. 5, no. 4, pp. 7901507–7901507, Aug. 2013.

[29] A. H. Azhar, T. Tran, and D. O'Brien, "A Gigabit / s Indoor Wireless Transmission Using MIMO OFDM Visible-Light Communications," IEEE PTL., vol. 25, no. 2, pp. 171–174, 2013.

[30] K. Langer, J. Hilt, D. Shulz, F. Lassak, F. Hartlieb, C. Kottke, L. Grobe, V. Jungnickel, and A. Paraskevopoulos, "Rate-adaptive visible light communication at 500Mb/s arrives at plug and play," SPIE Newsroom, pp. 2–4, 2013.

[31] D. O'Brien and G. Faulkner, "100-Mb/s NRZ Visible Light Communications Using a Postequalized White LED," IEEE Photonics Technol. Lett., vol. 21, no. 15, pp. 1063–1065, Aug. 2009.

[32] Ultra-Prallel Visible Light Communications (UP-VLC), "http://up-vlc.photonics.ac.uk." .

[33] D. Tsonev, H. Chun, S. Rajbhandari, J. J. D. Mckendry, M. Ieee, S. Videv, E. Gu, M. Haji, S. Watson, A. E. Kelly, G. Faulkner, M. D. Dawson, F. Ieee, H. Haas, and D. O. Brien, "A 3-Gb / s Single-LED OFDM-based Wireless VLC Link Using a Gallium Nitride μ LED," Photonics Technology Letters, IEEE , vol.26, no.7, pp.637,640, April1, 2014.

[34] H. Chun, P. Manousiadis, S. Rajbhandari, D. A. Vithanage, G. Faulkner, D. Tsonev, J. James, D. Mckendry, S. Videv, E. Xie, E. Gu, M. D. Dawson, H. Haas, G. A. Turnbull, S. Member, I. D. W. Samuel, and D. C. O. Brien, "Visible Light Communication Using a Blue GaN μ LED and Fluorescent Polymer Color Converter," vol. 26, no. 20, pp. 2035–2038, 2014.

[35] J. M. Kahn and J. R. Barry, "Wireless Infrared Communications," Proceedings of the IEEE , vol.85, no.2, pp.265,298, Feb 1997.

[36] J. Grubor, S. Randel, K.-D. Langer, and J. W. Walewski, "Broadband Information Broadcasting Using LED-Based Interior Lighting," J. Light. Technol., vol. 26, no. 24, pp. 3883–3892, Dec. 2008.

[37] T. Komine and M. Nakagawa, "Fundamental analysis for visible-light communication system using LED lights," Consumer Electronics, IEEE Transactions on , vol.50, no.1, pp.100,107, Feb 2004.

[38] J. Barry, Wireless infrared communications. 1994.

[39] F. J. Lopez-Hernandez, R. Perez-Jimenez, and A. Santamarıa, “Ray-tracing algorithms for fast calculation of the channel impulse response on diffuse IR wireless indoor channels,” Opt. Eng., vol. 39, pp. 2775–2780, 2000.

[40] S. Long, M. Khalighi, M. Wolf, S. Bourennane, and Z. Ghassemlooy, “Channel Characterization for Indoor Visible Light Communications,” Optical Wireless Communications (IWOW), 2014 3rd International Workshop in , vol., no., pp.75,79, 17-17 Sept. 2014.

[41] D. Barros, S. Wilson, and J. Kahn, “Comparison of Orthogonal Frequency-Division Multiplexing and Pulse-Amplitude Modulation in Indoor Optical Wireless Links,” IEEE Trans. Commun., vol. 60, no. 1, pp. 153–163, 2012.

[42] T. Fath and H. Haas, “Performance Comparison of MIMO Techniques for Optical Wireless Communications in Indoor Environments,” IEEE Trans. Commun., vol. 61, no. 2, pp. 733–742, Feb. 2013.

[43] J. J. Tan, C. Q. Zou, S. H. Du, and J. T. Tan, “Simulation of MIMO channel characteristics for indoor visible light communication with LEDs,” Int. J. Light Electron Opt., vol. 125, no. 1, pp. 44–49, Jan. 2014.

[44] J. Armstrong and B. Schmidt, “Comparison of asymmetrically clipped optical OFDM and DC-biased optical OFDM in AWGN,” Commun. Lett. IEEE, vol. 12, no. 5, pp. 343–345, 2008.

[45] S. Dissanayake and J. Armstrong, “Comparison of ACO-OFDM, DCO-OFDM and ADO-OFDM in IM/DD systems,” Lightwave Technology, Journal of , vol.31, no.7, pp.1063,1072, April1, 2013.

[46] S. Randel and F. Breyer, “Advanced modulation schemes for short-range optical communications,” Selected Topics in Quantum Electronics, IEEE Journal of , vol.16, no.5, pp.1280,1289, Sept.-Oct. 2010.

[47] S. Dimitrov, S. Sinanovic, and H. Haas, “Signal Shaping and Modulation for Optical Wireless Communication,” Lightwave Technology, Journal of, pp. 1–11, 2012.

[48] F. Wu, C. Lin, C. Wei, and C. Chen, “1.1-Gb/s White-LED-Based Visible Light Communication Employing Carrier-Less Amplitude and Phase Modulation,” vol. 24, no. 19, pp. 1730–1732, 2012.

[49] Y. Wang, L. Tao, Y. Wang, and N. Chi, “High speed WDM visible light communication based on multi-band CAP64 with weighted pre- equalization and modified CMMA based post- equalization,” vol. 21, no. 5, pp. 18842–18848, 2013.

[50] K. Cho and D. Yoon, “On the general BER expression of one- and two-dimensional amplitude modulations,” IEEE Trans. Commun., vol. 50, no. 7, pp. 1074–1080, Jul. 2002.

[51] J. Armstrong and A. Lowery, “Power efficient optical OFDM,” Electron. Lett., vol. 42, no. 6, 2006.

[52] H. Myung, J. Lim, and D. Goodman, “Peak-To-Average Power Ratio of Single Carrier FDMA Signals with Pulse Shaping,” 2006 IEEE 17th Int. Symp. Pers. Indoor Mob. Radio Commun., pp. 1–5, Sep. 2006.

[53] Y.-J. Kim and X. Li, “A Low PAPR Visible Light Communication System Employing SC-FDMA Technique,” Appl. Math. Inf. Sci., vol. 7, no. 2, pp. 539–544, Mar. 2013.

[54] S. Qureshi, “Adaptive equalization,” Proc. IEEE, vol. 73, no. 9, pp. 1349–1387, 1985.

[55] B. Sklar, Digital Communications– second edition. 2002.

[56] T. Komine, S. Haruyama, and M. Nakagawa, “Adaptive equalization system for visible light wireless communication utilizing multiple white LED lighting equipment,” IEEE Trans. Wirel. Commun., vol. 8, no. 6, pp. 2892–2900, Jun. 2009.

[57] P. S. Chow, J. M. Cioffi, and J. C. Bingham, “A practical discrete multitone transceiver loading algorithm for data transmission over spectrally shaped channels,” IEEE Trans. Commun., vol. 43, no. 2, pp. 773–775, 1995.

[58] H. E. Levin, “A complete and optimal data allocation method for practical discrete multitone systems,” GLOBECOM’01. IEEE Glob. Telecommun. Conf. (Cat. No.01CH37270), pp. 369–374, 2001.

[59] O. González, “Multiple-Input Multiple-Output (MIMO) Optical Wireless Communications,” no. Vlc, pp. 1–22, 2012.

[60] A. Azhar, T. Tran, and D. O’Brien, “Demonstration of high-speed data transmission using MIMO-OFDM visible light communications,” GLOBECOM Workshop, pp. 1052–1056, 2010.

[61] L. Zeng, S. Member, D. O' Brien, H. Le Minh, G. E. Faulkner, K. Lee, D. Jung, Y. Oh, and E. T. Won, “High Data Rate Multiple Input Multiple Output (MIMO) Optical Wireless Communications Using White LED Lighting,” vol. 27, no. 9, pp. 1654–1662, 2009.

[62] R. Mesleh, H. Elgala, and H. Haas, “Optical Spatial Modulation,” J. Opt. Commun. Netw., vol. 3, no. 3, p. 234, Feb. 2011.

[63] E. Poves, W. Popoola, H. Haas, J. Thompson, and D. Cárdenas, “Experimental Results on the Performance of Optical Spatial Modulation Systems,” 2012 IEEE Veh. Technol. Conf. (VTC Fall), pp. 1–5, Sep. 2012.

[64] K. D. Dambul, D. C. O’Brien, and G. Faulkner, “Indoor Optical Wireless MIMO System With an Imaging Receiver,” IEEE Photonics Technol. Lett., vol. 23, no. 2, pp. 97–99, Jan. 2011.

[65] J. Wang and A. M. C. Model, “A Comparative Study of MIMO Detection Algorithms for Wideband Spatial Multiplexing Systems,” no. 1, pp. 408–413, 2005.

[66] R. Van Nee, A. Van Zelst, G. Awater, “Maximum Likelihood Decoding in a Space Division Multiplexing System,” ehicular Technology Conference Proceedings, 2000. VTC 2000-Spring Tokyo. 2000 IEEE 51st , vol.1, no., pp.6,10 vol.1, 2000.

[67] B. Laboratories, L. Technologies, and H. Rd, “V-BLAST : An Architecture for Realizing Very High Data Rates Over the Rich-Scattering Wireless Channel,” Signals, Systems, and Electronics, 1998. ISSSE 98. 1998 URSI International Symposium on , pp.295,300, 29 Sep-2 Oct 1998.

[68] G. J. Foschini and M. J. Gans, “On Limits of Wireless Communications in a Fading Environment when Using Multiple Antennas,” pp. 311–335, 1998.

[69] P. M. Butala, H. Elgala, and T. D. C. Little, “Performance of Optical Spatial Modulation and Spatial Multiplexing with Imaging Receiver,” Wireless Communications and Networking Conference (WCNC), 2014 IEEE , vol., no., pp.394,399, 6-9 April 2014.

[70] A. Van Zelst and J. Hammerschmidt, “A single coefficient spatial correlation model for multiple-input multiple-output (MIMO) radio channels,” Proc. URSI, pp. 2–5, 2002.

[71] C. Soo, “MIMO-OFDM Wireless Communications with Matlab.” Wiley, 2010.

[72] J. J. D. McKendry, R. P. Green, a. E. Kelly, Z. Gong, B. Guilhabert, D. Massoubre, E. Gu, and M. D. Dawson, “High-Speed Visible Light Communications Using Individual Pixels in a Micro Light-Emitting Diode Array,” IEEE Photonics Technol. Lett., vol. 22, no. 18, pp. 1346–1348, Sep. 2010.

[73] Hyunchae Chun, Sujan Rajbhandari, Dobroslav Tsonev, Grahame Faulkner, Harald Haas, D. O'Brien, “Visible Light Communication using Laser Diode based Remote Phosphor Technique,” in IEEE ICC, 2015.

[74] A. M. Khalid, G. Cossu, R. Corsini, P. Choudhury, and E. Ciaramella, “1-Gb/s Transmission Over a Phosphorescent White LED by Using Rate-Adaptive Discrete Multitone Modulation,” IEEE Photonics J., vol. 4, no. 5, pp. 1465–1473, Oct. 2012.

[75] H. Xiao, Y.-J. Lu, T.-M. Shih, L.-H. Zhu, S.-Q. Lin, P. J. Pagni, and Z. Chen, “Improvements on Remote Diffuser-Phosphor-Packaged Light-Emitting Diode Systems,” IEEE Photonics J., vol. 6, no. 2, pp. 1–8, 2014.

[76] L. Ulrich, “Whiter brights with lasers,” Spectrum, IEEE, vol. 50, no. 11, p. 36,56, 2013.

[77] A Neumann, J. J. Wierer, W. Davis, Y. Ohno, S. R. J. Brueck, and J. Y. Tsao, “Four-color laser white illuminant demonstrating high color-rendering quality.,” Opt. Express, vol. 19 Suppl 4, no. May, pp. A982–A990, 2011.

[78] C. Basu, M. Meinhardt-Wollweber, and B. Roth, “Lighting with laser diodes,” Adv. Opt. Technol., vol. 2, no. 4, pp. 313–321, Jan. 2013.

[79] K.-L. Du and M. N. S., “Wireless Communication Systems: From RF Subsystems to 4G Enabling Technologies,” Cambridge Univ. Press, 2010.